Synthesis and Property Characterization of Rare-Earth High-Entropy Oxides with Pyrochlore-Type Structures

A Dissertation Presented for the
Doctor of Philosophy
Degree
The University of Tennessee, Knoxville

Candice M. Kinsler-Fedon
May 2022

Copyright © 2022 by Candice Kinsler-Fedon.
All rights reserved.

DEDICATION

I would like to dedicate this dissertation to my family and husband for their love, encouragement, and support.

ACKNOWLEDGEMENTS

It has been an incredibly rewarding experience studying at the University of Tennessee Knoxville, where I attended for my undergraduate and graduate programs. It is a great achievement to make it to this point in my education; however, I did not do it alone. The support and assistance of many wonderful people have allowed me to be where I am today, and for this I am forever grateful!

First, I would like to thank my family and my husband for their continuous support, love, and encouragement throughout my time at the University of Tennessee. I would also like to thank my committee members, beginning with my Ph.D. advisor, Dr. Veerle Keppens, for her support, encouragement, and vast knowledge of RUS and magnetism! I know she spent many hours proofreading my manuscripts and this dissertation, and for all the time she has taken to work with me, I am truly thankful. I would also like to thank Dr. David Mandrus for co-advising me by providing helpful knowledge and advice for my research to move forward. I also enjoyed the local outdoor activities he would suggest for the group! I am also thankful to Dr. Haidong Zhou for allowing me to join his research group as an undergraduate in Physics. This experience was invaluable to me because I learned most of my current laboratory skills during that time and, ultimately, it set the stage for the research I conducted as a graduate student. Many thanks to Dr. William J. Weber and Dr. Yanwen Zhang for introducing me to ion-irradiation experimentation. Their patience in guiding me through this work and a manuscript was tremendously helpful, and I truly appreciate their time! My gratitude must also go out to Dr. Jiaqiang Yan for introducing the topic of high entropy oxides to our group and providing very helpful feedback on my first manuscript. To all my Oak Ridge National Laboratory collaborators, thank you for your collaborations and insight.

I have so much appreciation for the students, post doctorates, and group members, past and present, that have helped me along the way. I must acknowledge the students that supported my research: Amanda Haglund for teaching me RUS measurements and analysis, Lauren Nuckols irradiated my single crystalline samples and walked me through the analysis. Qing Huang taught and assisted during float-zone synthesis. Serena

Beauchamp worked with me to discover the best way to polish my single crystals. Sean Drewry hot pressed several compositions to help achieve denser samples for RUS. Rubayet Tanveer assisted in the lab during my final months as a student and was a pleasure to teach! I also must acknowledge former group member Michael Koehler for always making time to help with RUS questions!

Finally, I would like to thank fellow group members: Rui Xue, Takahiro Matsuoka, Hasitha Suriya Arachchige, Shirin Mozaffari, Richa Pokharel Maghogaria, Nan Huang, Matthew Cothrine, and William Meier for always being there to help problem solve and troubleshoot lab equipment. It certainly takes a team to keep a lab operating! The conversations, sharing of knowledge, and true friendship of every member in the Mandrus/Keppens research group has made my experience in graduate school so much better! I certainly never felt alone, and I cannot express in words my gratitude for you all! For anyone I unintentionally excluded, thank you for everything you do.

ABSTRACT

In the search for novel materials with advanced physical properties, the concept of adding configurational entropy onto a single atomic site is known to provide new avenues toward material discovery. In the case of high entropy oxides (HEOs), the ability to "tune" a material's properties by having multiple cations on single or multiple sites allows for greater opportunity to design materials for specific applications. The work presented here explores the synthesis of new multicomponent (high entropy) oxides, followed by a detailed characterization using several techniques. We have successfully synthesized multiple single-phase polycrystalline rare-earth high entropy oxides and grown large, bulk single crystals with the titanate pyrochlore composition using the floating zone technique. Characterization involving mechanical stiffness, thermal expansion, and irradiation amorphization resistance is presented, allowing for a detailed investigation of these new complex oxides and their potential applications.

TABLE OF CONTENTS

Chapter One Introduction 1
Chapter Two Background and Overview 3
2.1 The Pyrochlore Structure 3
2.2 The Tripod Kagome Lattice Structure 3
2.3 The Concept of "High Entropy" 5
2.4 High-Entropy Pyrochlore Oxides 7
Chapter Three Methodology and Experimental Techniques 9
3.1 Sample Synthesis and Crystal Growth 9
3.1.1 Polycrystalline samples synthesized by Solid State Reaction 9
3.1.2 Single Crystal Growth with Optical Floating Zone 9
3.2 X-Ray Diffraction 10
3.2.1 Powder X-ray Diffraction (XRD) 10
3.2.2 Laue Diffraction 13
3.2.3 Non-ambient X-ray Diffraction (HTXRD) 13
3.3 Microscopy and Microstructure Analysis 14
3.3.1 Scanning Electron Microscopy and Energy Dispersive X-ray (SEM/EDX) 14
3.3.2 HAADF-STEM EELS/TEM 14
3.4 Magnetization and Magnetic Susceptibility 15
3.4.2 Magnetic Frustration in Pyrochlore Oxides 15
3.5 Resonant Ultrasound Spectroscopy (RUS) 18
3.5.1 Concept 18
3.5.2 RUS Sample Preparation 19
3.5.3 RUS Procedure and Analysis 20
3.5.4 RUS for Probing Structural Phase Transitions 20
3.6 Ion-Irradiation and Rutherford Backscattering Spectrometry (RBS) 23
3.6.1 Purpose and General Concept 23
3.6.2 Ion-Irradiation Procedure 24
3.6.3 Rutherford Backscattering Spectrometry (RBS) and Ion Channeling 25
Chapter Four Synthesis, characterization, and single-crystal growth of a high-entropy rare-earth pyrochlore oxide 30
Chapter Five Effects of ion-irradiation induced damage in high-entropy pyrochlore oxide single crystals 56
Chapter Six Non-ambient x-ray diffraction for the study of the structural stability of entropic pyrochlore oxides at elevated temperatures 74
Chapter Seven Mechanical properties of high entropy pyrochlores using resonant ultrasound spectroscopy 83
Chapter Eight Conclusions and Recommendations 94
List of References 96
Appendices 110
Appendix A 110
List of additional high entropy oxides synthesized 110
Appendix B 111

Additional X-Ray diffraction data 111
Appendix C 123
Additional Scanning Electron microscopy results 123
Appendix D 138
Ambient Temperature Resonant Ultrasound Spectroscopy of High Entropy Oxide Fluorites 138
Appendix E 142
DC Susceptibility Curves 142
Vita 149

LIST OF TABLES

Table 3.1: List of successfully synthesized pyrochlore-type HEOs with their sintering temperature, sintering time, structure, space group, and lattice parameters. 12
Table 3.2: Ion-irradiation experiments, irradiation rounds, and ion fluences for each area on HEO single crystal $(YbHoTmErLu)_2Ti_2O_7$. Ion fluences are in ions/cm^2. 27
Table 4.1: List of comparable lattice parameters of the single-component rare-earth pyrochlore titanate oxides and HEO rare-earth pyrochlore titanate. 34
Table 4.2: Area scan concentration data for single crystal $(Yb_{0.2}Tb_{0.2}Gd_{0.2}Dy_{0.2}Er_{0.2})_2Ti_2O_7$. 38
Table 4.3: Calculated effective magnetic moments, applied field direction, temperature ranges, and Curie-Weiss temperatures for $(5RE_{0.2})_2Ti_2O_7$. 49
Table 4.4: Compilation of literature reported magnetic moments for the single component rare-earth pyrochlore oxides, applied field direction (for single crystals), temperature ranges measured, free ion magnetic moments, and Curie-Weiss temperatures..... 51
Table 5.1: Comparison of the HEO pyrochlore irradiation conditions and fluence/dose for achieving amorphous state at damage peak with those of single-component rare-earth titanate pyrochlores. 66
Table 5.2: Comparison of the HEO's amorphization model parameters to $Gd_2Ti_2O_7$ [25]. These parameters were determined from data fits shown in Figures 5.2(c) and 5.5. 68
Table 6.1: List of experimentally derived linear thermal expansion coefficients for each HEO pyrochlore-type composition. 81
Table 7.1: Room temperature elastic moduli values for single crystalline HEO pyrochlore $(YbHoTmErLu)_2Ti_2O_7$ and parent non-HEO pyrochlores..... 85

LIST OF FIGURES

Figure 2.1: (a) Representation of the rare-earth pyrochlore structure with O^{2-} ions in red, B^{4+} ions light blue, and the A^{3+} ions multi-colored and (b) corner-sharing tetrahedra formed by the A sublattice [55]. 4
Figure 2.2: Diagram comparing the (a) pyrochlore structure with alternating triangular and kagome layers and (b) tripod kagome structure with alternating RE-kagome and Mg-triangular layers [56]. 4
Figure 3.1: (a) Typical floating zone crystal growth set-up; (b) result of crystal growth for $(Yb_{0.2}Tb_{0.2}Gd_{0.2}Dy_{0.2}Er_{0.2})_2Ti_2O_7$; (c) Laue diffraction pattern of crystal aligned along [110]. 11
Figure 3.2: The cubic pyrochlore A and B sublattices [25]. 16
Figure 3.3: Frustration of antiferromagnetic spins on a triangular lattice. 16
Figure 3.4: (a) Room temperature RUS probe typically used with digital RUS system. (b) In-house designed RUS probe used for measurements as a function of temperature in a PPMS or VersaLab system with rectangular parallelepiped shaped crystal positioned between two transducers. 21
Figure 3.5: Example of a typical resonance spectrum. 22
Figure 3.6: HEO single crystal mounted on the sample stage for room temperature ion irradiation of 4 MeV Au^{2+} ions with two irradiation areas labeled A and B. 26
Figure 3.7: (a) Material with random order (leads to more backscatter) and (b) a single crystal aligned so that rows of atoms (blue dots) are incident with the ion beam. The trajectory of a high energy ion is represented by the black arrows depicting low-angle scattering. 29
Figure 4.1: Room temperature powder X-ray diffraction pattern of polycrystalline $(5RE_{0.2})_2Ti_2O_7$. The refinement pattern (red line) overlays the observed pattern (black circles) which matches the $Fd\bar{3}m$ cubic structure (green vertical dashed lines are the Bragg reflections characteristic of the pyrochlore phase). The difference pattern is represented in blue below the diffraction pattern. 33
Figure 4.2: (a) Resulting multi-crystal of $(5RE_{0.2})_2Ti_2O_7$ of ~7 cm in length. (b)-(d) Laue diffraction patterns of $(5RE_{0.2})_2Ti_2O_7$ taken from various sections of the ingot showing good quality with (b) aligned in the [111], (c) in the [110], and (d) in the [100]. 36
Figure 4.3: SEM image at 200 µm and area scan of single crystal $(5RE_{0.2})_2Ti_2O_7$. 37
Figure 4.4: Elemental mapping of polycrystalline $(5RE_{0.2})_2Ti_2O_7$ showing homogeneity near 10 µm. 39
Figure 4.5: HAADF-STEM images along the [011] zone axis for (a) single-crystalline and (b) polycrystalline $(5RE_{0.2})_2Ti_2O_7$, respectively. The inset in (a) is the crystal structure in this projection, where only cations are shown (the red and the blue are Ti and rare-earth atoms, respectively). The intensity variations arise from three types of atomic columns along this direction. The columns with brightest, intermediate, and weakest contrasts involve 100% rare-earth atoms, 50% rare-earth atoms plus 50% Ti atoms, and 100% Ti atoms, respectively. 41

Figure 4.6: HAADF-STEM imaging and nanoscale electron-energy loss spectroscopy (EELS) mapping along [001] for the single crystalline $(5RE_{0.2})_2Ti_2O_7$. (a) Atomic-resolution HAADF image for the EELS mapping region with the dimension of 27 nm × 27 nm. (b)-(g) EELS mapping analysis: (b) HAADF image recorded simultaneously during the EELS data set acquisition; (c) Yb, (d) Tb, (e) Gd, (f) Dy, and (g) Er chemical maps obtained from their M_5-signals, respectively. Note that each pixel in EELS maps is scanned by 16 × 16 for the simultaneously recorded HAADF image in (b), resulting in atomic-resolution in (b) while nano-scale resolution in the EELS maps in (c)-(g). 42
Figure 4.7: (a) Average low-loss electron-energy loss (EEL) spectrum for the region in Figure 4.6(a). The thickness for this region is calculated to be ~0.5□ using the log-ratio method, where □ is an inelastic mean free path. (b) Average core-loss EEL spectrum for this region shows the $M_{4,5}$ edges of Gd, Tb, Dy, Er and Yb, respectively. 43
Figure 4.8: HAADF-STEM imaging and atomic scale electron-energy loss spectroscopy (EELS) mapping along [001] for the single-crystalline $(5RE_{0.2})_2Ti_2O_7$. (a) Atomic-resolution HAADF image, where the green region was used for EELS mapping analysis in (b)-(g). (b) HAADF image recorded simultaneously during the EELS data set acquisition; (c) Yb, (d) Tb, (e) Gd, (f) Dy, and (g) Er chemical maps obtained from their M_5-signals, respectively. 45
Figure 4.9: HAADF-STEM imaging and nano-scale electron-energy loss spectroscopy (EELS) mapping along [001] for the polycrystalline $(5RE_{0.2})_2Ti_2O_7$. (a) Atomic-resolution HAADF image for the EELS mapping region with the dimension of 27 nm × 27 nm. (b)-(g) EELS mapping analysis: (b) HAADF image recorded simultaneously during the EELS data set acquisition; (c) Yb, (d) Tb, (e) Gd, (f) Dy, and (g) Er chemical maps obtained from their M_5-signals, respectively. Note that each pixel in EELS maps is scanned by 16 × 16 for the simultaneously recorded HAADF image in (b), resulting in atomic-resolution in (b) while nano-scale resolution in the EELS maps in (c)-(g). 46
Figure 4.10: HAADF-STEM imaging and atomic-scale electron-energy loss spectroscopy (EELS) mapping along [001] for the polycrystalline $(5RE_{0.2})_2Ti_2O_7$. (a) Atomic-resolution HAADF image, where the green region was used for EELS mapping analysis in (b)-(g). (b) HAADF image recorded simultaneously during the EELS data set acquisition; (c) Yb, (d) Tb, (e) Gd, (f) Dy, and (g) Er chemical maps obtained from their M_5-signals, respectively. 47
Figure 4.11: DC susceptibility measurements on $(5RE_{0.2})_2Ti_2O_7$ polycrystal (a) and single crystal with applied magnetic field along the [100] direction (b) from 3 K to 300 K, along with the magnetization curves (c) at 3 K from -7 T to 7 T. 50
Figure 4.12: AC susceptibility measurements (the real part) on single crystal $(5RE_{0.2})_2Ti_2O_7$ from temperatures of 0.3 K to 1.7 K with (a) magnetic fields ranging from 0 T to 1 T and (b) dependence on frequency ranging from 47 Hz to 995 Hz, indicating a spin-glass magnetic ground state. (c) Linear relation of frequency dependence to freezing temperature (Vogel-Fulcher law)..... 53

Figure 5.1: The depth profiles of local damage dose (dpa), represented by solid black squares, and implanted Au concentration (appm), represented by solid red circles predicted by SRIM simulations for an ion fluence of 6 $\times 10^{13}$ cm^{-2}. Solid red and black lines are fits to the data. 60
Figure 5.2: Local damage dose (dpa) as a function of depth following 4 MeV Au^{2+} irradiation to ion fluences from 0.5 to 6 ($\times 10^{13}$ cm^{-2}) of $(Yb_{0.2}Tm_{0.2}Lu_{0.2}Ho_{0.2}Er_{0.2})_2Ti_2O_7$. 61
Figure 5.3: $(Yb_{0.2}Tm_{0.2}Lu_{0.2}Ho_{0.2}Er_{0.2})_2Ti_2O_7$ rare-earth sublattice disorder curves following 4 MeV Au^{2+} irradiation with ion fluences ranging from (a) 1 to 3 ($\times 10^{13}$ cm^{-2}) and (b) 0.5 to 3.6 ($\times 10^{13}$ cm^{-2}). Solid lines represent fits to the data. (c) Relative rare-earth disorder at the damage peak as a function of Au fluence and dose. The solid red line is the fit of the damage accumulation along with the amorphous region f_a (green dashed line) and the residual crystalline region S_d (blue dashed/dotted line). 62
Figure 5.4: RBS channeling spectra for the HEO titanate pyrochlore $(Yb_{0.2}Tm_{0.2}Lu_{0.2}Ho_{0.2}Er_{0.2})_2Ti_2O_7$ aligned in the [100] direction. 65
Figure 5.5: Comparison of rare-earth disorder at the damage peak as a function of dose between reported $Gd_2Ti_2O_7$ [131] and HEO $(Yb_{0.2}Tm_{0.2}Lu_{0.2}Ho_{0.2}Er_{0.2})_2Ti_2O_7$ single crystals with 4.0 MeV Au ions at 300 K. The red and blue solid lines are fits to the damage data points. 69
Figure 5.6: Cross-sectional TEM dark-field micrographs unveiling the damaged regions near the surface of the irradiated HEO pyrochlore crystal with 4 MeV Au^{2+} ions corresponding to the regions irradiated to ion fluences of (a) 3.33×10^{13} cm^{-2} and (b) 3.66×10^{13} cm^{-2}. Insets are SAED patterns taken on-axis, with the arrows highlighting the image forming g-vector. 71
Figure 5.7: Raman spectroscopy results for HEO composition $(Yb_{0.2}Tb_{0.2}Gd_{0.2}Dy_{0.2}Er_{0.2})_2Ti_2O_7$ following 23 MeV Ni ions. Amorphization occurs at the highest ion fluence ($4x10^{16}$ ions/cm^2). 72
Figure 6.1: (a) Non-ambient X-ray diffraction plot for $(YbTbGdErDy)_2Ti_2O_7$ showing the pyrochlore structure expanding uniformly from 25˚C to 1200˚C. Inset is the expanded view of a diffraction peak from 29.8 to 31 ˚2θ. (b) Lattice parameter shift as a function of temperature up to 1200˚C (red line represents a linear fit to the data). (c) Length and volume trends with respect to temperature. 75
Figure 6.2: (a) Non-ambient X-ray diffraction plot for $(YbHoErTmLu)_2Ti_2O_7$ showing the pyrochlore structure expanding uniformly from 25˚C to 1200˚C. Inset is the expanded view of a diffraction peak from 30 to 31 ˚2θ. (b) Lattice parameter shift as a function of temperature up to 1200˚C. (c) Length and volume trends with respect to temperature. 76
Figure 6.3: (a) Non-ambient X-ray diffraction plot for $(EuNdSmLaPr)_2Hf_2O_7$ showing the pyrochlore structure expanding uniformly from 25˚C to 1200˚C. Inset is the expanded view of a diffraction peak from 29.5 to 29.5 ˚2θ. (b) Lattice parameter shift as a function of temperature up to 1200˚C. (c) Length and volume trends with respect to temperature. 77

Figure 6.4: (a) Non-ambient X-ray diffraction plot for $(GdNdSmLaPr)_2Zr_2O_7$ showing the pyrochlore structure expanding uniformly from 25˚C to 1200˚C. Inset is the expanded view of a diffraction peak from 28.4 to 29.6 ˚2θ. (b) Lattice parameter shift as a function of temperature up to 1200˚C. (c) Length and volume trends with respect to temperature. 78
Figure 6.5: (a) Non-ambient X-ray diffraction plot for $(DyHoSmGdNd)_2Sn_2O_7$ showing the pyrochlore structure expanding uniformly from 25˚C to 1200˚C. Inset is the expanded view of a diffraction peak from 28.5 to 30.5 ˚2θ. (b) Lattice parameter shift as a function of temperature up to 1200˚C. (c) Length and volume trends with respect to temperature. 79
Figure 6.6: (a) Non-ambient X-ray diffraction plot for $(NdSmEuGd)_3Sb_3Mg_2O_{14}$ showing the rhombohedral kagome structure expanding uniformly from 25˚C to 1200˚C. Inset is the expanded view of a diffraction peak from 28 to 31˚2θ. (b) Lattice parameter shift as a function of temperature up to 1200˚C. (c) Length and volume trends with respect to temperature. 80
Figure 7.1: Temperature dependence of elastic constants C' and C_{44} for $(YbHoTmErLu)_2Ti_2O_7$ single crystal from 50 to 300 K. 87
Figure 7.2: Temperature dependence showing individually tracked resonant frequencies for $(YbTbGdDyEr)_2Ti_2O_7$ single crystal from 5 to 350 K. 88
Figure 7.3: Temperature dependence of elastic constants C_{11} and C_{44} for $(EuNdSmLaPr)_2Hf_2O_7$ polycrystal from 50 to 325 K. 91
Figure 7.4: Comparison of the C_{44} (shear modulus) temperature dependence for $(EuNdSmLaPr)_2Hf_2O_7$ with polycrystalline (a) $La_2Hf_2O_7$ and (b) $Nd_2Hf_2O_7$ from 50 to 350 K. 92

CHAPTER ONE
INTRODUCTION

Originating from the notion of high entropy alloys, high entropy oxides (HEOs) are defined as oxides having five or more cations on a single atomic site [1,2], They are also known as configurationally complex oxides (CCOs) or multicomponent oxides and have been gaining interest since their introduction in 2015 when the first high entropy oxide with the rocksalt phase was reported [3]. Recent studies have explored adding configurational complexity to other oxide systems, with the most common being the fluorite [4,5], perovskite [6-9], and spinel [10-13] structures. Introducing the high entropy concept to oxides has led to the discovery of novel functionalities and capabilities including low thermal conductivity, high corrosion and oxidation resistance, increased electrical storage capacities, room temperature lithium superionic conductivity, and a wide-range of interesting magnetic behavior [14-18].

The majority of the work presented here focuses on the synthesis and characterization of compositionally complex oxides with the pyrochlore structure. Rare-earth pyrochlore oxides have been of interest to researchers for decades. The properties of these materials include high radiation resistance, low thermal conductivity, exotic magnetism, strong ionic conduction for fuel cells, and luminescence, to name a few [19-33]. In some cases, rare-earth pyrochlore oxides can be “tuned” to have enhanced properties and capabilities by doping or manipulating the A and B site cations based on their size [33,34]. However, very few studies have been conducted to see how adding multiple rare-earth cations to a single site may affect these properties in rare-earth pyrochlore oxides compared to their single component, non-HEO counterparts, the few studies available focused on the synthesis and thermal conductivity of rare-earth zirconate pyrochlores [35-38].

With this work, we expand the study of HEOs to pyrochlores. Since very few HEOs have been successfully synthesized as bulk single crystals [39-42], it is necessary to develop reliable methods of material synthesis that allow for large, high-quality crystals which will improve material property studies of these oxides for years to come. The work presented here shows that it is possible to synthesize high quality powders using standard solid state reaction synthesis and grow large single crystals (greater than 1 mm) employing the floating zone technique. A detailed

analysis of the mechanical, thermal lattice expansion, and radiation resistant properties is presented, increasing the understanding of an underdeveloped and newly produced set of high entropy rare-earth oxides. While most of the compositions in this dissertation are based on the pyrochlore structure, a few novel compositions with other structures including a tripod Kagome lattice (TKL) oxide and fluorites (Appendix D) are also discussed and explored.

CHAPTER TWO
BACKGROUND AND OVERVIEW

2.1 The Pyrochlore Structure

Pyrochlore oxides have cubic symmetry, belong to the Fd-3m space group, and contain eight formula units per unit cell. The pyrochlores in this study possess the $A_2B_2O_7$ (227) stoichiometry with trivalent rare earth cations occupying the A-site (16d) and tetravalent transition metals on the B-site (16c). Figure 2.1 illustrates the atomic pyrochlore structure with corner-sharing tetrahedra. Due to their unique structural framework, phase stability, and compositional flexibility, pyrochlores have been heavily studied for their magnetism, radiation resistance, thermal stability, and ionic/electric conductivities [19-34,43-51]. The structure of corner-sharing tetrahedra causes geometric frustration when A and/or B are magnetic cations, leading to exotic magnetic ground states such as spin ice, spin liquid, and spin glass [25-27]. Adding configurational entropy to at least one cation site induces disorder and distortion within the lattice and is expected to impact the properties of these materials. In order to synthesize an oxide in the pyrochlore phase, a cation radius ratio rule of the A/B cations (1.36 to 1.78 roughly) must be obeyed [51]. Reported exceptions to this rule involve extreme synthesis routes, such as high pressure, to produce stable 227 materials [52-54].

2.2 The Tripod Kagome Lattice Structure

As shown in Figure 2.2, the Tripod Kagome Lattice (TKL) structure is “pyrochlore-like” in that it has alternating triangular and Kagome layers (a two-dimensional arrangement of hexagons and equilateral triangles of RE^{3+} cations and formed by the vertices of the Mg^{2+} tetrahedra), much like that of the pyrochlore when positioned along the [111] orientation. In this thesis, the successful synthesis of one configurationally complex TKL composition is described and analyzed for its properties.

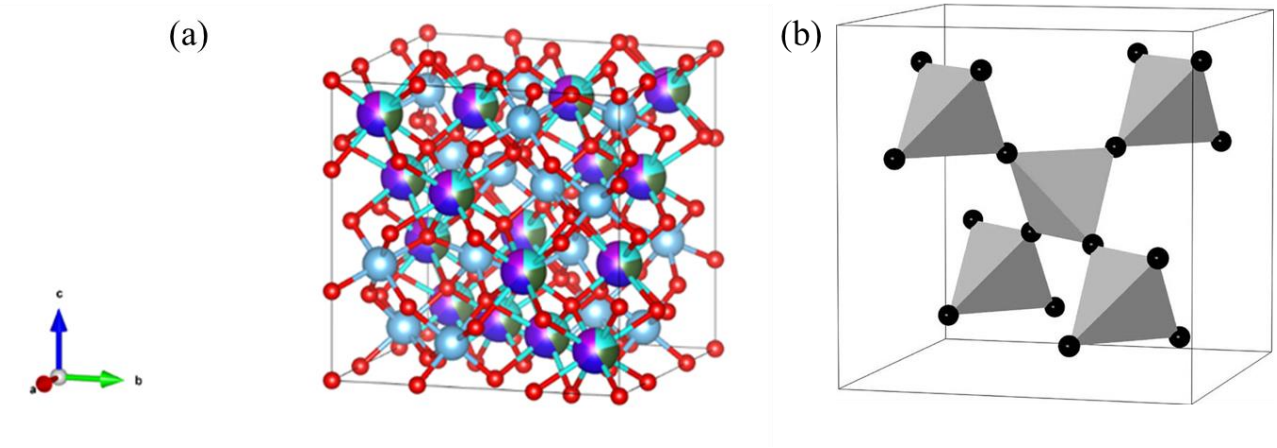

Figure 2.1: (a) Representation of the rare-earth pyrochlore structure with O^{2-} ions in red, B^{4+} ions light blue, and the A^{3+} ions multi-colored and (b) corner-sharing tetrahedra formed by the A sublattice [55].

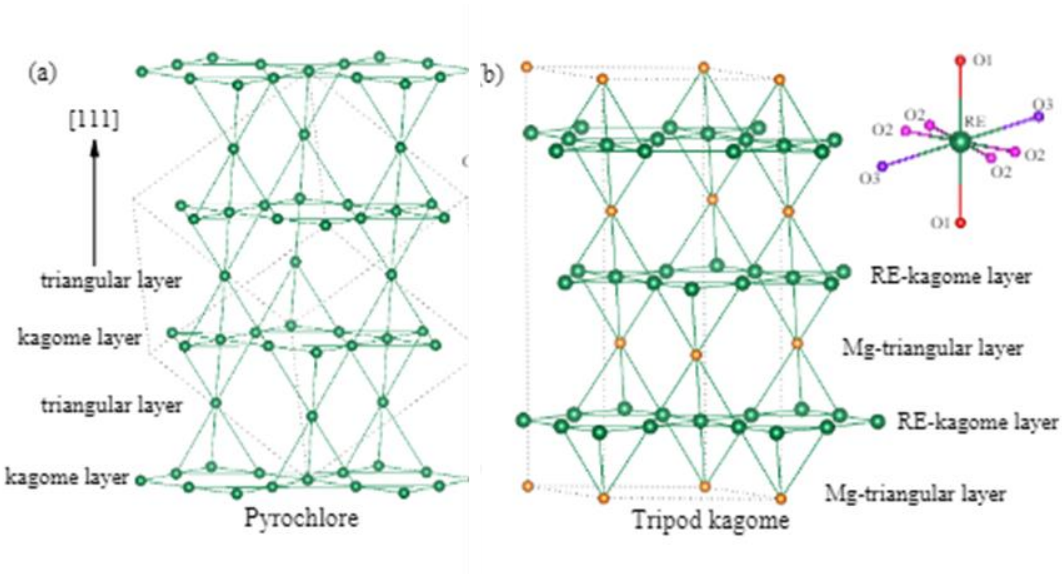

Figure 2.2: Diagram comparing the (a) pyrochlore structure with alternating triangular and kagome layers and (b) tripod kagome structure with alternating RE-kagome and Mg-triangular layers [56].

The tripod kagome lattice (TKL) with the form $RE_3Sb_3Mg_2O_{14}$ is a relatively new oxide material, as it has only been synthesized and studied within the past few decades [56-59]. It has a two-dimensional kagome lattice, belongs to the R-3m space group, and has a rhombohedral structure. Similar kagome oxides have been previously successfully synthesized with various RE cations and with Co and Zn on the Mg^{2+} site [58,59]. Thus far, much work has been conducted to understand the magnetic behavior and ground states. The synthesis of a multi-component TKL has not been reported prior to this work.

2.3 The Concept of "High Entropy"

The concept of novel material design employing "multiple principal elements in equimolar or near-equimolar ratios" was first introduced in 2004 for binary and ternary alloys [2,60]. These works introduced the idea of creating stable solid solutions of metal alloys known as high entropy alloys or HEAs by increasing the entropy of mixing. Since these reports, many research groups have reported stable high entropy alloys with five or more elements on a single atomic site and studies have shown that their mechanical, magnetic, electronic, and thermal properties can be improved by applying configurational entropy [1,61,62].

The first high entropy oxide was synthesized in 2015 by the successful incorporation of five transition metal cations onto one lattice site in the rocksalt structure ($Fm\bar{3}m$, space group # 225) [3]. This study proved the possibility of "entropy-stabilization" for oxides by mixing five binary oxides (MgO, CuO, NiO, ZnO, and CoO) in equimolar amounts at high temperatures (850 to 900˚C) to form a single-phase rocksalt solid solution. Most importantly, it was discovered that the reaction was reversible when the temperature was lowered, implying that the reaction was "entropy-driven." This concept has recently been extended beyond oxides to diborides, nitrides, carbides, sulfides, fluorides, to name a few [63-69]. For configurationally complex materials that are either oxides, diborides, carbides, or nitrides, these materials have been placed into a subset of high entropy materials coined high entropy ceramics [68-69].

When referring to the energy and processes required for a reaction to occur, it is necessary to consider the Gibbs free energy, enthalpy, and entropy changes. The Gibbs free energy is represented by

$$\Delta G = \Delta H - T\Delta S \tag{2.1}$$

where ΔG is the change in free energy, ΔH is the change in enthalpy, T is the reaction temperature, and ΔS is the entropy change in the system. In the simplest of terms, for a reaction to become thermodynamically favorable, the Gibbs free energy must be negative. There are multiple "pathways" that can be chosen for a reaction. When taking into consideration the enthalpy term and a particular pathway, the change in enthalpy can take one of two forms: mixing enthalpy for solid solution formation and formation enthalpy for compound formation. Alternatively, the entropy term is dependent on the addition of elemental components in a system and an increase in elemental arrangements within the lattice (configurational entropy). Lattice vibrations and ordering variations due to electronic or magnetic interactions can also have a role in the overall configurational entropy of a material [70]. The configurational entropy change per mole ΔS_{conf} is given by

$$\Delta S_{conf} = R \ln n \tag{2.2}$$

where R is the gas constant and n is the number of elements in equimolar amounts [2,70]. This formula represents the total configurational entropy for thermodynamic ideal mixing. To achieve ideal mixing using this equation, it is important to have a random, homogenous distribution of atoms. Additionally, increasing the number of elements n will increase the configurational entropy. Although this equation has been applied to both metals and oxide ceramics, these materials are subject to major differences such as atomic bonding and variations in crystal and electronic structures [70].

Per its earliest definition, to obtain a single-phase entropy-stabilized oxide, the configurational entropy of the system must overcome the enthalpy of formation term. This will

lead to a negative Gibbs free energy and can only occur above a critical temperature [70]. Therefore, if the temperature falls below the critical temperature, the mixed components will "decompose" into a multiphase oxide comprised of the initial oxide compounds. As discussed above, Rost et al. were able to achieve this with the first successfully synthesized high entropy oxide rocksalt [3]. This concept of entropy-stabilization has been demonstrated in other various multicomponent oxide structures [16]. However, not all reports on "HEOs" have verified that entropy is the driving force behind stabilization, including the novel pyrochlores discussed in this dissertation. Stable ternary pyrochlores can be formed with a wide range of individual rare-earth cations on the A-site, as long as the A/B cation ratio rule is obeyed. Moreover, high configurational entropy is only one aspect in creating stable single phase multicomponent solid solutions [16,70].

2.4 High-Entropy Pyrochlore Oxides

As previously discussed, the pyrochlore structure ($A_2B_2O_7$) is stable for a wide range of A and B cations. When high entropy is added to the pyrochlore system, whether on the A or B sites, a vast range of chemical compositions with the pyrochlore structure can be imagined. Due to a lack of computational guidance predicting which cation combinations would produce single-phase solid solution HEOs, many research efforts were based on "trial and error" with the primary motivation of HEO research revolving around whether specific combinations of entropic oxides could be successfully synthesized. This approach was also true when the first HEO pyrochlore studies were published in 2019. Li et al. were the first to publish a study on the successful synthesis of six new rare earth high entropy pyrochlore oxide zirconates, where Zr is on B-site and the entropy was chosen for the A-site. This study not only showed the feasibility of single-phase high entropy pyrochlores, but also showed that that they have low thermal conductivity, indicating the potential for use as thermal barrier coatings [35]. Following this publication, several more studies involving pyrochlores have been reported [36,37,71-79]. Many of these reports consisted of synthesizing HEO pyrochlore zirconates using various techniques (spark plasma sintering, low-temperature polymerized complex method, atmospheric plasma spraying,

combustion synthesis, sol-gel method, particle foaming stabilization, and conventional solid-state reactions) and confirm low to ultra-low thermal conductivity in these materials. In 2022, a computationally based study for HEO pyrochlore stability and synthesis was reported [80]. It focused on multi-cation occupancy of B-site pyrochlores and involved Monte Carlo simulations and thermodynamic processes to determine the optimum cationic combinations for predicting single phase B-site pyrochlores.

Additional studies on HEO pyrochlores have expanded to include entropy on the B-site and, in some cases, on both cationic sites [81-87]. These reports focus on synthesis and include some examination of mechanical properties such as hardness and fracture toughness. One study reports on the lattice distortions and chemical disorder [86]. The majority of HEO pyrochlores studied have multiple cations with equal or "equimolar" amounts. Recently, a few studies have explored the synthesis and stability of HEO pyrochlores with non-equimolar versions of high configurational entropy [87,88].

The search for HEO pyrochlores with more variation in composition and a broader range of insight into unique properties is ongoing. Most reports have focused on synthesizing HEO rare earth pyrochlore zirconates, with a recent expansion into a wider range of HEO pyrochlore compositions including rare earth titanates and pyrochlores with mixed B-site cations [39,81,83-85,90]. While pyrochlores in general have been heavily investigated for their frustrated magnetism, only recently has this been explored for a few HEO pyrochlores [39,89]. A study of the radiation resistant abilities of HEO pyrochlores has also been overlooked. Only a few introductory reports have discussed the possibility of using HEO pyrochlores for immobilizing radioactive waste [90,91] but none of these explore HEO pyrochlores for their amorphization resistance or studied irradiation response of single crystal HEO pyrochlores.

CHAPTER THREE
METHODOLOGY AND EXPERIMENTAL TECHNIQUES

3.1 Sample Synthesis and Crystal Growth

3.1.1 Polycrystalline samples synthesized by Solid State Reaction

The solid-state reaction method was used to produce the single-phase polycrystalline rare-earth high entropy oxides for this study. High purity (at least 99.9%) starting reactants consisting of rare-earth oxides ($RE_2^{3+}O_3$) (dried overnight at 850°C) and transition metal oxides ($M^{4+}O_2$) were weighed in stoichiometric amounts, combined in a polypropylene grinding vial with two methacrylate mixing balls, and mixed in a SPEX 8000M Mixer/Mill from 60 to 90 minutes to produce the homogenous powder. They were then pressed into pellets (using either a Carver hydraulic press or hydrostatic water-cell press) and sintered in air at high temperatures ranging from 1300˚C to 1600˚C. Some samples required multiple grindings and reheating to obtain single-phase.

3.1.2 Single Crystal Growth with Optical Floating Zone

The floating zone technique is a melt-based crystal growth method involving the use of an image furnace with multiple mirrors that focus light to a “molten zone”. A polycrystal is pulled through this molten zone at a steady growth speed to allow for single crystallization, which occurs at the solidifying end of the molten zone. “Feed” and “seed” rod pellets are counter rotated at specified speeds and a growth rate (pulling speed) is determined based on the material composition and molten zone stability. Typically, slower growth rates are preferred and produce higher quality crystals. This technique is known to produce large single crystals (up to several centimeters), ranging from good to high quality, and commonly used for various metal oxides. Standard image furnaces use halogen lamps, allowing for growths to occur at temperatures up to ~2200˚C. However, if higher temperatures are needed, the use of a Xenon lamp will allow growths with

temperatures well above 2000˚C. Multiple factors affect the growth of a crystal using this method including voltage and temperature needed, melting temperatures based on the material composition, “pulling” and “rotation” speeds, growth atmosphere, pressure, and gas flow.

It is well known that single crystals of standard pyrochlore oxides can be grown using the optical floating zone technique, but prior to our work, no studies on HEO bulk single crystals were reported. In this dissertation, single crystals of two rare-earth HEO titanate pyrochlore compositions were successfully grown with the optical floating zone technique using a two-mirror optical floating-zone furnace (Canon Machinery model SC1-MDH) with 1500-W halogen lamps. In this process, large single-phase polycrystalline pellets are cut into two unequal length pieces (feed and seed rods), placed inside a quartz chamber (feed rod was hung at the top of the chamber while the seed rod was fastened to the bottom) and counter-rotated between 20 and 25 rpm. The crystals were grown in an oxygen atmosphere (0.2 to 0.3 MPa) with pulling speeds (growth rates) ranging from 5 to 20 mm/hr. Our growth attempts produced both large multi-crystal and single crystal boules. The resulting single crystals discovered in these boules ranged in length from several millimeters to 3 centimeters. Figure 3.1(a) displays the floating-zone setup with polycrystalline sample in place. Figures 3.1(b)-(c) show a resulting HEO crystal growth with Laue diffraction back scattering image along the [110].

3.2 X-Ray Diffraction

3.2.1 Powder X-ray Diffraction (XRD)

A PANalytical Empyrean multipurpose diffractometer (Cu Kα1 radiation, λ = 1.54059 Å) was employed for the collection of room temperature powder X-ray diffraction pattern data for each of the polycrystalline HEO materials discussed in this thesis. Rietveld Refinements of each sample using this data along with the General Structure Analysis System II (GSAS-II) software [92] allowed for the determination of the crystal structure and lattice parameters. Table 3.1 lists the HEOs synthesized along with the sintering temperature, sintering time, structure, space group, and lattice parameters. Complete refinement data and XRD pattern plots are located in Appendix B.

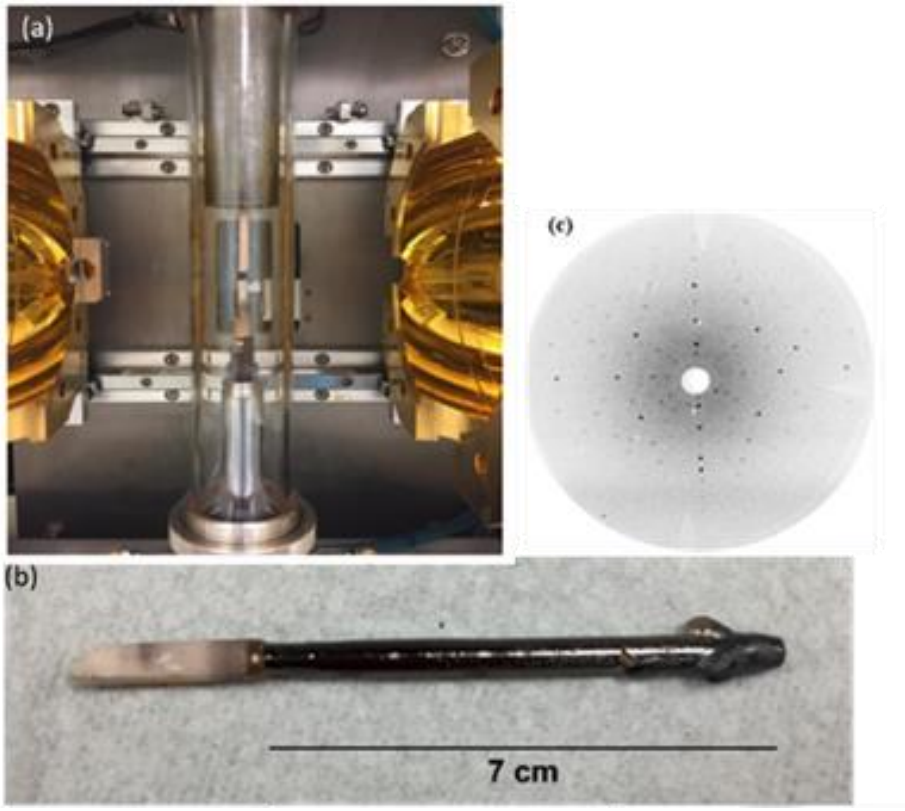

Figure 3.1: (a) Typical floating zone crystal growth set-up; (b) result of crystal growth for $(Yb_{0.2}Tb_{0.2}Gd_{0.2}Dy_{0.2}Er_{0.2})_2Ti_2O_7$; (c) Laue diffraction pattern of crystal aligned along [110].

Table 3.1: List of successfully synthesized pyrochlore-type HEOs with their sintering temperature, sintering time, structure, space group, and lattice parameters.

HEO Sample	Sintering Temperature (˚C)	Sintering Time (hrs.)	Structure	Space Group	Lattice Parameter (Å)
$(YbTbGdErDy)_2Ti_2O_7$	1400	20	Pyrochlore	Fd-3m	10.1152(3)
$(YbHoTmErLu)_2Ti_2O_7$	1300	20	Pyrochlore	Fd-3m	10.0551(3)
$(DyHoSmGdNd)_2Sn_2O_7$	1400	15	Pyrochlore	Fd-3m	10.4640(8)
$(EuPrSmLaNd)_2Hf_2O_7$	1450	20	Pyrochlore	Fd-3m	10.6569(0)
$(GdNdSmPrLa)_2Zr_2O_7$	1500	20	Pyrochlore	Fd-3m	10.6639(9)
$(NdSmEuGd)_3Sb_3Mg_2O_{14}$	1400	60	Kagome (Rhombohedral)	R-3m	a=b = 7.3857(9) c = 17.4628(5)

3.2.2 Laue Diffraction

All single crystals discussed in this dissertation have undergone Laue diffraction for structure confirmation, quality determination, and orientation for various measurements. Laue diffraction "images" appear as a collective arrangement of spots that are unique to a crystal's structure and symmetry and can be employed to determine a crystal's orientation and quality. The crystal can be positioned or "oriented" for specific experiments and measurements using Laue diffraction and a crystal aligning software (OrientExpress), which takes the recorded pattern and matches it to a simulated pattern from its database. Likewise, crystal quality is generally determined by examining the "appearance" of the Laue spots. If the spots are circular and clear (not blurred, irregularly shaped, or shadowed) then a crystal is considered high quality. Laue is also typically used to ensure that a crystal is single domain throughout. If multiple domains exist, then a multicrystal has been produced. All crystals examined have good quality or better, as seen from Figure 3.1(c).

3.2.3 Non-ambient X-ray Diffraction (HTXRD)

Non-ambient X-ray diffraction is a useful tool for understanding a material's lattice behavior in-situ with temperature change. Very little work has been done to understand how cation selection and/or choice of entropy-sublattice affects the structural response and phase stability in HEOs. In this thesis, high-temperature X-ray diffraction (HTXRD) is used to probe the changes in structure and lattice parameter of the HEO materials from room temperature up to 1200˚C to determine the thermal expansion. Each single-phase sample was either ground into a powder or pressed into half inch pellets and placed into the ceramic holder. A PANalytical Empyrean multipurpose diffractometer (Cu K$\boldsymbol{\alpha}$1 radiation, λ = 1.54059 Å) with an Anton-Parr furnace stage that reaches temperatures up to 1200˚C in air or inert gas atmospheres was employed for the collection of XRD data. Following scans at room temperature (25˚C) and 100˚C, subsequent scans were run with temperature increments of 100˚C up to 1200˚C in air. Once the temperature had stabilized at each 100-degree increment, XRD data would be collected. Sequential Rietveld refinements using the GSAS-II software [92] were conducted on each HEO sample and

expansion coefficients were determined from the obtained lattice parameters, as discussed in Chapter 6.

3.3 Microscopy and Microstructure Analysis

3.3.1 Scanning Electron Microscopy and Energy Dispersive X-ray (SEM/EDX)

Scanning electron microscopy and electron dispersive X-ray (SEM/EDX) are techniques commonly used for the analysis and determination of a material's surface topography and composition. This process involves an electron beam interacting with the sample surface producing X-rays distinctive to the elements in the material. Sample purity, stoichiometric balance of the elements, and composition homogeneity can be determined by this characterization technique.

Microscopy of the samples' surface was performed using a ZEISS EVO scanning electron microscope (SEM) with Bruker xFlash 6130 energy dispersive X-ray spectrometer (EDXS). Compositional mapping was performed to determine micron-scale homogeneity of the mixed rare-earth oxides. The elemental composition at specified areas on the polycrystalline pellets and single crystal surfaces was analyzed to confirm the stoichiometric ratios of each element in each sample.

3.3.2 HAADF-STEM EELS/TEM

The STEM-EELS and TEM work were used briefly in two separate studies in this dissertation. The specifics of the conditions and analysis are provided in Chapters 4.2 and 5.2 and, therefore, will not be discussed here.

3.4 Magnetization and Magnetic Susceptibility

3.4.1 Bulk Magnetization

A Quantum Design Magnetic Property Measurement System (MPMS 3) was employed to study the HEOs' response to a magnetic field. This device is highly sensitive to magnetic moments at varying temperatures and changes in magnetization given a magnetic field. For the new HEOs, DC susceptibility and magnetization versus field measurements were carried out to gain a better understanding of the overall magnetic behavior, including effective magnetic moments and Curie-Weiss temperatures. Susceptibility measurements were conducted from 2 to 300 K with a field of 1000 Oe under zero field cooled (ZFC) conditions. M vs. H measurements were carried out at 300 K and 2 or 3 K in fields up to 7 T. AC susceptibility data were also collected for one single crystalline composition at very low temperatures (below 1 K) at the National High Magnetic Field Laboratory in Tallahassee, Florida as discussed in chapter 4. DC susceptibility curves, experimentally derived effective magnetic moments, and Curie-Weiss temperatures for each composition can be found in Appendix E.

3.4.2 Magnetic Frustration in Pyrochlore Oxides

The magnetic properties of rare-earth pyrochlore oxides with structure $A_2^{3+} B_2^{4+} O_7$ have stirred excitement and intrigue in condensed matter science in the past 30 years [25] mostly due to the geometric frustration common to the structure. When the A and/or B sublattices are occupied by magnetic ions, and the magnetic interactions are antiferromagnetic in nature, the network of corner-sharing tetrahedra (Figure 3.2) leads to a "competition" of interactions, known as geometric frustration. An illustration of this phenomenon is shown in Figure 3.3 representing geometric frustration as Ising spins where the moments behave antiferromagnetically.

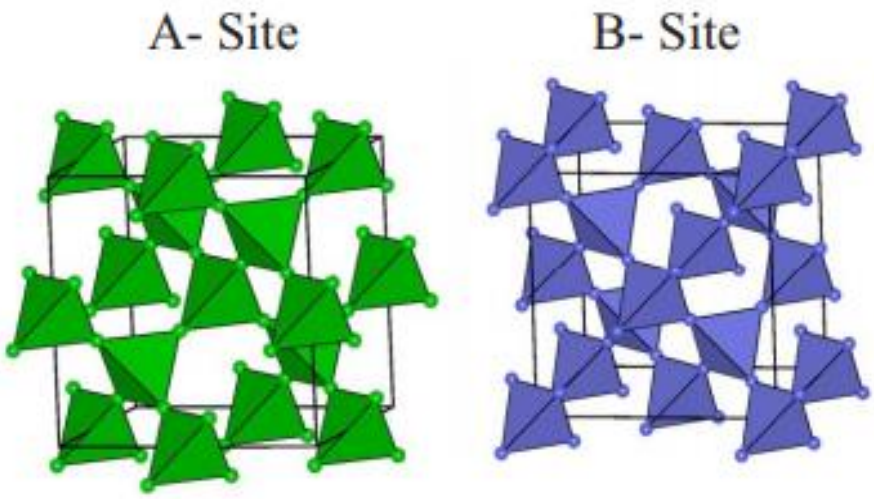

Figure 3.2: The cubic pyrochlore A and B sublattices [25].

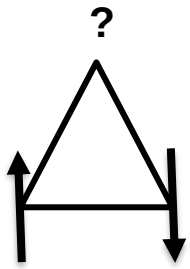

Figure 3.3: Frustration of antiferromagnetic spins on a triangular lattice.

In cubic rare-earth pyrochlores, rare-earth cations reside on the A^{3+} while the transition metal cations reside on the B^{4+} site. The A-site or B-site can have the magnetic ions, or both sites can have magnetic ions, creating an even higher degree of frustration. It has been previously discovered that many rare-earth pyrochlore oxides cannot develop long range magnetic order due to its geometrically frustrated lattice. Instead, unusual magnetic behavior develops when the materials are cooled down to very low temperatures. For a frustrated system, having a form of measurement to determine the extent of frustration in the system is desirable. The frustration index *f*, which was first introduced by Ramirez [93], measures the level of frustration for a magnetic material.

$$f \equiv \frac{|\theta_{CW}|}{T^*} \qquad (3.1)$$

For this equation, θ_{CW} represents the Curie-Weiss temperature and T^* is the critical temperature or Néel temperature where the system transitions to long range order [25]. For a system to be highly frustrated, the critical temperature T^* must be very low compared to θ_{CW}.

There are three known types of magnetic spin systems due to frustration: spin glass, spin ice, and spin liquid. The spin glass state can be briefly summarized as a "quenched" disordered system or, more specifically, the freezing of mixed spins that are randomly interacting, occurring at the spin-glass temperature [25,94]. Below this specified temperature, long-range ordering ceases to exist. There are two important conditions that must be met to have a spin glass: randomness of the spin positions and frustration due to the competition between nearest-neighbor interactions [25-27,94]. There have been several techniques for experimentally determining the spin glass state. Some of these include AC susceptibility measurements that involve a frequency dependence of χ', low temperature heat capacity measurements and its linear temperature dependence, and the nonlinear magnetic susceptibility temperature dependence [25-27,95].

3.5 Resonant Ultrasound Spectroscopy (RUS)

3.5.1 Concept

Resonant ultrasound spectroscopy (RUS) is a nondestructive technique developed by Migliori et al. [96] to determine the elastic moduli of a material. In an RUS experiment, an ultrasonic wave is sent through a solid material, producing a set of resonant frequencies unique to the material [96,97]. The frequencies at which these free-body resonances occur depend on the sample's shape and dimensions, as well as its elastic tensor. Therefore, experimental determination of the resonant frequencies, along with the sample's dimensions, allows us to determine the full elastic tensor of a solid material. Samples are typically shaped into a rectangular parallelepiped or cylinder, and the resonances can be tracked as a function of temperature and/or magnetic field, allowing to detect structural and magnetic transitions.

The utilization of a fitting procedure aids in the determination of the full elastic tensor of a solid material shaped as either a rectangular parallelopiped or cylinder. This is represented by a two-step process involving the computation of the resonant frequencies from the elastic constants (direct problem) and the calculation of the elastic constants from the resonant frequencies (inverse problem). While the direct problem is a straightforward calculation, taking into account the elastic tensor and dimensions of the sample, the inverse problem requires a nonlinear optimization procedure, using a "figure of merit" represented by:

$$F = \sum_{i=1}^{N} w_i (f_i - g_i)^2 \qquad (3.2)$$

where w_i is the weighing factor (either 1 or 0) and f_i and g_i represent the calculated and measured frequencies vectors. The calculated frequency is based on the direct calculation using an "educated guess" of the elastic tensor.

3.5.2 RUS Sample Preparation

RUS measurements require high quality samples with no porosity, cavities, or cracks. To prepare samples for RUS measurements, dense polycrystalline pellets are shaped into rectangular parallelepipeds. Similarly, cubic single crystals are cut, aligned with faces perpendicular to the [100] axis, and then shaped into rectangular parallelepipeds. The mass and dimensions must be obtained to determine the density of the material, which is used in the nonlinear optimization procedure. In this dissertation, HEO and select single component pyrochlore samples measured with RUS were either single crystals grown from an optical floating zone furnace or polycrystals synthesized by solid state reaction. All samples were carefully shaped into rectangular parallelepipeds by polishing the surfaces to achieve 90-degree angles and flat surfaces. HEO single crystals were cut from large crystal rods into smaller pieces using a diamond blade saw. Laue diffraction was used to determine crystal quality and align the cut crystal pieces so that the [100] axis could be identified, and the sample was polished with the [100] axis perpendicular to the faces.

To obtain dense polycrystals for RUS measurements, a uniaxial hot press (OXYGON industries (Model No. FR210-25T-A-200-04T)) was used for one HEO and two single-component pyrochlore compositions for sintering at high temperatures and apply pressure simultaneously. This creates a polycrystalline ceramic with less porosity, making for a more adequate test sample for RUS measurements. Single phase pyrochlore powders were initially pressed into disc pellets using a hydraulic press, then placed into a graphite die with graphite sheets surrounding the sample. Once loaded into the equipment, a constant pressure of 0.6 tons (45 MPa) was applied with temperatures between 1400˚C and 1500°C for 12 to 20 hours. The samples were then polished to remove excess graphite from the surface and then heated again to burn off any remaining graphite. The samples were then polished and shaped to rectangular parallelopipeds for measurement.

3.5.3 RUS Procedure and Analysis

Samples are placed between two piezoelectric transducers and mounted on its edges, corners, or flat on its faces. Figure 3.4 illustrates this setup with a sample positioned on its corners. Frequencies are typically measured and collected between 100 to 2500 kHz. An electromagnetic signal is generated by the frequency generator and then converted into an acoustic wave at the top transducer. The wave travels through the sample, generating resonances that are converted back into an electromagnetic signal at the bottom transducer. Figure 3.5 shows part of a typical resonance spectrum obtained. Measured resonance frequencies are unique to the sample in question. Elastic moduli fits are typically obtained from the collection of the first 30 to 50 resonances, however more resonances can be used. For cubic single crystals, there are three independent elastic constants (one longitudinal and 2 shear moduli) and for polycrystals there are two (one longitudinal and one shear modulus). Table D2 in Appendix D shows an example of the output file from an RUS fit. It lists the experimentally collected resonances as well as the calculated resonances based on sample density and estimated elastic constants. In addition, it shows the root-mean-square (rms) percent errors for each mode, and how each frequency is affected by a change in elastic moduli.

3.5.4 RUS for Probing Structural Phase Transitions

When tracking a material's resonances with temperature, materials that possess no thermodynamic "irregularity" will show a gradual increase in resonant frequencies with decreasing temperature, corresponding to an elastic stiffening. However, when a structural or magnetic transition takes place, the temperature-dependence of the tracked resonances (and thus elastic moduli) often shows a change in slope or abrupt change. The elastic constants will typically show noticeable discontinuities at second-order transitions due to the effects of coupling between strain and the order parameter (Q).

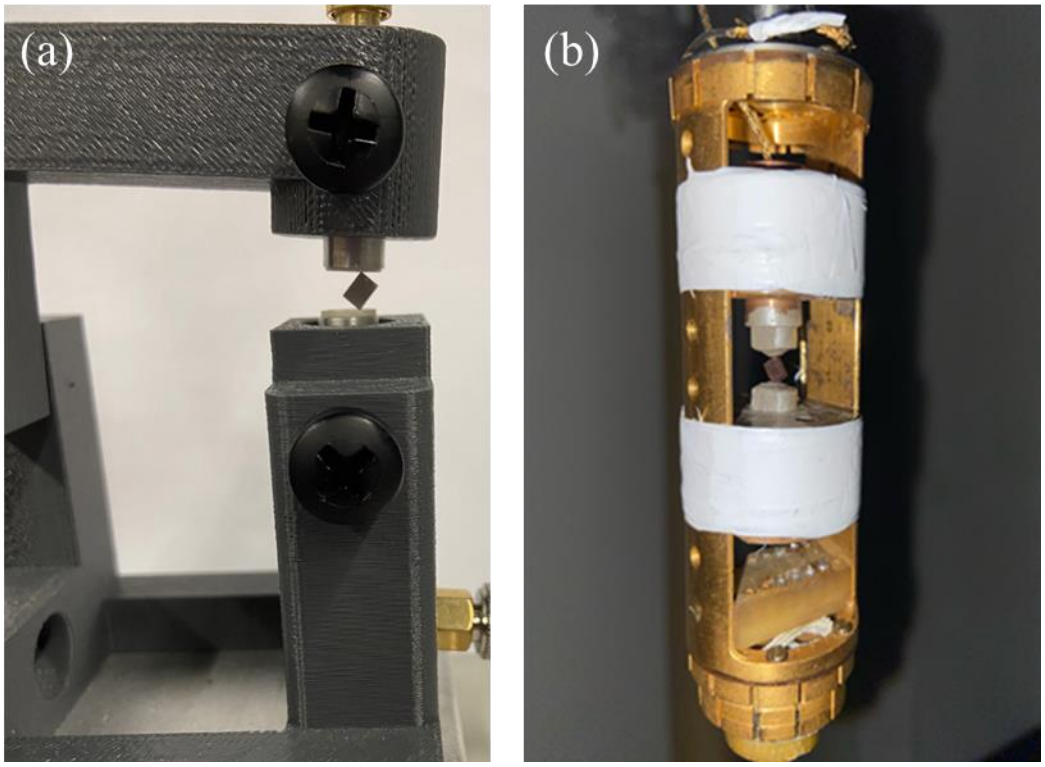

Figure 3.4: (a) Room temperature RUS probe typically used with digital RUS system. (b) In-house designed RUS probe used for measurements as a function of temperature in a PPMS or VersaLab system with rectangular parallelepiped shaped crystal positioned between two transducers.

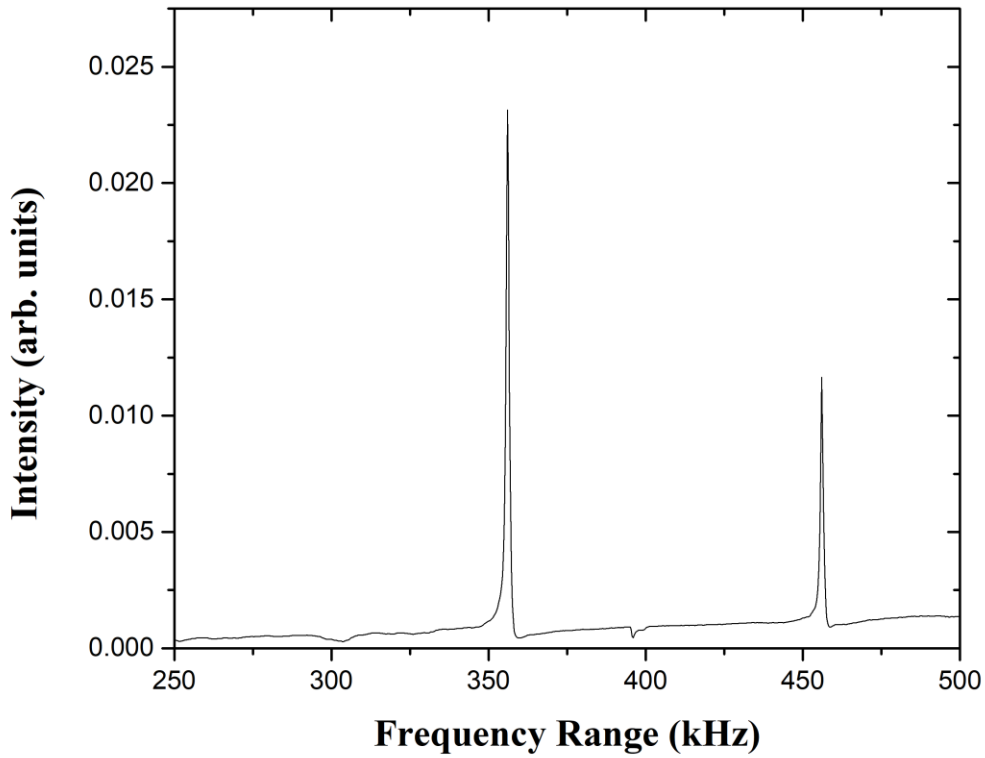

Figure 3.5: Example of a typical resonance spectrum.

3.6 Ion-Irradiation and Rutherford Backscattering Spectrometry (RBS)

3.6.1 Purpose and General Concept

In an ion-irradiation experiment, a material is subjected to energetic ions (ionizing radiation) from an ion accelerator. This experimental technique allows for the study of a material's radiation resistance for nuclear applications and for the use of ions to modify material properties. It has been commonly used to evaluate the radiation stability of ceramic materials, such as pyrochlores, for nuclear waste storage [98,99]. Single crystal samples are first aligned to have the crystal positioned in a direction along a major axis perpendicular to the sample surface and then polished to a "mirror finish". In order to characterize the quality of the single crystals and to quantify the radiation damage, energetic light ions, such as helium ions, are aligned along a major crystallographic direction (i.e., an ion channel), and Rutherford backscattering spectrometry of the incident light ions is used to determine the local crystalline disorder as a function of depth. This ion beam analysis approach is generally referred to as ion-channeling, or specifically as Rutherford backscattering spectrometry in channeling geometry (RBS/C) when the backscattered particle is due to Rutherford scattering, and not non-Rutherford scattering or nuclear reactions The choice of ion type and energy used for the RBS/C measurements is based on the sample composition, density and the depth to be probed. Along with the use of ion-channeling for the damage analysis, the Stopping and Range of Ions in Matter (SRIM) set of packages is employed to determine the depth distribution of ion-induced damage, including the depth of peak damage, and the local damage dose for a given set of experimental parameters. As noted, Rutherford backscattering spectrometry (RBS) is typically used to determine the damage evolution, along with an iterative procedure to develop a quantitative damage profile [98,99].

The intention of the ion-irradiation experiments in this dissertation is to induce irradiation damage in a single crystalline HEO pyrochlore, analyze the accumulation of damage with increasing ion fluence, and assess this damage evolution by comparing the resulting disordering behavior with previously reported single rare-earth pyrochlore oxides. Raman spectroscopy, ion channeling techniques, and Transmission Electron Microscopy (TEM) analysis are used to characterize damage results.

3.6.2 Ion-Irradiation Procedure

This section is provided to describe the general procedure of ion irradiation. Further discussion and details on the specifics of the conditions applied to the HEO pyrochlore crystal are provided in Chapter 5. A Tandem ion accelerator located at the University of Tennessee, Knoxville's Ion Beam Materials Laboratory (UT-IBML) with a ~ 3 MeV (maximum terminal voltage) was employed for the irradiation studies of the HEO single crystals [100]. Two sources were used for this study: one is the Alphatross, which produces He ions for ion channeling, and the second is the SINCS (Source of Negative Ions by Cesium Sputtering) which produces a large variety of negative ions from C to Au by sputtering and Cs vapor charge exchange. The negative ions are injected into the tandem accelerator and accelerated to higher energies by the positive potential created by the high-voltage terminal shell in the middle of the accelerator. These accelerated negative ions pass through an exchange chamber of low-pressure nitrogen gas in the terminal shell which removes electrons producing positive ions that are further accelerated until they exit the accelerator. Since the ions exiting the accelerator can have different charge states and energies, the ions of interest are magnetically separated into one of three beamlines, where they are focused and steered onto the target sample for irradiation or RBS/C analysis.

As previously mentioned, SRIM software packages were used to determine reasonable experimental parameters. The stopping power (energy loss per unit distance) tables for any ion or solid can be determined up to 2 GeV/amu, separated into electronic and nuclear stopping power components. A Monte Carlo algorithm for estimating ion ranges and energy loss and damage production profiles production is also included with SRIM. The SRIM calculations in this dissertation were conducted under full cascade mode for obtaining accurate approximations of the depth profiles of atomic displacements and implanted ions. The threshold displacement energies for all the ions in the target material were set to 50 eV [101] and an experimentally derived density of 7 g/cm^3 was used in the SRIM simulations. The local damage dose in displacements per atom (dpa) is determined using output files (VACANCY.txt and NOVAC.txt) generated from SRIM and expressed in Equation 3.3:

$$dpa(x) = \frac{\nu(x)}{\rho} \tag{3.3}$$

where $\nu(x)$ is the local number of displacements (vacancies plus replacements) per cm ion at depth x and ρ is the atomic density (atoms cm^{-3}). This equation gives an estimate of the number of atomic displacements generated from the irradiation exposure. The depth profile of implanted ions was determined from the Range.txt file generated in the SRIM calculations.

The single crystal sample irradiated in this study was ~ 9 mm in length with a width ranging from 2 to 4 mm. Figure 3.6 shows the crystal fixed to the holder using carbon tape for room temperature ion irradiation. Two separate experiments were carried out on the same single crystal sample using 4 MeV Au ions. The crystal was divided into two irradiation sections labeled A and B to specify the locations for the various applied fluences, as shown in Table 3.2. After Experiment 1 was concluded, the crystal surface was repolished to a mirror finish to remove the damaged surface layer in preparation for Experiment 2.

3.6.3 Rutherford Backscattering Spectrometry (RBS) and Ion Channeling

Rutherford Backscattering Spectrometry (RBS) is an analysis technique that measures the energy spectrum of backscattered ions from a material that is bombarded with high energy light ions. These collisions between the incident probe ion and the target ion are elastic in nature. Those backscattered ions in a small solid angle are measured by a silicon detector that is positioned at a specific angle from the surface, allowing the energy spectrum of the backscattered ions in that solid angle to be quantified. This process allows for the determination of the backscattered ion's energy, which is plotted as counts versus the channel number (energy). Different elements with differing masses will scatter ions at different energies and angles. This variation in energies produces peaks or "edges" on the counts versus channel plots, which are characteristic of the material's elements and is typically witnessed if the backscatter is collected on a material with random geometry (off channel). Therefore, RBS can determine elemental composition of a material over some depth.

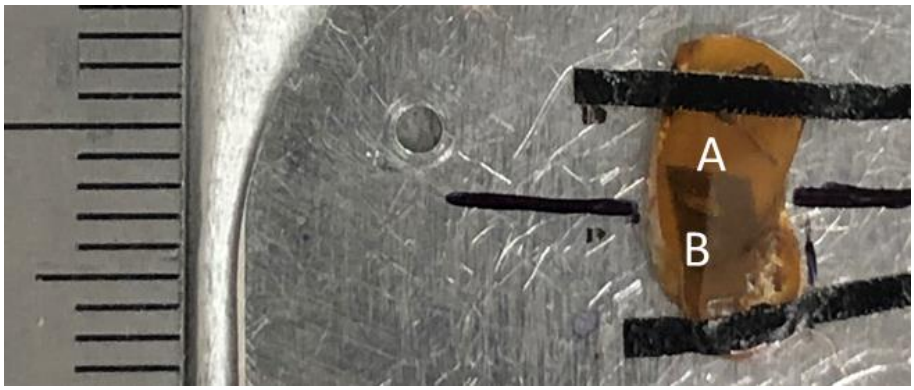

Figure 3.6: HEO single crystal mounted on the sample stage for room temperature ion irradiation of 4 MeV Au^{2+} ions with two irradiation areas labeled A and B.

Table 3.2: Ion-irradiation experiments, irradiation rounds, and ion fluences for each area on HEO single crystal $(YbHoTmErLu)_2Ti_2O_7$. Ion fluences are in ions/cm^2.

	Experiment 1		Experiment 2	
Irradiation Round	**Area A Fluences**	**Area B Fluences**	**Area A Fluences**	**Area B Fluences**
1	1×10^{13}	4×10^{13}	5×10^{12}	1.5×10^{13}
2	2×10^{13}	5×10^{13}	2.33×10^{13}	2.66×10^{13}
3	3×10^{13}	6×10^{13}	3.33×10^{13}	3.66×10^{13}

In addition, the depth distribution of implanted ions can be deduced by RBS. When the RBS probe ion (such as He) is scattered from the surface of a sample, the backscattered ion energy is discretely large. In contrast, when the RBS probe ion penetrates into the sample bulk, energy will be lost continuously as a consequence of the nuclear and electronic stopping powers for the ion in the sample. As a result, the backscattered depth can be discovered from the overall energy loss of the backscattered ion and experimentally predicted stopping powers.

As previously described, materials that contain atoms arranged in a random order will produce a lot of backscatter, resulting in higher counts measured by RBS. However, when a major crystallographic direction of a single crystal is aligned along the path of the incident high energy ions, rows of organized atoms will be revealed along with open “channels” where energetic ions can travel through by low angle scattering (Figure 3.7). When this occurs, significantly less backscattering is produced and detected. Therefore, low RBS yield (~ 10% or less) is produced in comparison to the random spectrum. Because of this phenomenon, the combination of Rutherford backscattering spectrometry and ion channeling geometry (RBS/C) can be used to detect impurities and defects in crystalline materials [102-104]. In our study, RBS/C is employed for the HEO single crystal irradiation study discussed in Chapter 5, allowing us to track and determine the damage and degree of amorphization.

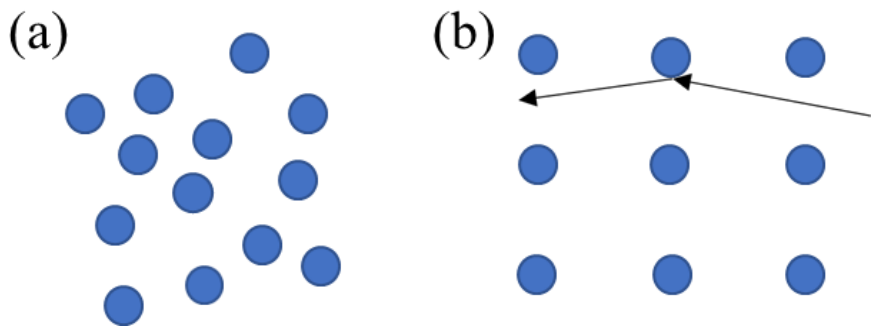

Figure 3.7: (a) Material with random order (leads to more backscatter) and (b) a single crystal aligned so that rows of atoms (blue dots) are incident with the ion beam. The trajectory of a high energy ion is represented by the black arrows depicting low-angle scattering.

CHAPTER FOUR
SYNTHESIS, CHARACTERIZATION, AND SINGLE-CRYSTAL GROWTH OF A HIGH-ENTROPY RARE-EARTH PYROCHLORE OXIDE

A version of this chapter was originally published by Candice Kinsler-Fedon *et. al.*: C. Kinsler-Fedon, Q. Zheng, Q. Huang, E.S. Choi, J. Yan, H. Zhou, D. Mandrus, and V. Keppens, Synthesis, characterization, and single-crystal growth of a high-entropy rare-earth pyrochlore oxide, Physical Review Materials, 4, 104411 (2020). [39]

In this chapter, we report the synthesis, single crystal growth, X-ray diffraction, atomic-scale structure analysis, and magnetic property analysis of the high entropy pyrochlore oxide $(Yb_{0.2}Tb_{0.2}Gd_{0.2}Dy_{0.2}Er_{0.2})_2Ti_2O_7$.

4.1 Introduction

The magnetic behavior in rare-earth pyrochlore oxides has been heavily investigated for decades [24-27,55]. The addition of multiple rare-earth cations to the geometrically frustrated sublattice site of the pyrochlore structure could potentially lead to new magnetic behavior given the complexity of the interactions. This report discusses the successful synthesis of $(Yb_{0.2}Tb_{0.2}Gd_{0.2}Dy_{0.2}Er_{0.2})_2Ti_2O_7$ or $(5RE_{0.2})_2Ti_2O_7$ HEO pyrochlore, its single-crystal growth using the optical floating-zone technique, and characterization of its structure and magnetic properties, identifying nanoscale-level mixed occupation of the rare-earth cations in the pyrochlore phase and significant evidence of an exotic magnetic ground state. Configurational entropy was chosen for the A site of the $RE_2Ti_2O_7$ system because each rare-earth cation forms a pyrochlore in its single-component form, obeying the A-site to B-site cation ratio rule (1.36–1.78, roughly) needed to form the (227) structure [51]. All five rare-earth cations are magnetic, and configurational entropy on this sublattice is expected to be a good starting point for discovering novel materials with possible spin-glass or spin liquid ground states.

4.2 Experimental Procedure

Generalized descriptions of the experimental methods and instrumentation used are provided in Chapter 3. This section is provided to explain the specific details for this study. Solid-state reaction was used to form a single-phase polycrystalline $(5RE_{0.2})_2Ti_2O_7$. Starting reactants were Yb_2O_3 (99.9%), Tb_2O_3 (99.9%), Gd_2O_3 (99.9%), Dy_2O_3 (99.9%), Er_2O_3 (99.9%), and TiO_2 (99.9%). The rare-earth oxide starting components were dried overnight at 1073 K in air. The dried powders were weighed at room temperature, combined, and mixed using a vibratory ball mill (SPEX 8000M Mixer/Mill) in a polypropylene grinding vial with two 12.7-mm methacrylate mixing balls for over an hour. The powder was pressed into a pellet, which was heated in a high-temperature box furnace at 1673 K for 20 hours in air. The pellet was removed, the x-ray diffraction pattern was checked, and reheated for another 20-hour heat treatment. This process was repeated (approximately 3–4 times) until a single-phase x-ray diffraction pattern was observed. Single crystals were grown using the floating-zone crystal growth technique with a two-mirror optical floating-zone furnace (Canon Machinery model SC1-MDH) and 1500-W halogen lamps. The single-phase powder was put into a balloon sleeve and pressed into a long rod pellet using a water cell press. The rod was heated at 1673 K for 20 hours and prepared for single-crystal growth as described in Chapter 3, section 1.2. Growing conditions for the $(5RE_{0.2})_2Ti_2O_7$ crystal growth consisted of an oxygen atmosphere at a pressure of 0.3 MPa and a growth rate of 15–20 mm per hour. The rods were counter-rotated at 20–25 rpm. Scanning transmission electron microscopy (STEM) measurements were conducted for further confirmation of a single-phase structure and homogeneous distribution of the rare-earth cations. Single-crystalline and polycrystalline $(5RE_{0.2})_2Ti_2O_7$ samples were crushed in ethanol. Drops of the resulting suspensions were deposited on lacey carbon TEM grids and dried in air for STEM observations. High-angle annular dark-field (HAADF) imaging and electron-energy loss spectroscopy (EELS) were performed using a Nion UltraSTEM100 equipped with a cold field-emission gun and a corrector of third- and fifth-order aberrations, operated at an accelerating voltage of 100 kV. HAADF-STEM images were collected with a probe convergence angle of 30 mrad and an inner collection angle of 86 mrad. EEL spectra were collected using a Gatan Enfinium spectrometer (Gatan Inc.) with a dispersion of 0.5 eV per channel and collection

semiangle of 48 mrad. A superconducting interference device magnetometer (Quantum Design MPMS) was employed for the DC susceptibility measurements for the polycrystalline and single-crystal samples with an applied magnetic field of 1000 Oe and data were taken between 3 and 300 K. For the single crystal, the DC susceptibility was measured with the field parallel to the [100] direction. Magnetization versus field (M vs H) measurements were recorded using magnetic fields up to 7 T. Low-temperature (0.3–1.7 K) AC susceptibility measurements were performed at the National High Magnetic Field Laboratory with frequencies ranging from 47 to 995 Hz and magnetic fields up to 1 T. Laue diffraction, X-ray diffraction, and scanning electron microscopy analysis are as described in Chapter 3 using the instrumentation provided therein.

4.3 Results and Discussion

X-ray diffraction data and structure refinement recorded for polycrystalline $(5RE_{0.2})_2Ti_2O_7$ (Figure 4.1) shows that the multicomponent oxide has a cubic structure and belongs to the $Fd\bar{3}m$ space group. The diffraction pattern matches closely with the patterns of the standard cubic pyrochlore rare-earth titanates. Results of the structure refinement, including refined crystallographic parameters and powder x-ray diffraction data, are listed in Appendix B. The lattice parameter was found to be 10.1152(3) Å for $(5RE_{0.2})_2Ti_2O_7$, which is comparable to the single rare-earth component titanate pyrochlores from literature [34,54,105-107] listed in Table 4.1. The lattice parameter for $(5RE_{0.2})_2Ti_2O_7$ falls in between the lattice parameters of $Yb_2Ti_2O_7$ and $Dy_2Ti_2O_7$, consistent with an even proportion of each rare-earth ion on the rare-earth site of $(5RE_{0.2})_2Ti_2O_7$. This result is expected given that the average ionic radius is ~ 1.0218 Å for the five rare-earth cations, which falls between Dy^{3+} (1.027 Å) and Yb^{3+} (0.985 Å). The final refinement results, which include setting values to the instrument parameters (U, V, W) and refining the instrument parameter "X" to improve the reflection intensities, are very reasonable with values for the wRp = 6.34%, R_{exp} = 4.38%, and the goodness of fit χ^2 = 1.45.

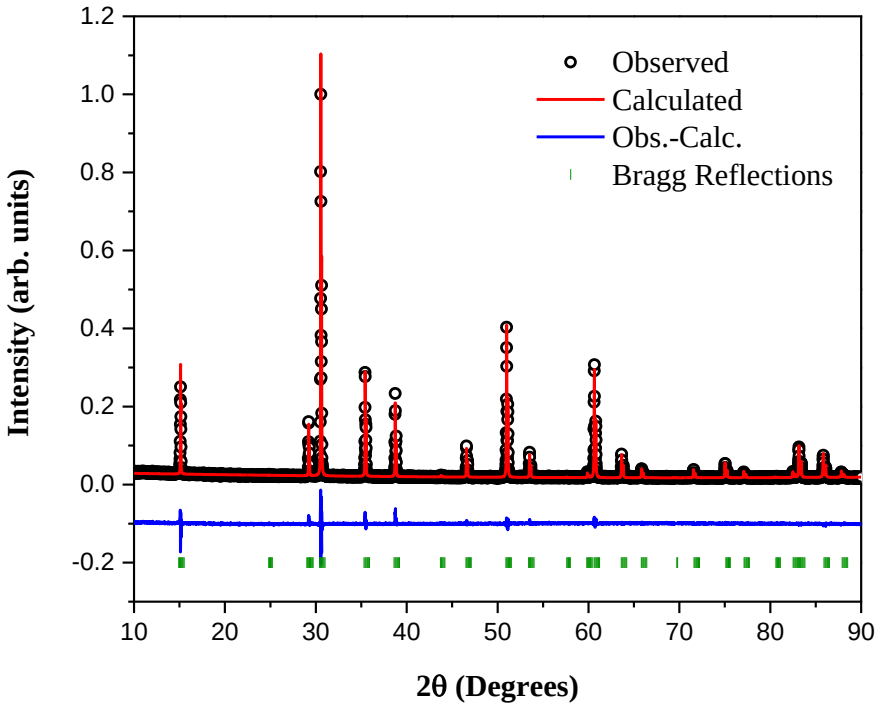

Figure 4.1: Room temperature powder X-ray diffraction pattern of polycrystalline $(5RE_{0.2})_2Ti_2O_7$. The refinement pattern (red line) overlays the observed pattern (black circles) which matches the $Fd\bar{3}m$ cubic structure (green vertical dashed lines are the Bragg reflections characteristic of the pyrochlore phase). The difference pattern is represented in blue below the diffraction pattern.

Table 4.1: List of comparable lattice parameters of the single-component rare-earth pyrochlore titanate oxides and HEO rare-earth pyrochlore titanate.

Rare-Earth Titanate Pyrochlore Compounds	Lattice Parameter (Å)	Reference
$Yb_2Ti_2O_7$	10.09	[34]
$Tb_2Ti_2O_7$	10.158	[105]
$Dy_2Ti_2O_7$	10.131	[106]
$Er_2Ti_2O_7$	10.086	[107]
$Gd_2Ti_2O_7$	10.184	[54]
$(Yb_{0.2}Tb_{0.2}Gd_{0.2}Dy_{0.2}Er_{0.2})_2Ti_2O_7$	10.1152(3)	

Single crystalline $(5RE_{0.2})_2Ti_2O_7$ was grown using the floating zone growth technique, with growing conditions as described in the Experimental Procedure. Figure 4.2(a) shows the resulting ingot of the single crystal growth, approximately 7 cm in length. The ingot has a brownish red color and is translucent. X-ray diffraction verified that the multi-crystal was of the cubic pyrochlore phase, confirming that it did not change phase during growth (Figure B1 in Appendix B). Laue diffraction was used to determine crystal quality (Figures 4.2(b)-(d)) and indicates that the ingot contained multiple crystals of good quality ranging in size from 4 mm to 2 cm.

A former study of growing the single component rare-earth titanate oxides using the same crystal growth technique reported success with slower growth rates ranging from 2.5 to 4 mm per hour [108], however, these rates were not successful for the HEO rare-earth pyrochlore. Multiple attempts to produce a completely single domain crystal by using slower growth speeds ranging from 2 to 10 mm per hour resulted in unstable growth environments with bubble pocket formation or detachment of the molten zone. Adjusting the pressure from 0.3 MPa to 0.2 MPa and pulling the crystal through the heated zone twice also had no improvement on the quality of the crystal. Growing the crystal at a rate between 15 to 20 mm per hour was our growth speed of choice and produced a more stable growth overall. Improvements on the growth technique to obtain a larger high-quality single crystal will need further experimentation.

Scanning Electron Microscopy (SEM) and Energy Dispersive X-Ray (EDX) analyses were conducted on both the polycrystalline and single crystal samples. A comparison of the compositions and elemental percentages in specific areas of each sample is shown in Figure 4.3 and Table 4.2, along with chemical composition mapping of $(5RE_{0.2})_2Ti_2O_7$ polycrystal at 10 µm showing compositional uniformity of the five rare-earth cations at this scale (Figure 4.4).

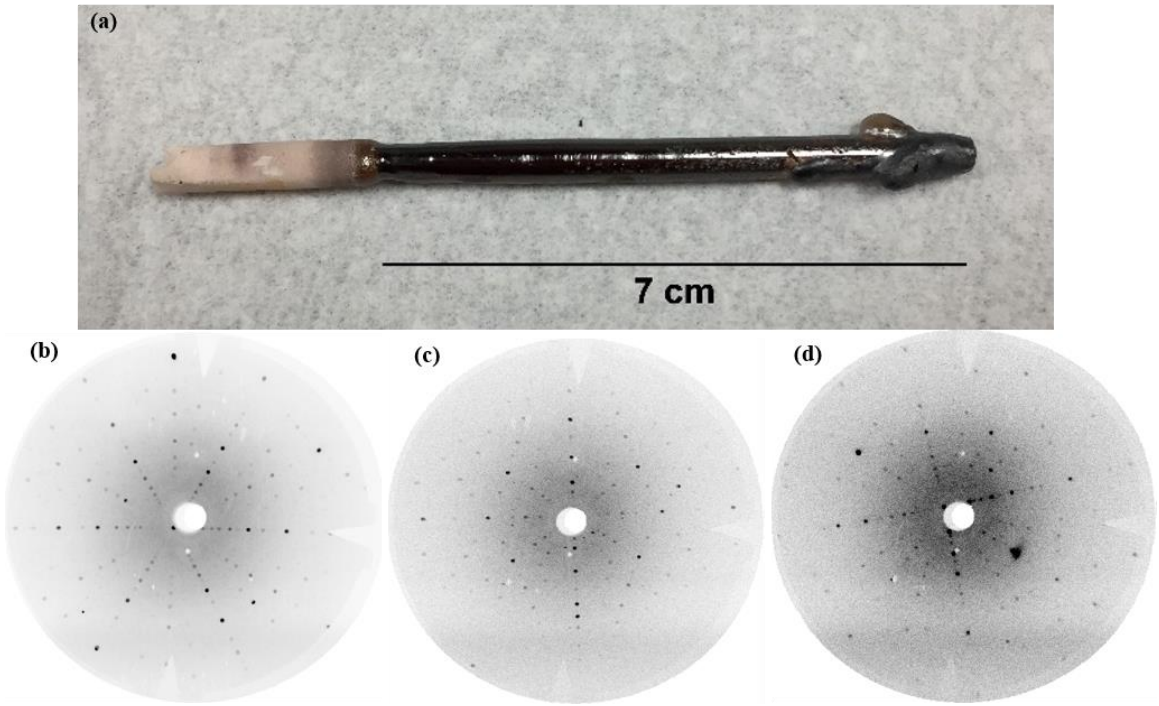

Figure 4.2: (a) Resulting multi-crystal of $(5RE_{0.2})_2Ti_2O_7$ of ~7 cm in length. (b)-(d) Laue diffraction patterns of $(5RE_{0.2})_2Ti_2O_7$ taken from various sections of the ingot showing good quality with (b) aligned in the [111], (c) in the [110], and (d) in the [100].

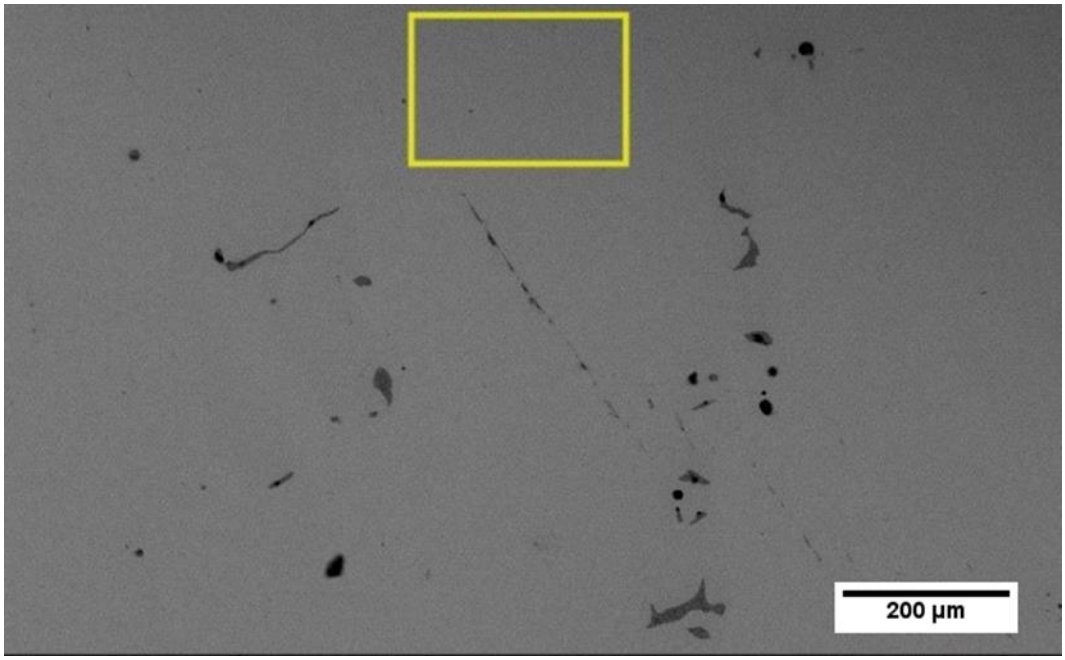

Figure 4.3: SEM image at 200 µm and area scan of single crystal $(5RE_{0.2})_2Ti_2O_7$.

Table 4.2: Area scan concentration data for single crystal $(5RE_{0.2})_2Ti_2O_7$.

Element	Atomic Number	Mass Concentration (%)	Mass Normalized (%)	Atom Concentration (%)	Absolute Error (%)
Oxygen	8	15.68	16.93	56.48	1.92
Titanium	22	19.29	20.84	23.22	0.56
Gadolinium	64	11.30	12.20	4.14	0.33
Terbium	65	11.63	12.56	4.22	0.34
Dysprosium	66	11.69	12.63	4.15	0.34
Erbium	68	11.26	12.16	3.88	0.33
Ytterbium	70	11.73	12.67	3.91	0.35
		92.58	100	100	

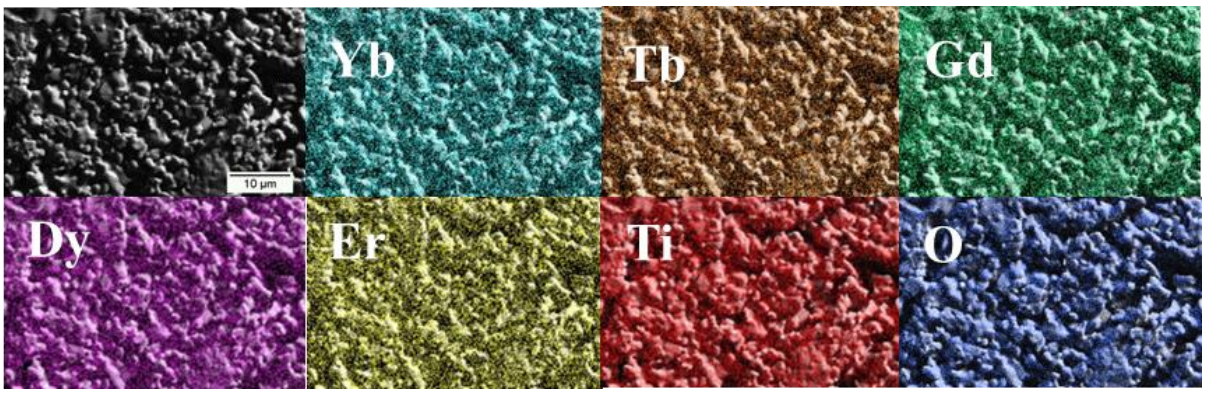

Figure 4.4: Elemental mapping of polycrystalline $(5RE_{0.2})_2Ti_2O_7$ showing homogeneity near 10 µm.

Given the configurational complexity of this new oxide, it is necessary to employ multiple microscopy methods to provide a better understanding of this material's structure and ion distribution at different scales. STEM-EELS was used to examine the homogeneity at smaller scales and further confirms a single-phase structure in both the single crystal and polycrystalline materials. In what follows, we will discuss the nanoscale and atomic analysis for the single crystal. .

The STEM observations were carried out along two main zone axes: [011] and [001], for both single crystalline and polycrystalline $(Yb_{0.2}Tb_{0.2}Gd_{0.2}Dy_{0.2}Er_{0.2})_2Ti_2O_7$. As shown in the inset in Figure 4.5(a), three types of cationic columns can be observed along the [011] direction, which consist of 100% heavier rare-earth atoms, 50% rare-earth atoms plus 50% Ti atoms, and 100% lighter Ti atoms, respectively. Since the HAADF image intensity is roughly proportional to Z^2 (Z is the atomic number), these three types of columns show brightest, intermediate, and weakest contrasts, respectively. No obvious local structural imperfections were observed in the single crystalline (Figure 4.5(a) and polycrystalline (Figure 4.5(b)) samples, indicating the mixed occupation of the five rare-earth elements maintains the pyrochlore structure, consistent with the XRD result.

In contrast, as depicted in Figure 4.6(a), along the [001] direction, each cationic column involves 50% rare-earth atoms plus 50% Ti atoms, suggesting an optimal zone axis for the uniformity analysis on the five rare-earth elements Yb, Tb, Gd, Dy and Er in this pyrochlore structure. A region with in-plane dimensions of 27 nm × 27 nm for the single crystalline sample (Figure 4.6(a)) was selected to analyze the distribution of the five rare-earth elements at different scales. Using the log-ratio method as described in [109,110] from the corresponding low-loss EEL spectrum (Figure 4.7(a)), the thickness for this region is calculated to be around 26 nm, *i.e.* 25 unit cells with 25 rare-earth atoms and 25 Ti atoms in each cationic column. The M_5-edges for these five rare-earth elements in the core-loss EEL spectra (Figure 4.7(b)) were used to acquire the chemical maps. Pixel size for the EEL mapping were first set to be around 0.7 nm × 0.7 nm, *i.e.* containing information of ~200 rare-earth atoms for each pixel. The obtained maps using their M_5-edges are shown in Figure 4.6(c)-(g), respectively. These maps suggest quite uniform distribution of these five rare-earth elements at such scale. Similar results were found for the polycrystalline sample using the same process described for the single crystal.

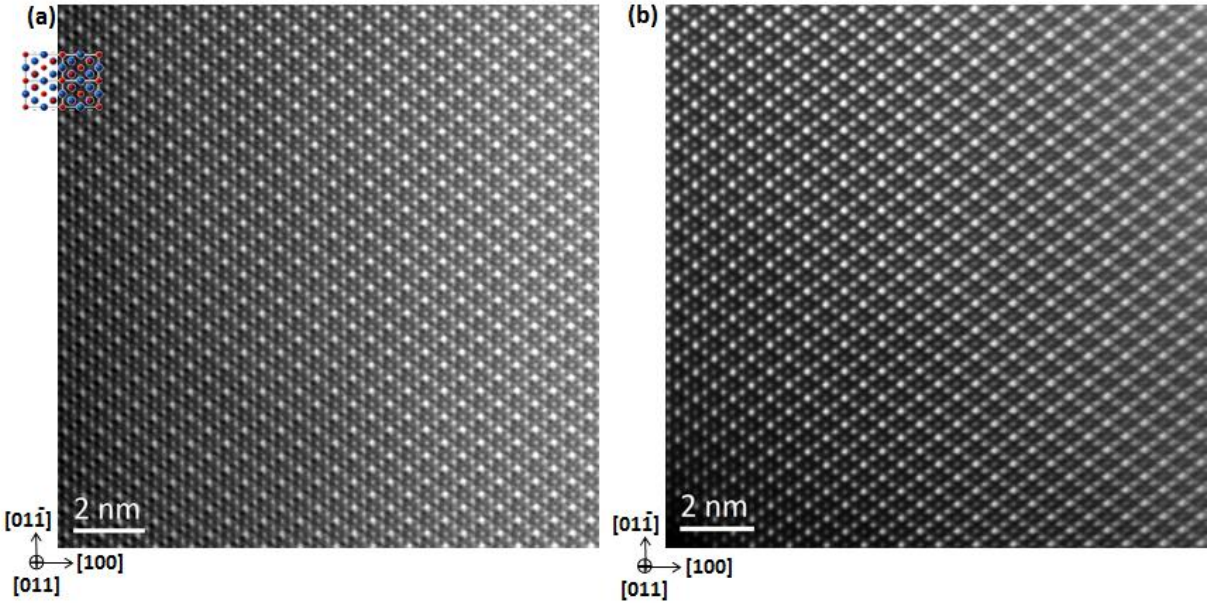

Figure 4.5: HAADF-STEM images along the [011] zone axis for (a) single-crystalline and (b) polycrystalline $(5RE_{0.2})_2Ti_2O_7$, respectively. The inset in (a) is the crystal structure in this projection, where only cations are shown (the red and the blue are Ti and rare-earth atoms, respectively). The intensity variations arise from three types of atomic columns along this direction. The columns with brightest, intermediate, and weakest contrasts involve 100% rare-earth atoms, 50% rare-earth atoms plus 50% Ti atoms, and 100% Ti atoms, respectively.

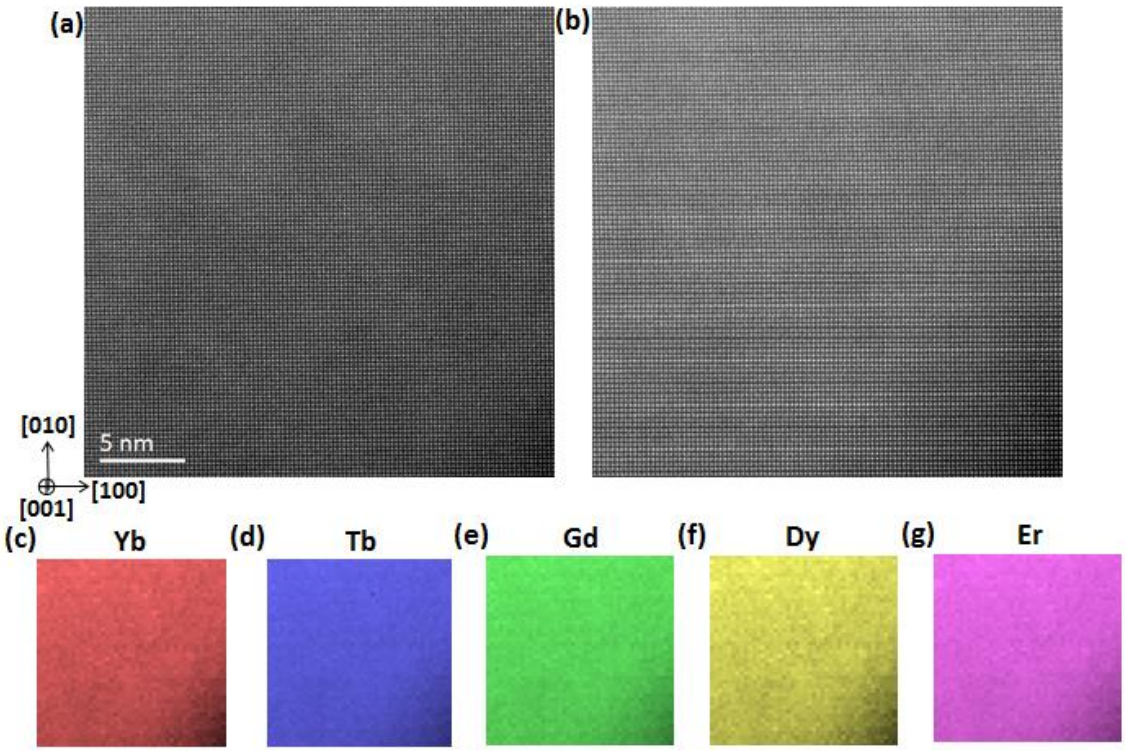

Figure 4.6: HAADF-STEM imaging and nanoscale electron-energy loss spectroscopy (EELS) mapping along [001] for the single crystalline $(5RE_{0.2})_2Ti_2O_7$. (a) Atomic-resolution HAADF image for the EELS mapping region with the dimension of 27 nm × 27 nm. (b)-(g) EELS mapping analysis: (b) HAADF image recorded simultaneously during the EELS data set acquisition; (c) Yb, (d) Tb, (e) Gd, (f) Dy, and (g) Er chemical maps obtained from their M_5-signals, respectively. Note that each pixel in EELS maps is scanned by 16 × 16 for the simultaneously recorded HAADF image in (b), resulting in atomic-resolution in (b) while nano-scale resolution in the EELS maps in (c)-(g).

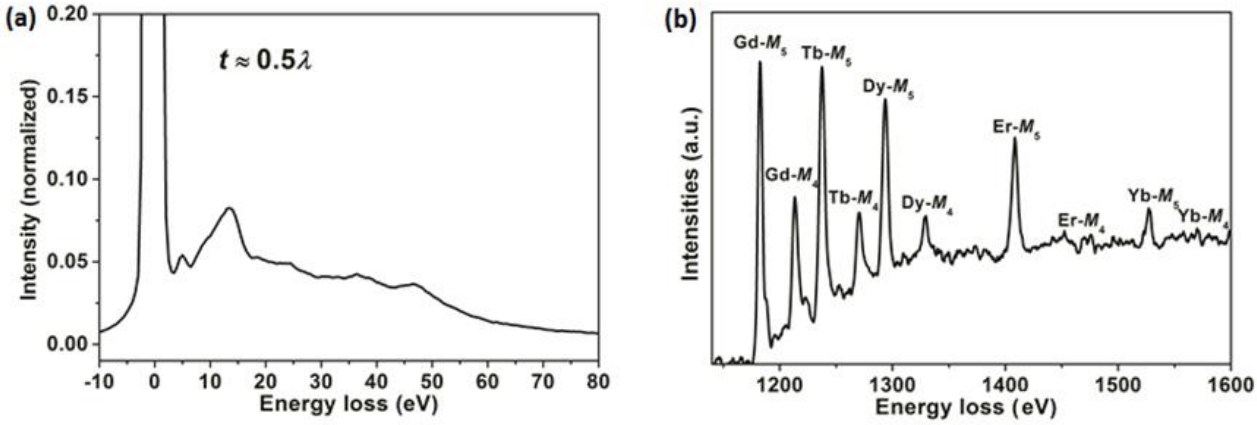

Figure 4.7: (a) Average low-loss electron-energy loss (EEL) spectrum for the region in Figure 4.6(a). The thickness for this region is calculated to be ~0.5λ using the log-ratio method, where λ is an inelastic mean free path. (b) Average core-loss EEL spectrum for this region shows the $M_{4,5}$ edges of Gd, Tb, Dy, Er and Yb, respectively.

It can be concluded from the STEM-EELS results that the five rare-earth cations in the $(5RE_{0.2})_2Ti_2O_7$ samples are distributed homogeneously down to ~2.3 nm.

Atomic-resolution EEL mapping were carried out to emerge the distribution of these five rare-earth elements in each atomic column, as demonstrated in Figure 4.8, which show an inhomogeneous distribution. Different with those maps in Figure 4.6 c-g, of which each pixel covers the chemical information of ~200 rare-earth atoms, the atomic scale chemical maps in Figure 4.8 reveals the chemical uniformity information of each rare-earth elements among only 25 total rare-earth atoms. 2.3 nm × 2.3 nm × 2.3 nm and 1.2 nm × 1.2 nm × 1.2 nm volumes then could be roughly calculated to involve ~200 rare-earth atoms and 25 rare-earth atoms, respectively. Therefore, these two different-resolution EELS mapping analysis suggests that the five rare-earth elements Yb, Tb, Gd, Dy and Er likely distribute homogenously in the single crystalline $(Yb_{0.2}Tb_{0.2}Gd_{0.2}Dy_{0.2}Er_{0.2})_2Ti_2O_7$ down to ~2.3 nm-scale.

The EELS mapping analyses were also carried out for the polycrystalline sample at different scales, as shown in Figure 4.9 and Figure 4.10, respectively. Similarly, the five rare-earth elements also appear to distribute homogenously down to ~2.3 nm-scale, but non-uniformly when the resolution goes down to ~1.2 nm-scale.

As a result, the HAADF images along the [011] and [001] zone axes for single crystalline and polycrystalline $(Yb_{0.2}Tb_{0.2}Gd_{0.2}Dy_{0.2}Er_{0.2})_2Ti_2O_7$ samples indicate the mixed occupation of the five rare-earth elements can still maintain the pyrochlore structure. Since the samples were not completely homogeneous at the atomic scale, this suggests that the rare-earth cations are not completely ordered (complete ordering would result in a superstructure lattice). This result is not surprising given that there are only 16 rare-earth sites in 1 unit cell × 1 unit cell × 1 unit cell (each unit cell ~ 1 nm), which explains why the 5 rare-earth cations would appear less homogenous below the 2 nm scale mark. Overall, the EELS maps for Yb, Tb, Gd, Dy and Er from nanoscale to atomic scale suggest relative homogeneity of these five rare-earth elements down to ~2.3 nm-scale in both single crystalline and polycrystalline samples.

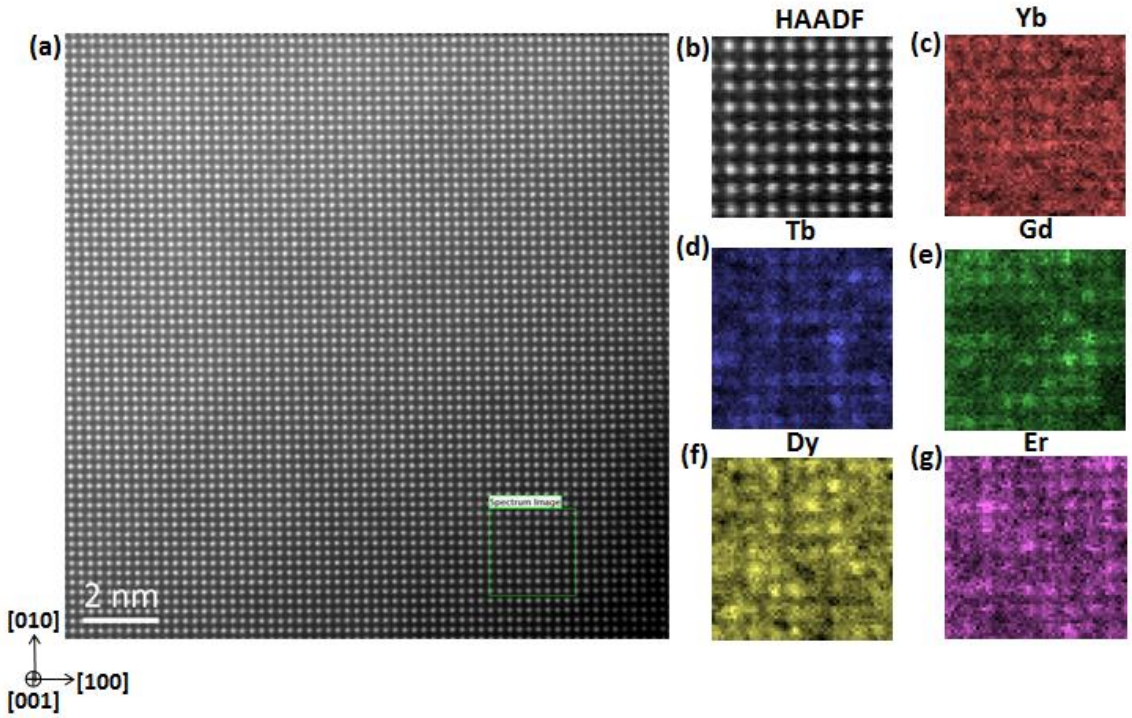

Figure 4.8: HAADF-STEM imaging and atomic scale electron-energy loss spectroscopy (EELS) mapping along [001] for the single-crystalline $(5RE_{0.2})_2Ti_2O_7$. (a) Atomic-resolution HAADF image, where the green region was used for EELS mapping analysis in (b)-(g). (b) HAADF image recorded simultaneously during the EELS data set acquisition; (c) Yb, (d) Tb, (e) Gd, (f) Dy, and (g) Er chemical maps obtained from their M_5-signals, respectively.

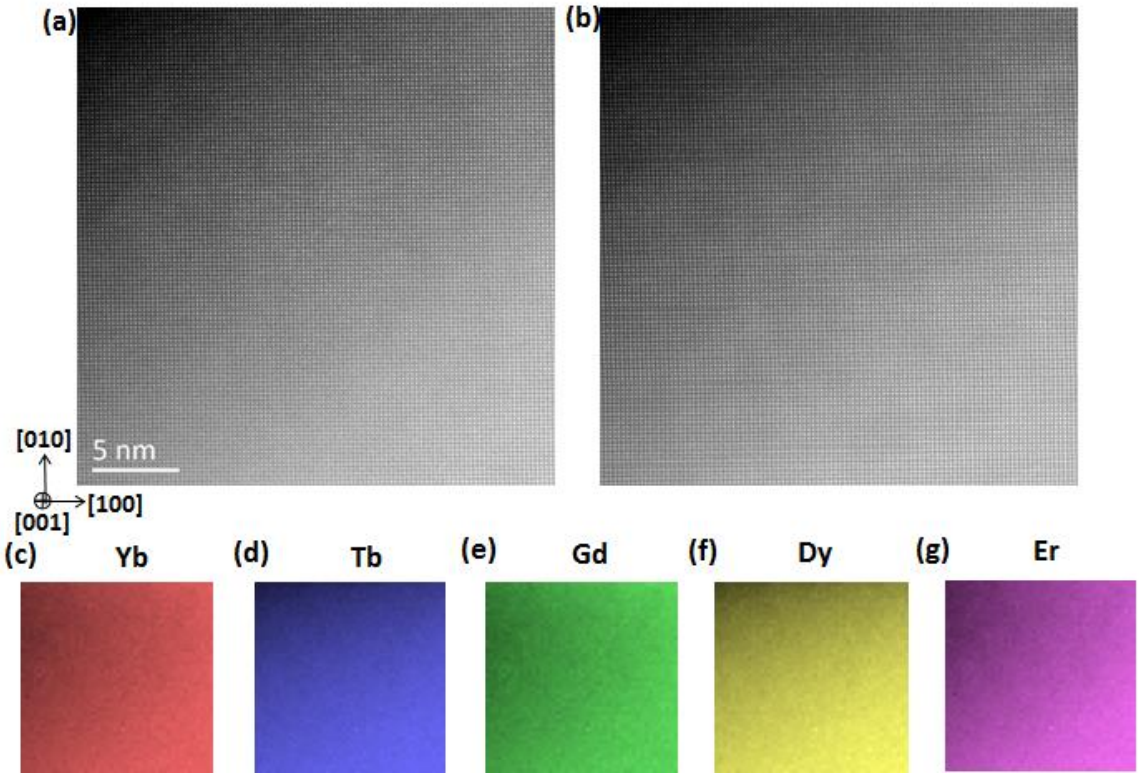

Figure 4.9: HAADF-STEM imaging and nano-scale electron-energy loss spectroscopy (EELS) mapping along [001] for the polycrystalline $(5RE_{0.2})_2Ti_2O_7$. (a) Atomic-resolution HAADF image for the EELS mapping region with the dimension of 27 nm × 27 nm. (b)-(g) EELS mapping analysis: (b) HAADF image recorded simultaneously during the EELS data set acquisition; (c) Yb, (d) Tb, (e) Gd, (f) Dy, and (g) Er chemical maps obtained from their M_5-signals, respectively. Note that each pixel in EELS maps is scanned by 16 × 16 for the simultaneously recorded HAADF image in (b), resulting in atomic-resolution in (b) while nano-scale resolution in the EELS maps in (c)-(g).

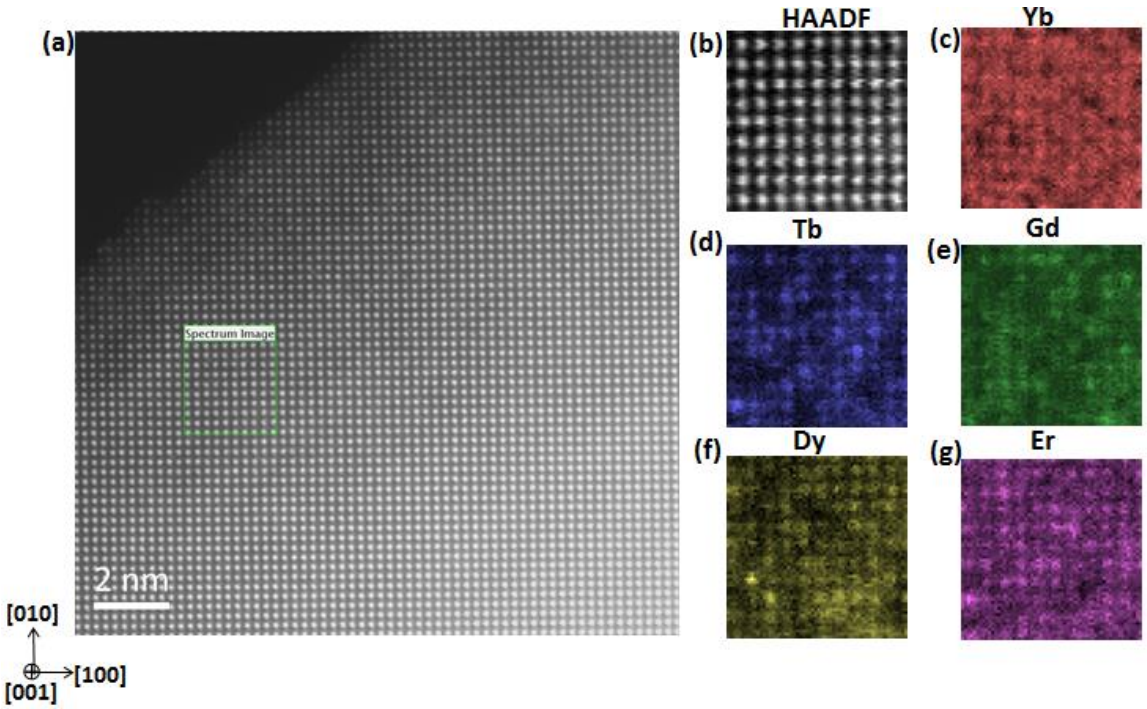

Figure 4.10: HAADF-STEM imaging and atomic-scale electron-energy loss spectroscopy (EELS) mapping along [001] for the polycrystalline $(5RE_{0.2})_2Ti_2O_7$. (a) Atomic-resolution HAADF image, where the green region was used for EELS mapping analysis in (b)-(g). (b) HAADF image recorded simultaneously during the EELS data set acquisition; (c) Yb, (d) Tb, (e) Gd, (f) Dy, and (g) Er chemical maps obtained from their M_5-signals, respectively.

Figure 4.11 shows a comparison of the DC magnetic susceptibility measurements for polycrystalline and single crystalline $(5RE_{0.2})_2Ti_2O_7$. Both samples (Figures 4.11(a) and (b)) show paramagnetic behavior from 3 K to 300 K. Curie-Weiss temperatures and effective magnetic moments were determined for each sample using the Curie-Weiss fits of the inverse susceptibility and are also listed in Table 4.3. The Curie-Weiss law

$$\chi = \frac{C}{T - \theta_{CW}} \tag{4.1}$$

was used for these Curie-Weiss fits where χ is the magnetic susceptibility, C is the Curie constant, T is the absolute temperature, and θ_{CW} is the Curie-Weiss temperature [111]. Using linear fits between 50 K and 300 K, the Curie-Weiss temperature for the single crystal is θ_{CW} = -13.06(6) K and for the polycrystal θ_{CW} = -2.91(6) K. These temperatures are both comparable to the Curie-Weiss temperatures found for the rare-earth titanate pyrochlores [111-119] and found in Table 4.4.

The single crystal's θ_{CW} is close to that of $Gd_2Ti_2O_7$ and $Er_2Ti_2O_7$, while the polycrystal's θ_{CW} falls in between those of $Gd_2Ti_2O_7$ and $Dy_2Ti_2O_7$. Since the Curie-Weiss temperatures for both samples are negative, antiferromagnetic frustration in the lattice and antiferromagnetic exchange coupling are expected. The discrepancy between the θ_{CW} temperatures of the single crystal and polycrystal is much reduced when using the Curie-Weiss fits between 3 K to 20 K, with θ_{CW} = -2.98(0) K for the single crystal and θ_{CW} = -3.14(1) K for the polycrystal. For the single crystal, there are some minor changes in slope between the higher and lower temperature fit ranges. This could be an indication of crystal electric field effects causing fluctuation of the magnetic interactions at the different temperature ranges.

Table 4.3: Calculated effective magnetic moments, applied field direction, temperature ranges, and Curie-Weiss temperatures for $(5RE_{0.2})_2Ti_2O_7$.

*Estimated standard deviations are 1σ

Sample	Field Direction	Temperature Range (K)	Effective Magnetic Moment (μ_B)	Curie-Weiss Temperature (K)
Single Crystal	along [100]	3 - 20	5.79	-2.98(0)
		50 - 300	6.50	-13.06(6)
Polycrystal	-	3 - 20	5.46	-3.14(1)
		50 - 300	5.87	-2.91(6)

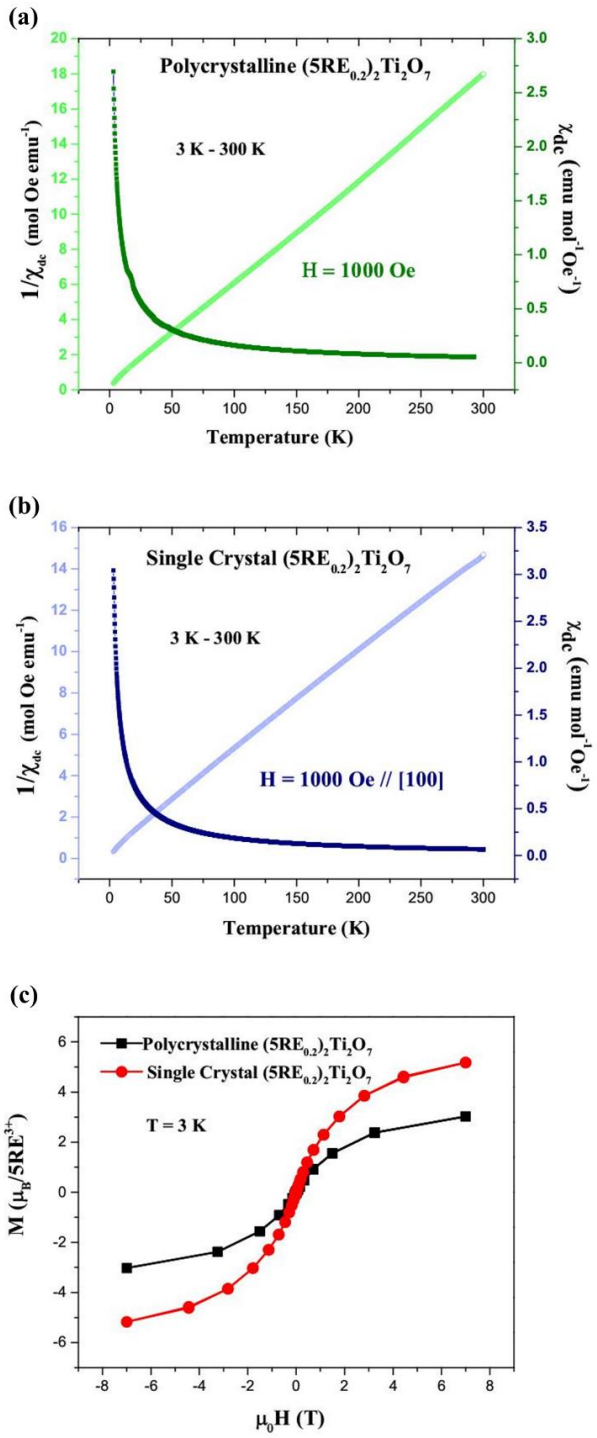

Figure 4.11: DC susceptibility measurements on $(5RE_{0.2})_2Ti_2O_7$ polycrystal (a) and single crystal with applied magnetic field along the [100] direction (b) from 3 K to 300 K, along with the magnetization curves (c) at 3 K from -7 T to 7 T.

Table 4.4: Compilation of literature reported effective magnetic moments for the single component rare-earth pyrochlore oxides, temperature ranges measured, free ion magnetic moments, and Curie-Weiss temperatures.

"-" indicates no reported value.

Rare-Earth Ion	Sample	Temperature Range (K)	$RE_2^{3+}Ti_2O_7$ Magnetic Moment (μ_B)	Free Ion Magnetic Moment (μ_B) Ref. [111]	Curie-Weiss Temperature (K)	Reference
Yb^{3+}	Polycrystal	5 - 11	3.33	4.54	0.59	[112]
	Polycrystal	-	1.15		0.75	[113]
Tb^{3+}	Polycrystal	-	9.40	9.72	-19	[114]
	Polycrystal	200 - 300	9.60		-18.9	[115]
Gd^{3+}	Polycrystal	50 - 300	7.22	7.94	-8.95	[112]
	Polycrystal	10 - 300	7.70		-9.60	[116]
	Polycrystal	-	7.80		-11.70	[118]
Er^{3+}	Polycrystal	50 - 300	8.93	9.58	-15.93	[112]
	Polycrystal	20 - 50	9.34		-22.3	
	Single Crystal	-	3.01		-	[119]
Dy^{3+}	Polycrystal	10 - 20	9.59	10.65	-0.20	[112]
	Polycrystal	-	9.96		-0.65	[118]
	Single Crystal	near 70	10.03		-0.8	[117]
		near 300	10.51		-	

The effective magnetic moment from 50 K to 300 K for the single crystal is μ_{eff} = 6.50 μ_B, making it slightly higher than the polycrystal's effective moment (μ_{eff} = 5.87 μ_B). From 3 K to 20 K, the effective magnetic moments for the polycrystal (μ_{eff} = 5.46 μ_B) and single crystal (μ_{eff} = 5.79 μ_B) are more agreeable, and remain consistent with the higher temperature calculated values. These values are smaller than the calculated average (roughly μ_{eff} = 8.48 μ_B) from the free ion magnetic moments of each of the five rare-earth cations having an oxidation state of 3+ listed in Table 4.4. It is probable that competing magnetic interactions between the five different rare-earth cations on the A-site, chemical pressure, or possible lattice distortions could contribute to the overall smaller effective magnetic moments. The effective magnetic moments of the single component rare-earth titanate pyrochlores found from literature [112-119] also show signs of variation compared to their expected free-ion magnetic moments. Due to single ion magnetic anisotropy in $Er_2Ti_2O_7$ and $Dy_2Ti_2O_7$, the values reported for these compounds vary depending on field and direction [112,117,119]. Several studies have found smaller values for the effective magnetic moments in comparison to their free-ion moments [112-113,117-119], including a study that reported the effective magnetic moment of $Yb_2Ti_2O_7$ showing temperature dependence [112]. It is therefore difficult to fully determine an average of the single component rare-earth pyrochlore oxides that agrees perfectly with the effective magnetic moments found for both the HEO polycrystal and single crystal.

The magnetization curves for the polycrystal and single crystal samples obtained at 3 K are displayed in Figure 4.11(c). Neither crystal nor polycrystal reaches complete magnetic saturation up to 7 T, and higher magnetic fields are needed to determine the saturation magnetization. The $(5RE_{0.2})_2Ti_2O_7$ single crystal shows a higher magnetization overall in comparison to the polycrystal.

AC susceptibility measurements on the single crystal sample between 0.3 K and 1.7 K are displayed in Figure 4.12. A noticeable broad peak near 0.94 K in Figure 4.12(a) begins to decrease and shift toward lower temperatures as the field is increased from 0 T to 1 T, indicating that the system's interactions are antiferromagnetic. Figure 4.12(b) shows a peak that is characteristic of the spin freezing temperature at approximately T_f = 0.84 K and moves from

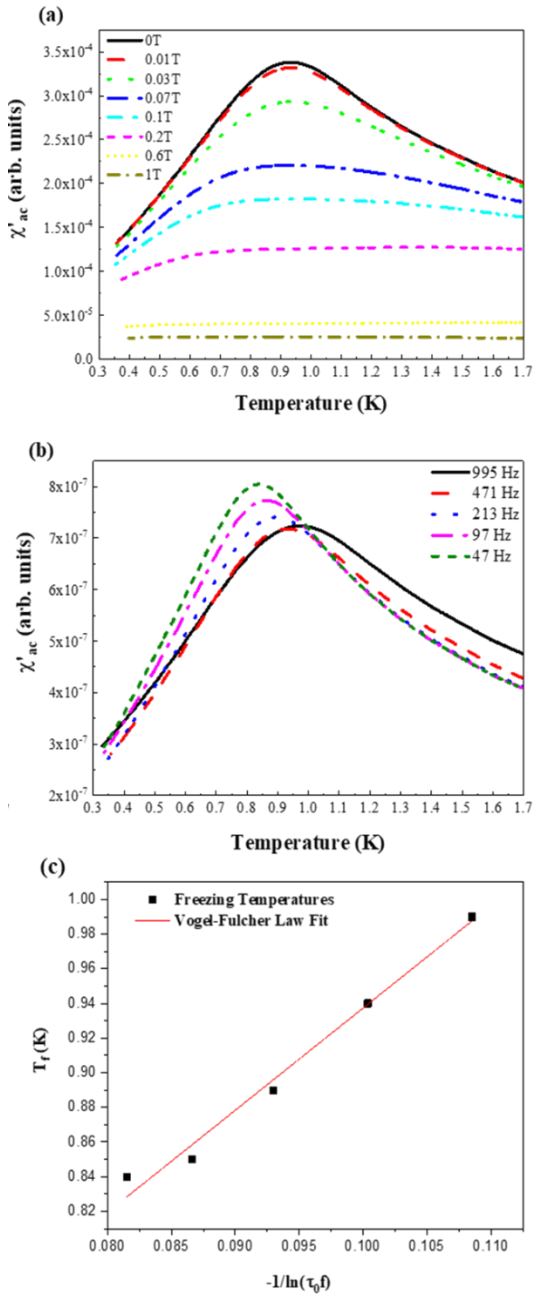

Figure 4.12: AC susceptibility measurements (the real part) on single crystal $(5RE_{0.2})_2Ti_2O_7$ from temperatures of 0.3 K to 1.7 K with (a) magnetic fields ranging from 0 T to 1 T and (b) dependence on frequency ranging from 47 Hz to 995 Hz, indicating a spin-glass magnetic ground state. (c) Linear relation of frequency dependence to freezing temperature (Vogel-Fulcher law).

0.84 K to 0.98 K as the frequency increases from 47 Hz to 995 Hz. This frequency dependence may signal a possible spin-glass ground state.

In order to have a spin-glass material, site disorder and frustration must be present [93]. As mentioned previously, disorder exists in this material due to the presence and randomization of the five rare-earth cations on the A-site. The frustration index

$$f = -\frac{\theta_{CW}}{T_f} \tag{4.2}$$

is often used to measure the level of frustration in a system and indicates frustration if $f > 1$ [93]. In $(5RE_{0.2})_2Ti_2O_7$, we find a frustration value of ~15.5 using the single crystal values θ_{CW} = -13.06(6) K and T_f = 0.84 K. This value represents a material having strong geometric frustration ($f > 10$), providing evidence for a spin-glass [93,120]. If the single crystal value θ_{CW} = -2.98(0) K found from the Curie-Weiss fit between 3 K to 20 K is used, we get a frustration value of ~ 3.5 which is still a clear indicator of system frustration. Figure 4.12(c) is a relation of the frequency dependence with the freezing temperature using the Vogel-Fulcher law represented by

$$T_f = T_0 - \frac{E_a}{k_B}\frac{1}{\ln(\tau_0 f)} \tag{4.3}$$

where E_a is the activation energy, τ_0 is the intrinsic relaxation time, f is the frequency, and T_0 is ideal glass temperature for the system [120,121]. A τ_0 value between 1×10^{-13} s (conventional spin-glasses) and 1×10^{-7} s (cluster glasses) represents the typical range of possible intrinsic relaxation times for spin-glasses [93,120-121]. For this reason, 1×10^{-7} s is used for τ_0 in this fit and gave reasonable values of E_a = 0.5 meV and T_0 = 0.37 K. The fit shows reasonable linearity of the freezing temperatures using the Vogel-Fulcher law, providing extended evidence of glassy behavior. Although there is significant evidence for a spin-glass ground state, further

measurements such as specific heat and inelastic neutron scattering are still needed to verify this behavior, understand the local magnetic structure, and confirm the ground state transition.

4.4 Summary

We report the synthesis, structure, and magnetic characterization of a new high entropy, configurationally complex oxide $(Yb_{0.2}Tb_{0.2}Gd_{0.2}Dy_{0.2}Er_{0.2})_2Ti_2O_7$, also referred to as $(5RE_{0.2})_2Ti_2O_7$. We have shown that this material can be synthesized in the cubic pyrochlore phase (227) and single crystals of good quality can be grown using the floating zone growth technique. STEM-EELS results further support single-phase polycrystalline and single crystalline materials and confirm cation homogeneity down to ~2.3 nm. Susceptibility and magnetization studies on this oxide indicate antiferromagnetic exchange coupling, and the effective magnetic moments and Curie-Weiss temperatures were determined and reported. Low temperature AC susceptibility measurements suggest a spin-glass magnetic ground state.

CHAPTER FIVE

EFFECTS OF ION-IRRADIATION INDUCED DAMAGE IN HIGH-ENTROPY PYROCHLORE OXIDE SINGLE CRYSTALS

A version of this chapter was submitted to Scripta Materialia and authored by C. Kinsler-Fedon, L. Nuckols, C. Nelson, Z. Qi, Q. Huang, D. Mandrus, Y. Zhang, W.J. Weber, and V. Keppens, Effects of Au^{2+} irradiation induced damage in a high-entropy pyrochlore oxide single crystal, Scripta Materialia, (2022). [122]

In this chapter, we report an ion-irradiation study of a compositionally complex (high entropy) pyrochlore oxide. The damage produced from 4 MeV Au^{2+} ion irradiation on single crystal $(Yb_{0.2}Tm_{0.2}Lu_{0.2}Ho_{0.2}Er_{0.2})_2Ti_2O_7$ aligned along the [100] direction is investigated at room temperature by Rutherford backscattering spectrometry in channeling mode (RBS/C). Damage profiles based on RBS/C are presented and compared to single-component pyrochlore titanate oxides to evaluate the relative resistance to irradiation-induced amorphization. Additional results from a separate preliminary irradiation study will be discussed near the end of this chapter on HEO composition $(Yb_{0.2}Tb_{0.2}Gd_{0.2}Dy_{0.2}Er_{0.2})_2Ti_2O_7$. .

5.1 Introduction

When considering materials for nuclear waste management, the $RE_2^{3+}Ti_2^{4+}O_7$ pyrochlore materials have been studied extensively by the incorporation of actinides [20,123-125]. It is understood that rare-earth titanate pyrochlores respond to ion irradiation by transforming into an amorphous state once it reaches a specific local damage dose under a given irradiation condition. The specific dose for the amorphous transition is highly dependent upon the incident ion mass and energy, as well as the size of the rare-earth cation (the larger the rare-earth cation, the greater the resistance to amorphization). Until now, no studies have been reported on the effects of irradiation induced damage on a high entropy titanate pyrochlore single crystal to understand its amorphization behavior. Extending the study of ternary rare-earth pyrochlore oxides and their

radiation response to the area of HEOs and multicomponent materials is necessary to improve or expand our options for storing nuclear waste and radioactive materials. At the same time, controlled response to ion irradiation offers potential for tuning properties and creating new functionalities in these compounds. Because multicomponent materials typically possess heavily distorted lattices and improved chemical durability, these materials can be highly attractive for radiation applications [126]. Within the past few years, radiation damage related research has gained momentum for configurationally complex materials, such as high entropy alloys (HEAs) [126-129], high entropy carbides [130], and even more recently high entropy oxides have been proposed as nuclear waste forms [90-91]. Some novel findings from these recent reports include improved radiation resistance, enhanced mechanical properties at elevated temperatures, excellent structural stabilities, high corrosion resistance, and reduced irradiation hardening. The tunability of the chemical and mechanical properties by manipulating the number of cations, the entropy site disorder, and mixing possibilities can enhance the properties and lead to a wider range of possible applications.

Because irradiation damage in single component pyrochlore oxides has been studied in detail [19,23,50,131], an examination of irradiation damage effects in a high entropy pyrochlore oxide is a logical extension. Large, high-quality single crystals of $(Yb_{0.2}Tm_{0.2}Lu_{0.2}Ho_{0.2}Er_{0.2})_2Ti_2O_7$ can be grown via the floating zone technique, making it an ideal candidate for analysis by Rutherford backscattering spectrometry in channeling mode (RBS/C). The damage profiles from 4 MeV Au ions are reported for $(Yb_{0.2}Tm_{0.2}Lu_{0.2}Ho_{0.2}Er_{0.2})_2Ti_2O_7$, and the results are compared to selected standard rare-earth pyrochlore oxides. In addition, preliminary ion-irradiation experimentation on $(Yb_{0.2}Tb_{0.2}Gd_{0.2}Dy_{0.2}Er_{0.2})_2Ti_2O_7$ will be briefly discussed, along with Raman spectroscopy characterization following irradiations from 23 MeV Ni ions.

5.2 Experimental Procedure

Generalized descriptions of the experimental methods and instrumentation used are provided in Chapter 3. This section is provided to explain the specifics of the experimental regime for the

Au-ion irradiation study of the $(Yb_{0.2}Tm_{0.2}Lu_{0.2}Ho_{0.2}Er_{0.2})_2Ti_2O_7$ single crystal. Chapter 4 discusses the synthesis and preparation for the $(Yb_{0.2}Tb_{0.2}Gd_{0.2}Dy_{0.2}Er_{0.2})_2Ti_2O_7$. As described in Chapter 3, solid state reactions were used to synthesize $(Yb_{0.2}Tm_{0.2}Lu_{0.2}Ho_{0.2}Er_{0.2})_2Ti_2O_7$. Single crystal $(Yb_{0.2}Tm_{0.2}Lu_{0.2}Ho_{0.2}Er_{0.2})_2Ti_2O_7$ was grown using the floating-zone growth technique and a two-mirror optical floating-zone furnace (Canon Machinery model SC1- MDH) with 1500-W halogen lamps. This crystal growth procedure is similar to $(Yb_{0.2}Tb_{0.2}Gd_{0.2}Dy_{0.2}Er_{0.2})_2Ti_2O_7$ described in Chapter 4.2, using an oxygen atmosphere at a pressure of 0.2 MPa and a growth rate of 5-6 mm per hour. The rods were counter-rotated at 20–25 rpm. Laue diffraction, using a Huber X-ray diffractometer and HD-CR 35 NDT (digital image plate scanner), was employed to determine crystal quality and align the crystal along the [100] direction for ion beam bombardment. An oval-shaped piece, roughly 9 mm in length and 1 mm in thickness, was cut from the oriented rod and polished to a mirror finish. Scanning electron microscopy using a Zeiss EVO scanning electron microscope with Bruker xFlash 6130 energy-dispersive X-ray spectrometer (EDXS) were used to analyze the single crystal surface prior to irradiation to confirm cation homogeneity (color mapping) and compositional stoichiometry. These results are summarized in Appendix C.

Room temperature Au-ion irradiations and ion beam analysis via Rutherford backscattering spectrometry (RBS/C) were performed using the 3 MeV tandem accelerator and associated facilities at the Ion Beam Materials Laboratory (IBML) at the University of Tennessee, Knoxville [100]. 4 MeV Au^{2+} ions were chosen as the irradiating species to ensure damage is shallow enough to be measured using RBS/C analysis. It also allows for comparison of the disordering behavior to that of other RE pyrochlores [98-99,131]. Irradiations were performed 4° off the normal surface to limit undesired channeling effects in the single crystal. Ion fluences ranged from 5×10^{12} to 6×10^{13} cm^{-2} to induce a wide range of damage states in the target material. A flux of 4.2×10^{11} $cm^{-2}s^{-1}$ was constant for all the irradiations. The irradiating beam was slightly wobbled and defocused so that the resulting damage was uniform. In-situ damage accumulation along the [100] direction was determined using RBS/C under high (< 2.0×10^{-7} torr) vacuum using a 3.5 MeV He^{+} ion beam to obtain quantitative RBS/C spectra to a depth of ~850 nm. Disorder profiles were determined from the RBS/C spectra using the iterative procedure described elsewhere [132]. The Stopping and Range in Matter code (SRIM code)

[133], in full-cascade mode [134], was used to determine the depth profiles of atomic displacements for the 4 MeV Au ions. The threshold displacement energies for all the ions in the target material were set to 50 eV [101] and an experimentally derived density of 7 g/cm^3 was used in the SRIM simulations. The irradiated crystal was prepared for Transmission Electron Microscopy (TEM) analysis by first coating the surface with a thin layer of carbon and milling two (~3 microns in depth from the irradiated surface) specimens from the two irradiated areas of the crystal. The milling was achieved by FIB-SEM (focused ion beam scanning electron microscopy) using a high-resolution Zeiss Auriga scanning electron microscope with the probe operating at 5 kV and 20 pA and an accelerating voltage (EHT) of 7 kV. TEM was performed on an FEI Titan at 300kV. Diffraction contrast images were captured using the two-beam condition with the sample tilted slightly off the zone axis to isolate diffraction from the (001) normal planes.

5.3 Results and Discussion

Based on the SRIM simulations, the depth profiles of local damage dose (displacements per atom or dpa) and implanted Au concentration at the highest ion fluence in this study (6×10^{13} cm^{-2}) are shown in Figure 5.1. The predicted damage profiles for all ion fluences employed in this irradiation experiment are provided in Figure 5.2. Under these irradiation conditions, the damage peak is at a depth of ~ 400 nm, and the peak concentration of implanted Au is predicted to be at ~ 520 nm.

Two separate irradiation experiments under identical conditions were performed on the same single crystal sample, which was repolished to remove damage from the first irradiation experiment prior to the second irradiation. The disorder accumulation curves shown in Figures 5.3(a) and 5.3(b) represent the two separate experiments and show the depth profiles of damage accumulation at various ion fluences, from 0.5 to 3.6×10^{13} cm^{-2}, on the RE sublattice. To obtain these damage profiles, an iterative process [132] using the raw RBS spectra (Figure 5.4) has been performed to generate the disorder in the material versus depth. This process allows for the removal of dechanneling effects and is commonly employed for this purpose [98-99,132]. A more detailed description of this process and how it is used is found elsewhere [132].

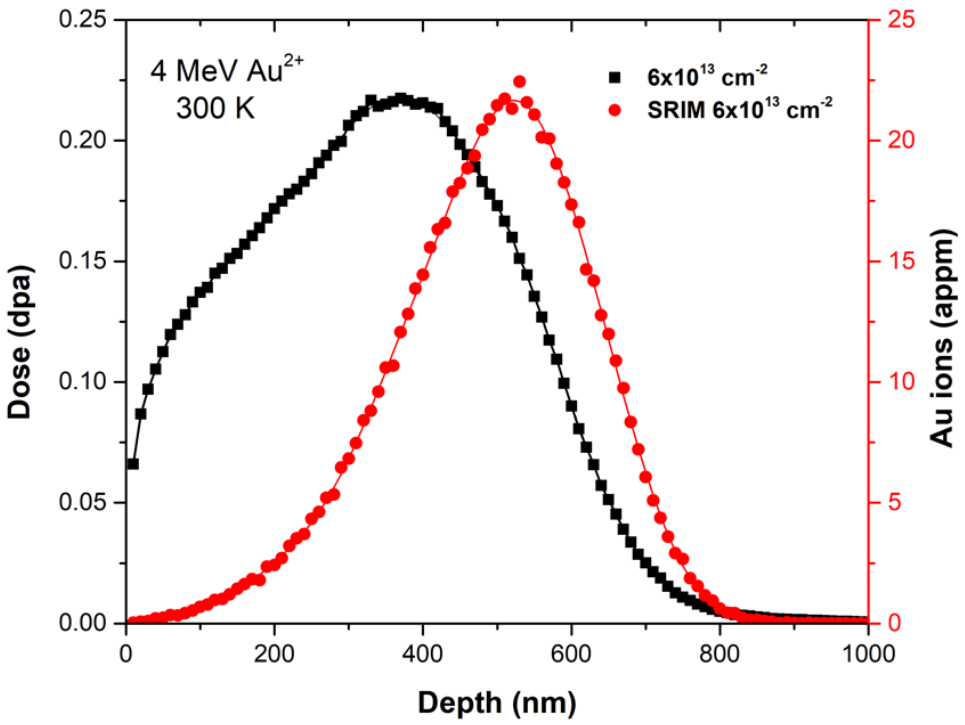

Figure 5.1: The depth profiles of local damage dose (dpa), represented by solid black squares, and implanted Au concentration (appm), represented by solid red circles predicted by SRIM simulations for an ion fluence of 6 ×10^{13} cm^{-2}. Solid red and black lines are fits to the data.

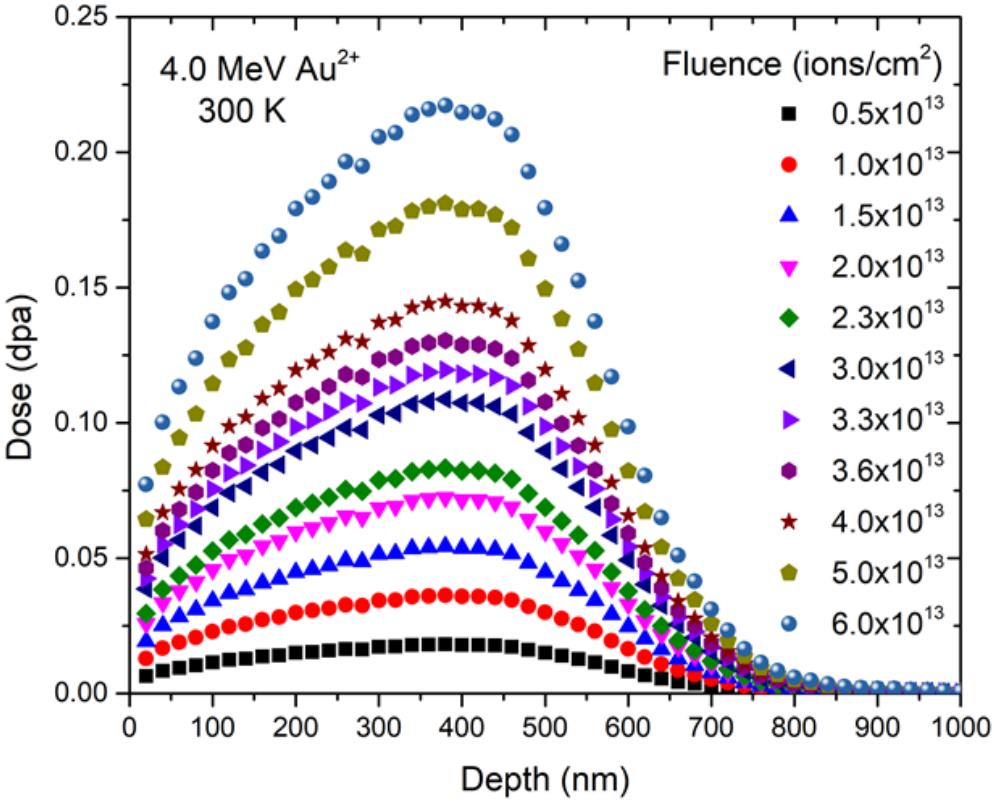

Figure 5.2: Local damage dose (dpa) as a function of depth following 4 MeV Au^{2+} irradiation to ion fluences from 0.5 to 6 ($\times 10^{13}$ cm^{-2}) of $(Yb_{0.2}Tm_{0.2}Lu_{0.2}Ho_{0.2}Er_{0.2})_2Ti_2O_7$.

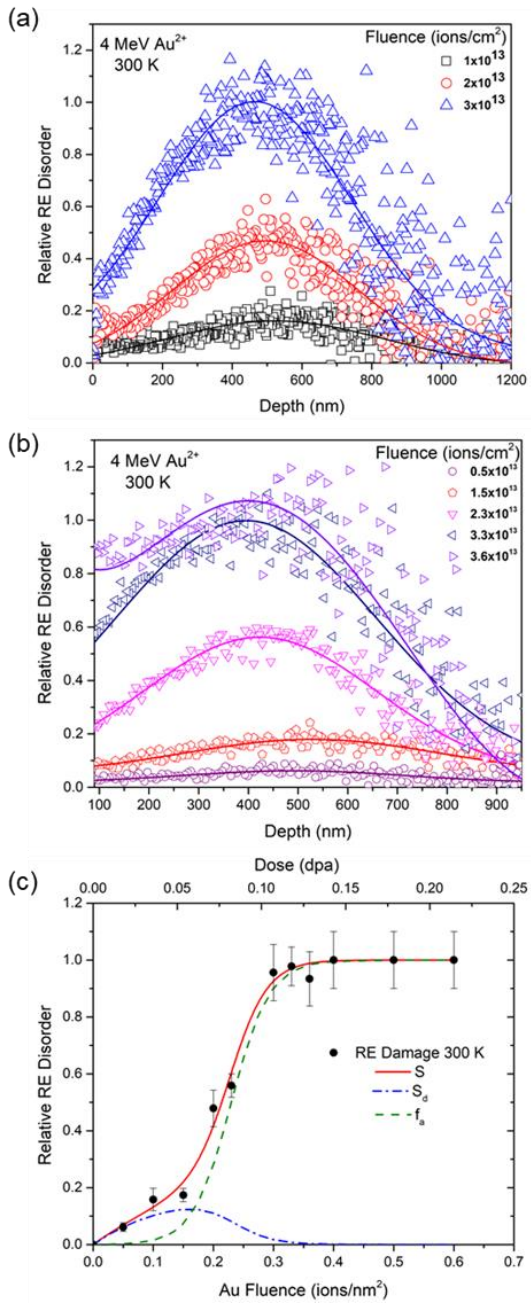

Figure 5.3: $(Yb_{0.2}Tm_{0.2}Lu_{0.2}Ho_{0.2}Er_{0.2})_2Ti_2O_7$ rare-earth sublattice disorder curves following 4 MeV Au^{2+} irradiation with ion fluences ranging from (a) 1 to 3 ($\times 10^{13}$ cm^{-2}) and (b) 0.5 to 3.6 ($\times 10^{13}$ cm^{-2}). Solid lines represent fits to the data. (c) Relative rare-earth disorder at the damage peak as a function of Au fluence and dose. The solid red line is the fit of the damage accumulation along with the amorphous region f_a (green dashed line) and the residual crystalline region S_d (blue dashed/dotted line).

Using the experimentally derived density of 7 g/cm^3 for the SRIM simulations, the He ion stopping power as a function of energy was determined for the HEO pyrochlore, and the energy difference per channel was used to determine the depth. Ultimately, these depth profiles show that the disorder increases with increasing ion fluence and a slight shift of the damage peak toward the surface, resulting in a fully amorphous material at the damage peak for a fluence of about 3.66×10^{13} cm^{-2}.

The accumulation of relative rare-earth disorder at the damage peak as a function of ion fluence and local damage dose is shown in Figure 5.3(c). In order to describe this damage accumulation behavior, a disorder accumulation model is employed [98-99,131]. Eq. 5.1 represents this model, with S being the total irradiation-induced disorder, f_a is the amorphous fraction, and S_d is the defect-induced disorder in the remaining damaged crystalline regions.

$$S = f_a + S_d \qquad (5.1)$$

This model is also referred to as the DI/DS model (direct-impact, defect-stimulated) [135]. For the amorphous fraction, Eq. 5.2 describes the relationship between σ_a (direct amorphous cross section), σ_s (defect-stimulated amorphous cross section), and D is either the local dose (in dpa) or ion fluence.

$$f_a = 1-(\sigma_a+\sigma_s)/\{\sigma_s+\sigma_a \exp(\sigma_a+\sigma_s)D\} \qquad (5.2)$$

To account for the damage caused by defects in the crystalline structure, Eq. 5.3 quantitatively represents this damage given the saturation value S_d* and a constant B that corresponds to the cross section relating to the probability of defect recombination processes [131].

$$S_d = S_d^*[1-\exp(-BD)](1-f_a) \qquad (5.3)$$

Figure 5.3(c) summarizes the collective results from this damage accumulation model, showing the contributions from f_a and S_d and a fit to the mixed RE disorder at the damage peak at ambient

temperature. The relative RE disorder as a function of Au fluence (ions/nm^2) and dose (dpa) reveals a nonlinear behavior with complete amorphization shown at ~ 0.13 dpa and 4 MeV Au fluences of ~ 0.37 (ions/nm^2). These results are comparable to similar studies on other rare-earth titanate pyrochlores [98-99,131], and Table 5.1 summarizes the ion fluence and dose experimentally found for attaining complete amorphization at the damage peak in each composition. The HEO pyrochlore's dose for amorphization appears to be slightly higher than $Ho_2Ti_2O_7$, indicating more radiation resistance, but lower than that for $Sm_2Ti_2O_7$, suggesting less radiation resistance. Likewise, when compared to $Gd_2Ti_2O_7$, which was irradiated under similar conditions (4 MeV Au ions), the HEO pyrochlore appears to be less radiation resistant.

It must also be noted that the Au ion energies are lower for $Sm_2Ti_2O_7$ and $Ho_2Ti_2O_7$ (1 MeV), which may affect a direct comparison with the HEO pyrochlore (4 MeV). Under 1 MeV Kr ion irradiation, the critical dose for amorphization of simple rare-earth titanate pyrochlores at room temperature varies by up to a factor of three depending on the specific rare-earth element on the A-site [22]; however, the critical dose under 0.6 MeV Bi ion irradiation is 0.18 ± 0.01 dpa for $A_2Ti_2O_7$ (A = Y, Sm, Gd, Lu) pyrochlores [101], which is comparable to the results in Table 5.1. The HEO pyrochlore in this study may represent the behavior of a mixture of pyrochlores with a range of critical doses (amorphization resistance), but additional studies on relevant rare-earth pyrochlores under identical heavy-ion irradiation conditions are needed to better understand this behavior.

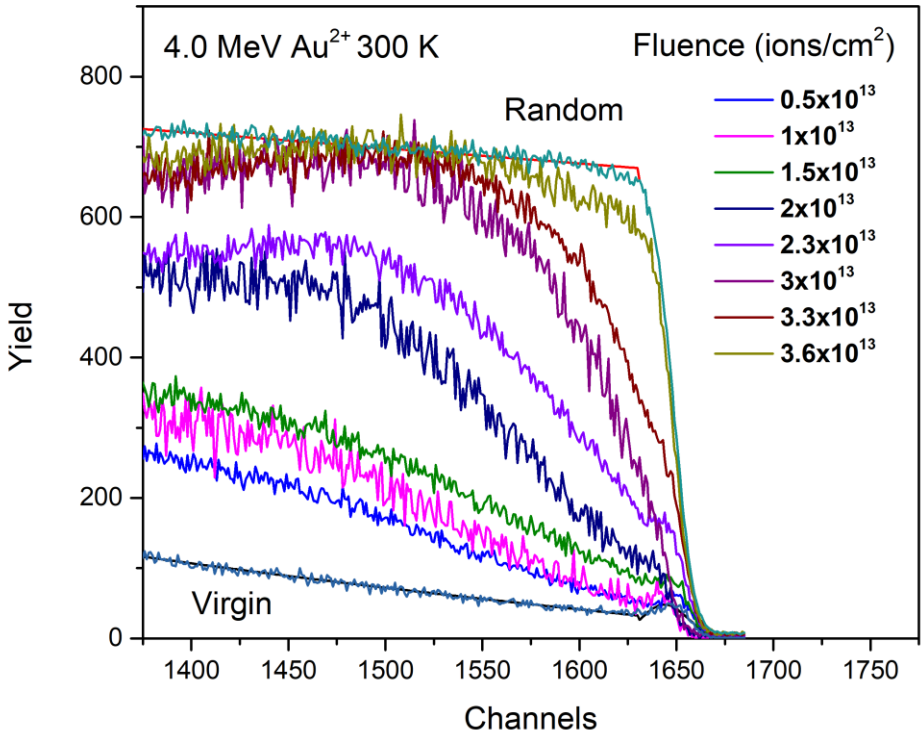

Figure 5.4: RBS channeling spectra for the HEO titanate pyrochlore $(Yb_{0.2}Tm_{0.2}Lu_{0.2}Ho_{0.2}Er_{0.2})_2Ti_2O_7$ aligned in the [100] direction.

Table 5.1: Comparison of the HEO pyrochlore irradiation conditions and fluence/dose for achieving amorphous state at damage peak with those of single-component rare-earth titanate pyrochlores.

Rare-Earth Titanate Pyrochlore Composition	Irradiation Species	Ion Fluence for Amorphization	Amorphization Dose (dpa)	Reference
$Gd_2Ti_2O_7$	4.0 MeV Au	$4.5x10^{13}$ cm^{-2}	0.15	[131]
$Sm_2Ti_2O_7$	1.0 MeV Au	$4.0x10^{13}$ cm^{-2}	0.14	[99]
$Ho_2Ti_2O_7$	1.0 MeV Au	$2.7x10^{13}$ cm^{-2}	0.12	[98]
$(Yb_{0.2}Tm_{0.2}Lu_{0.2}Ho_{0.2}Er_{0.2})_2Ti_2O_7$	4.0 MeV Au	$3.6x10^{13}$ cm^{-2}	0.13	

The amorphization parameters derived from the model fit discussed above are listed in Table 5.2, along with those experimentally found for $Gd_2Ti_2O_7$ from a previous study [131]. Because σ_s is significantly larger than σ_a, amorphization induced by accumulating defects is the most probable cause for overall amorphization in this HEO. At low doses up to ~0.065 dpa, the disorder caused by defects, S_d, has a greater influence on the HEO. At doses greater than ~0.07 dpa, the impact of the amorphous fraction, f_a, becomes dominant. These phenomena are common observations similar to previous reports for the typical, single-component titanate pyrochlores; however, this effect occurs at a higher dose in the HEO compared to the Ho and Sm pyrochlores (~0.03 dpa) [98-99]. The accumulation of disorder at the damage peak for the HEO titanate pyrochlore and $Gd_2Ti_2O_7$ are compared in Figure 5.5 for similar 4 MeV Au ion irradiations at room temperature. There are notable differences in disordering behavior between the two pyrochlores, as illustrated in Table 5.2 and Figure 5.5. At lower doses, the behavior of the different pyrochlores is relatively similar, but at a dose of ~0.09 dpa, a clear divergence in the total irradiation-induced disorder is shown. This divergence shows that $Gd_2Ti_2O_7$ has a slower rate of defect-stimulated amorphization in comparison to that of the HEO pyrochlore, which is also reflected by the higher defect-stimulated cross section σ_s for the HEO found in Table 5.2. The HEO pyrochlore does have a smaller direct amorphization cross section σa meaning that it is slightly less susceptible to direct amorphous behavior upon impact of heavy ions. From these results, it can be concluded that overall $Gd_2Ti_2O_7$ has higher radiation resistance than the HEO at room temperature.

Table 5.2: Comparison of the HEO's amorphization model parameters to $Gd_2Ti_2O_7$ [131]. These parameters were determined from data fits shown in Figures 5.3(c) and 5.5.

Amorphization Parameters	HEO RE sublattice	Gd sublattice
σ_a	0.022 nm^2	0.50 ± 0.25 nm^2
σ_s	31.65 nm^2	13 ± 2 nm^2
S_d^*	0.3 nm^2	0.15 ± 0.4 nm^2
B	5 nm^2	2.8 ± 4 nm^2

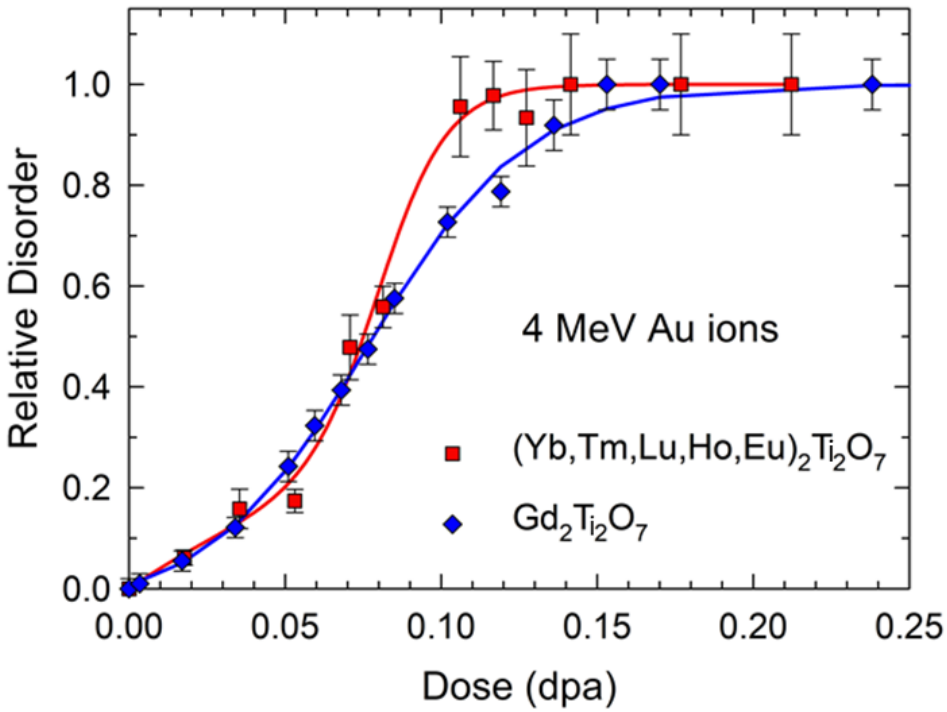

Figure 5.5: Comparison of rare-earth disorder at the damage peak as a function of dose between reported $Gd_2Ti_2O_7$ [131] and HEO $(Yb_{0.2}Tm_{0.2}Lu_{0.2}Ho_{0.2}Er_{0.2})_2Ti_2O_7$ single crystals with 4.0 MeV Au ions at 300 K. The red and blue solid lines are fits to the damage data points.

Cross-sectional TEM was conducted to characterize the resulting radiation damage of the HEO pyrochlore single crystal. Figures 5.6(a) and (b) are dark field micrographs showing the layers of damage at ion fluences of 3.33 and 3.66 ($\times 10^{13}$ cm^{-2}), respectively. The damaged region extends from the surface to ~ 800 nm in depth, with a peak in damage at a depth of 450 to 550 nm, which is consistent with the RBS/C results. Beyond this depth, a virgin region of crystal exists that was unaffected by the ion beam. It is suspected that cation disordering and defects are the primary factors leading to amorphization in this HEO crystal composition when exposed to 4 MeV Au irradiation, as predicted by the DI/DS model previously discussed. The local atomic displacements on the A lattice sites due to the random distribution of rare-earth cations may contribute to an increased instability and susceptibility to amorphization. The dark-light mottled contrast in the damaged layer is evidence of damage appearing as strained residual crystalline regions (light contrast) and unstrained amorphous regions (dark contrast) in Figures 5.6(a) and (b). While the SAED patterns indicate the presence of amorphous material, this may be due to amorphous material in the damaged layer and/or the amorphous graphite capping material. The TEM results are consistent with the RBS/C data fits in Figure 5.3(c) and in Table 5.2 that predict defect-stimulated amorphization is the primary cause of the observed crystalline to amorphous transition.

A second HEO pyrochlore composition $(Yb_{0.2}Tb_{0.2}Gd_{0.2}Dy_{0.2}Er_{0.2})_2Ti_2O_7$ was irradiated with 23 MeV Ni ions. Following these irradiations, Raman spectroscopy was conducted, as shown in Figure 5.7. The results suggest that this composition does not become amorphous until the highest fluence of $4x10^{16}$ ions/cm^2. However, it is possible that this composition may have undergone some crystallization recovery due to the transient thermal spike induced by the high electronic energy loss of each 23 MeV Ni ion during the irradiations. In order to understand this composition's room temperature amorphization resistance, a more complete study will need to be conducted.

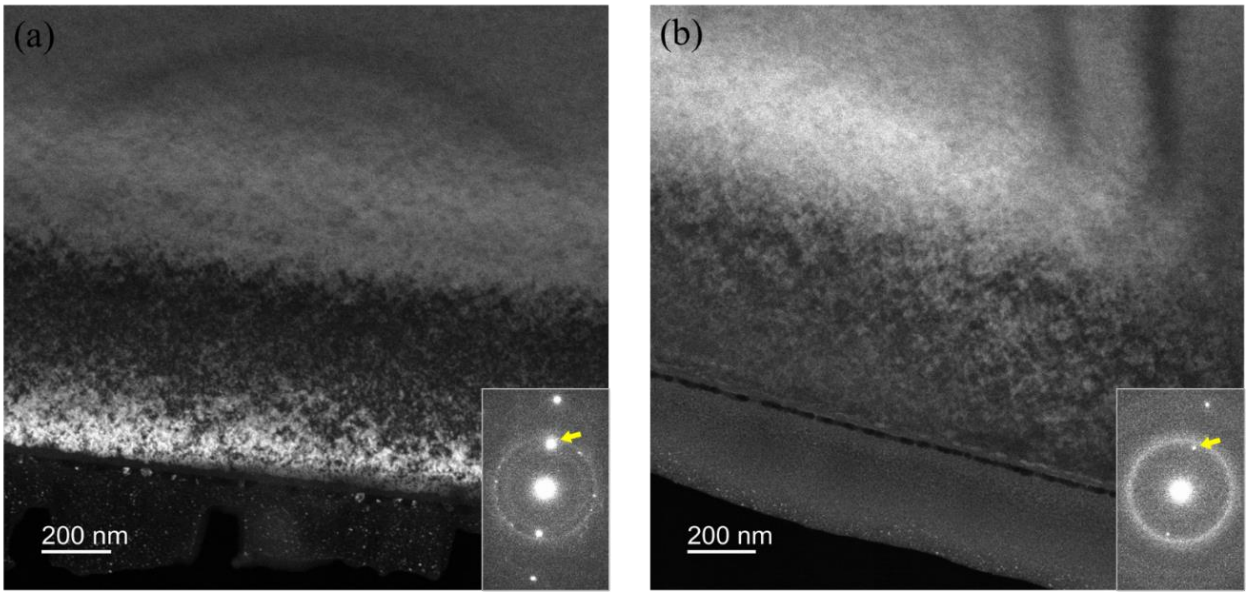

Figure 5.6: Cross-sectional TEM dark-field micrographs unveiling the damaged regions near the surface of the irradiated HEO pyrochlore crystal with 4 MeV Au^{2+} ions corresponding to the regions irradiated to ion fluences of (a) 3.33×10^{13} cm^{-2} and (b) 3.66×10^{13} cm^{-2}. Insets are SAED patterns taken on-axis, with the arrows highlighting the image forming g-vector.

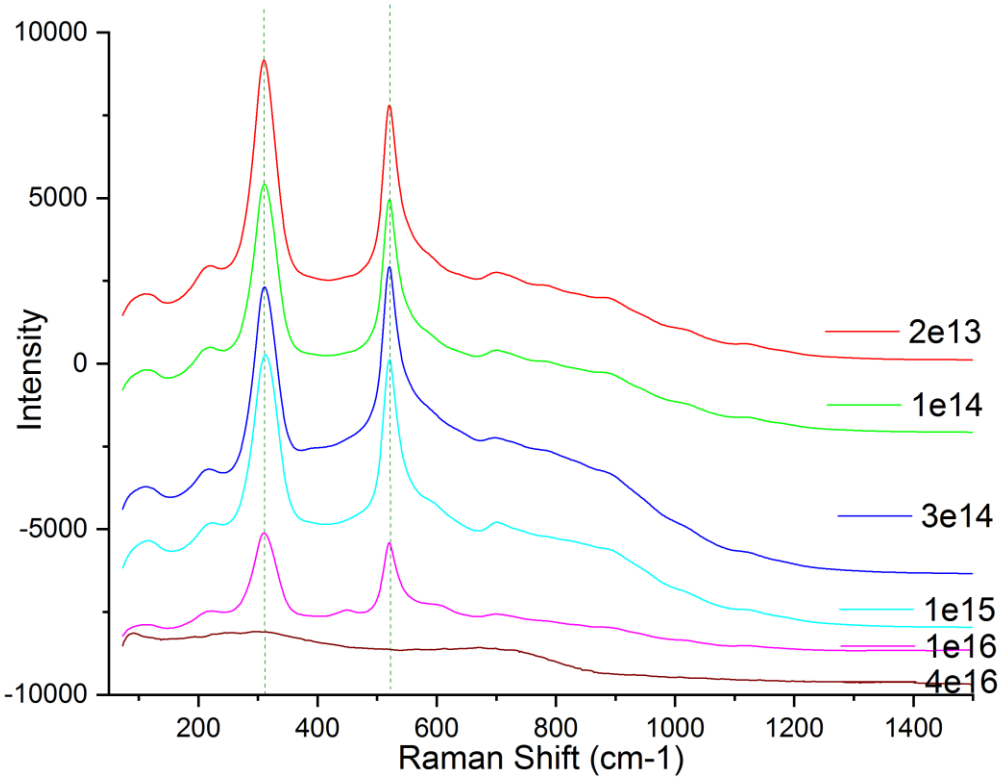

Figure 5.7: Raman spectroscopy results for HEO composition $(Yb_{0.2}Tb_{0.2}Gd_{0.2}Dy_{0.2}Er_{0.2})_2Ti_2O_7$ following 23 MeV Ni ions. Amorphization occurs at the highest ion fluence ($4x10^{16}$ ions/cm^2).

5.4 Summary

A single crystal of the novel HEO pyrochlore $(Yb_{0.2}Tm_{0.2}Lu_{0.2}Ho_{0.2}Er_{0.2})_2Ti_2O_7$ was successfully synthesized and characterized for its resistance to irradiation-induced amorphization using Rutherford Backscattering Spectrometry in channeling geometry. 4 MeV Au^{2+} irradiation was employed with ion fluences from 0.5 to 6 $\times 10^{13}$ cm^{-2} at ambient temperature. Under these conditions, an amorphous state in the HEO occurs at an ion fluence of 3.66×10^{13} cm^{-2} and a damage dose of ~0.13 dpa. From these results, it appears that the HEO may be slightly more resistant to amorphization than the single component Ho pyrochlore but less radiation resistant than the Sm and Gd pyrochlores. More studies are being conducted to gain a complete understanding of this HEO's amorphization resistance at various temperatures. A complete room temperature study is necessary to gain a definitive understanding of the $(Yb_{0.2}Tb_{0.2}Gd_{0.2}Dy_{0.2}Er_{0.2})_2Ti_2O_7$ composition's radiation resistance. It is possible that recrystallization from the high temperatures generated during the irradiation could have contributed to the appearance of high amorphization resistance. Given the promise of advanced properties in multicomponent oxides, expanding the study to include a variety of compositions and different structures with various levels of ion complexity will contribute to a better understanding of their response to irradiation damage. In addition, it is possible that irradiated configurationally complex pyrochlore oxides possess increased ionic conductivity or enhanced magnetic properties, as observed in other amorphous pyrochlores [124,136-137]. As the properties or functionalities of irradiation damaged HEOs are largely unknown, further studies are warranted.

CHAPTER SIX

NON-AMBIENT X-RAY DIFFRACTION FOR THE STUDY OF THE STRUCTURAL STABILITY OF ENTROPIC PYROCHLORE OXIDES AT ELEVATED TEMPERATURES

6.1 Introduction

Ceramic oxide compounds are notorious for having high thermal resistant properties such as low thermal conductivity, thermal shock resistance, corrosion resistance, and low thermal expansion coefficients [43-45]. These properties have been explored in a few novel high entropy oxide compositions that may be viable candidates for potential applications, including ceramic thermal barrier coatings, combustion liners, and gas diffusion pipes [35,36,71,76-79]. In this study, we explore the high temperature structural stability of five high entropy pyrochlore oxide compositions and one HEO with the TKL structure via non-ambient X-ray diffraction up to 1200 ˚C. For each single-phase composition, the phase and lattice expansion are monitored by employing sequential refinements (GSAS-II software) to determine the change in lattice parameter. The synthesis of the compounds and the details of the X-ray diffraction experiments are described in Chapter 3.

6.2 Results

This section displays the individual high-temperature X-ray diffraction results for each composition.

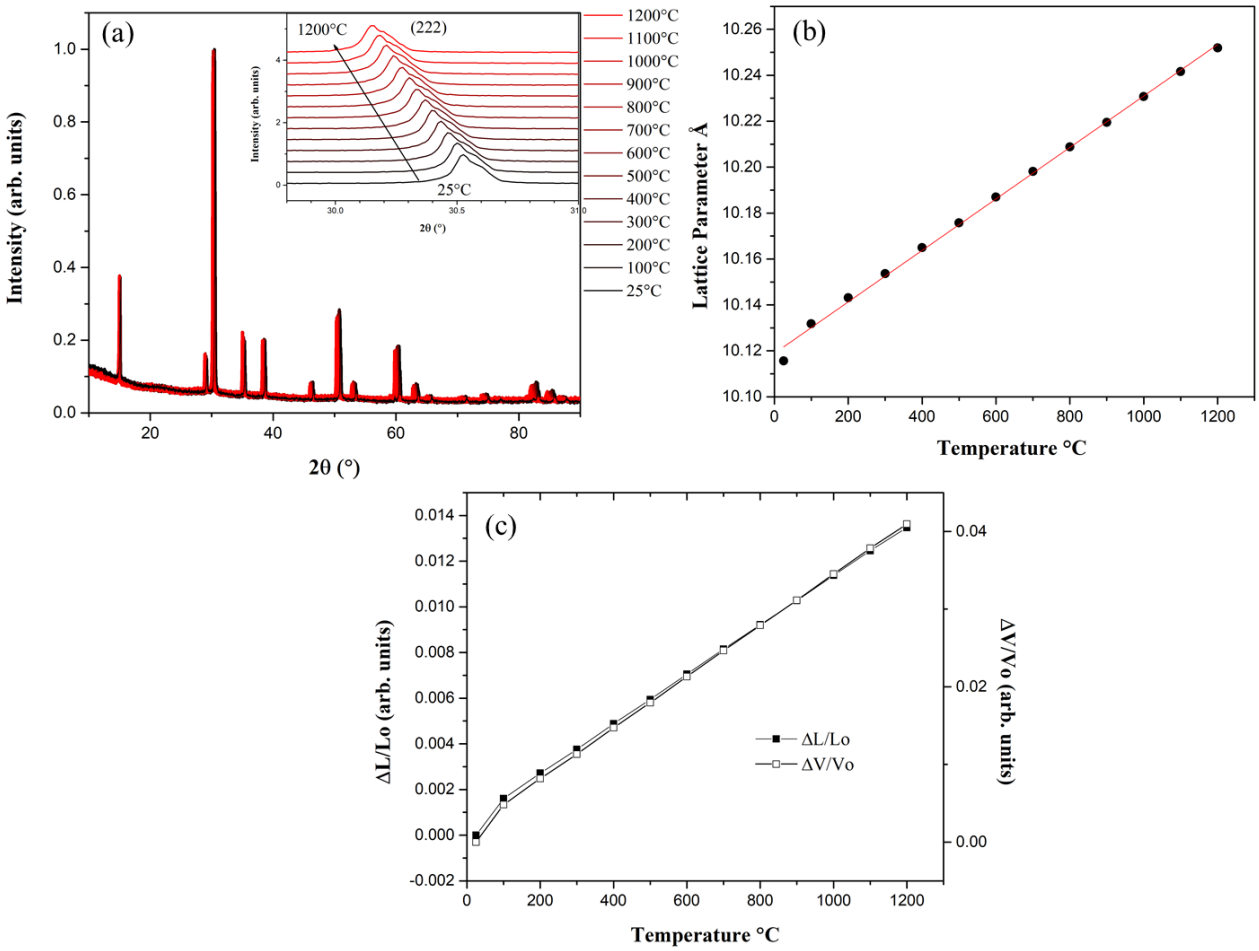

Figure 6.1: (a) Non-ambient X-ray diffraction plot for $(YbTbGdErDy)_2Ti_2O_7$ showing the pyrochlore structure expanding uniformly from 25˚C to 1200˚C. Inset is the expanded view of a diffraction peak from 29.8 to 31 ˚2θ. (b) Lattice parameter shift as a function of temperature up to 1200˚C (red line represents a linear fit to the data). (c) Length and volume trends with respect to temperature.

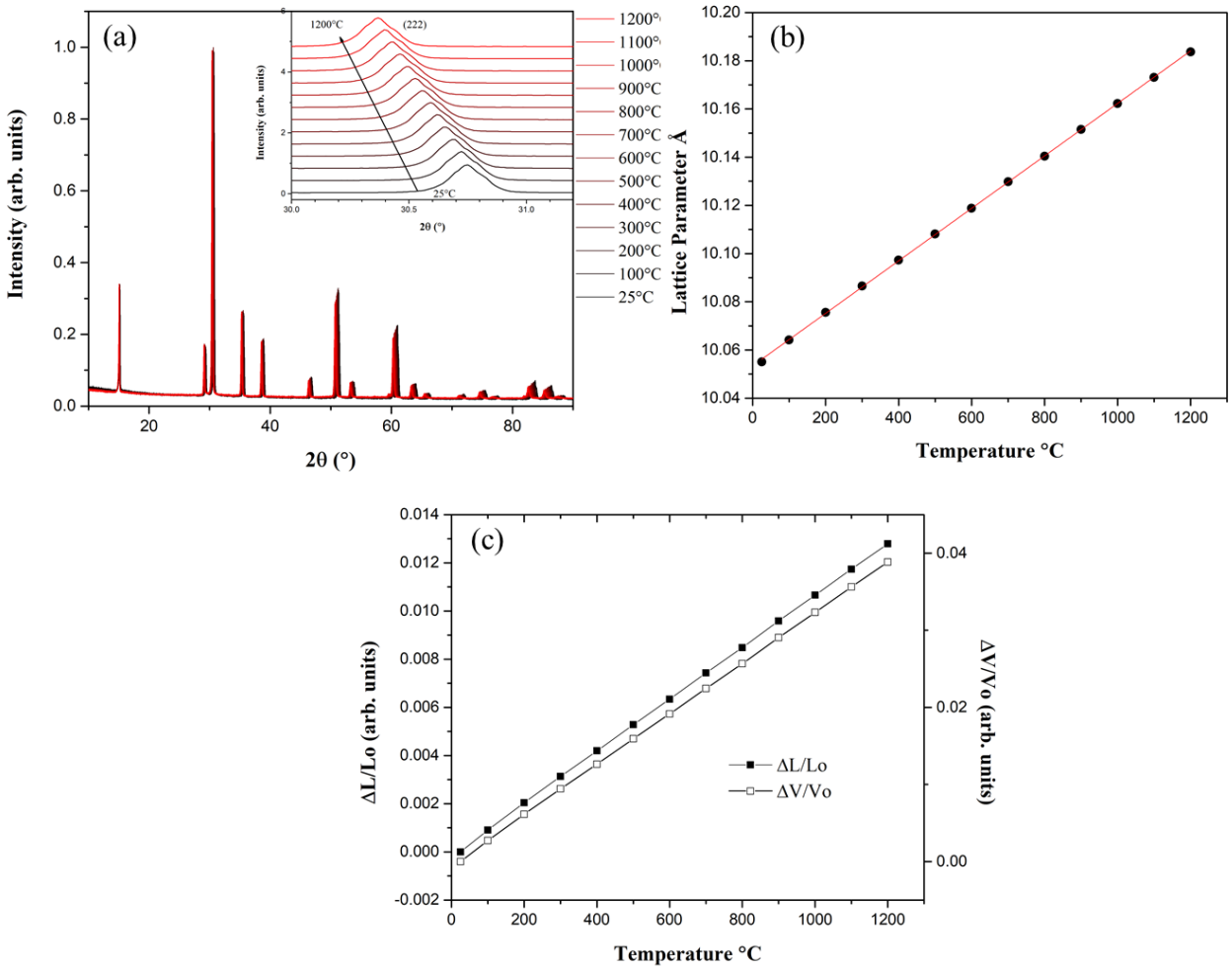

Figure 6.2: (a) Non-ambient X-ray diffraction plot for $(YbHoErTmLu)_2Ti_2O_7$ showing the pyrochlore structure expanding uniformly from 25˚C to 1200˚C. Inset is the expanded view of a diffraction peak from 30 to 31 ˚2θ. (b) Lattice parameter shift as a function of temperature up to 1200˚C. (c) Length and volume trends with respect to temperature.

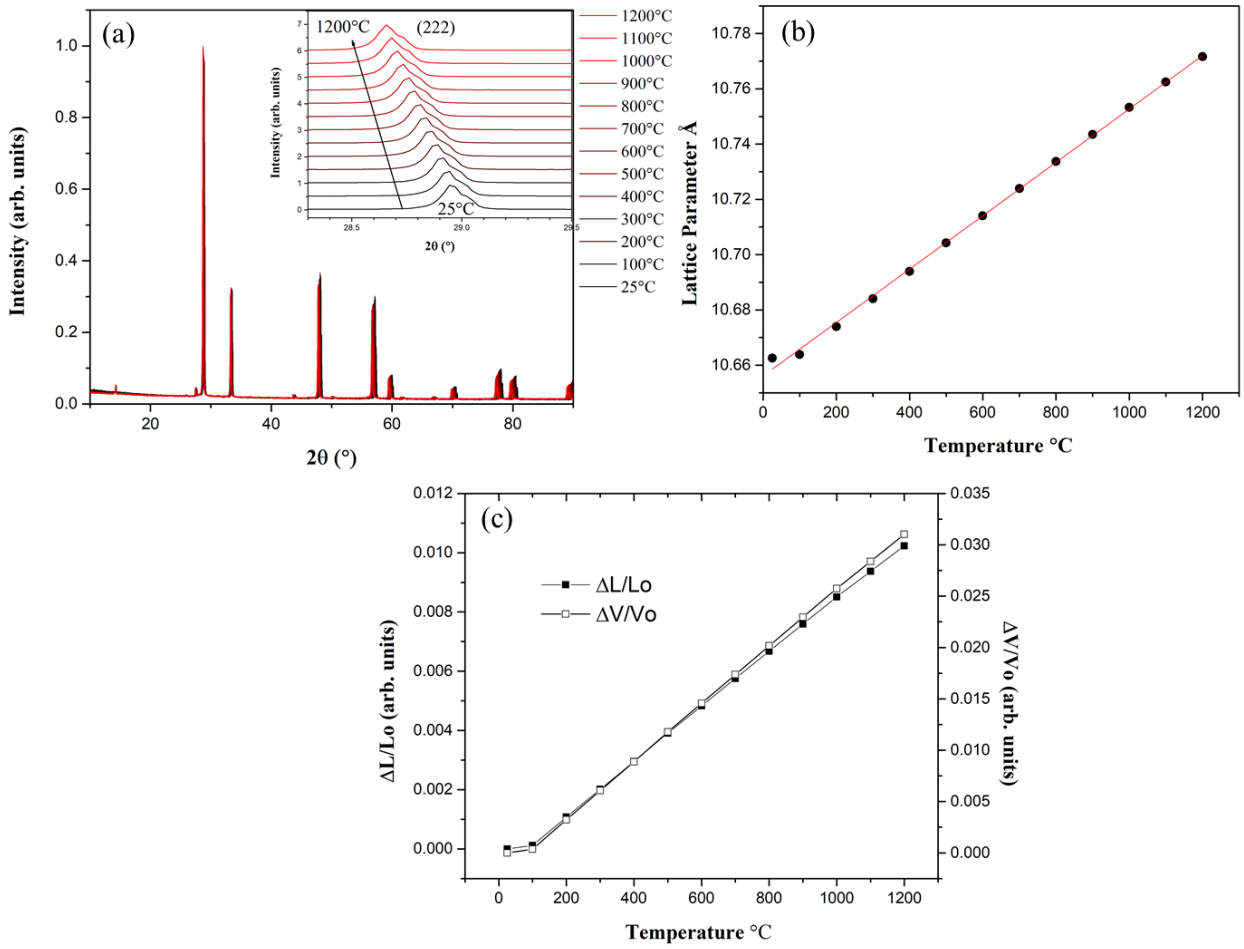

Figure 6.3: (a) Non-ambient X-ray diffraction plot for $(EuNdSmLaPr)_2Hf_2O_7$ showing the pyrochlore structure expanding uniformly from 25˚C to 1200˚C. Inset is the expanded view of a diffraction peak from 29.5 to 29.5 ˚2θ. (b) Lattice parameter shift as a function of temperature up to 1200˚C. (c) Length and volume trends with respect to temperature.

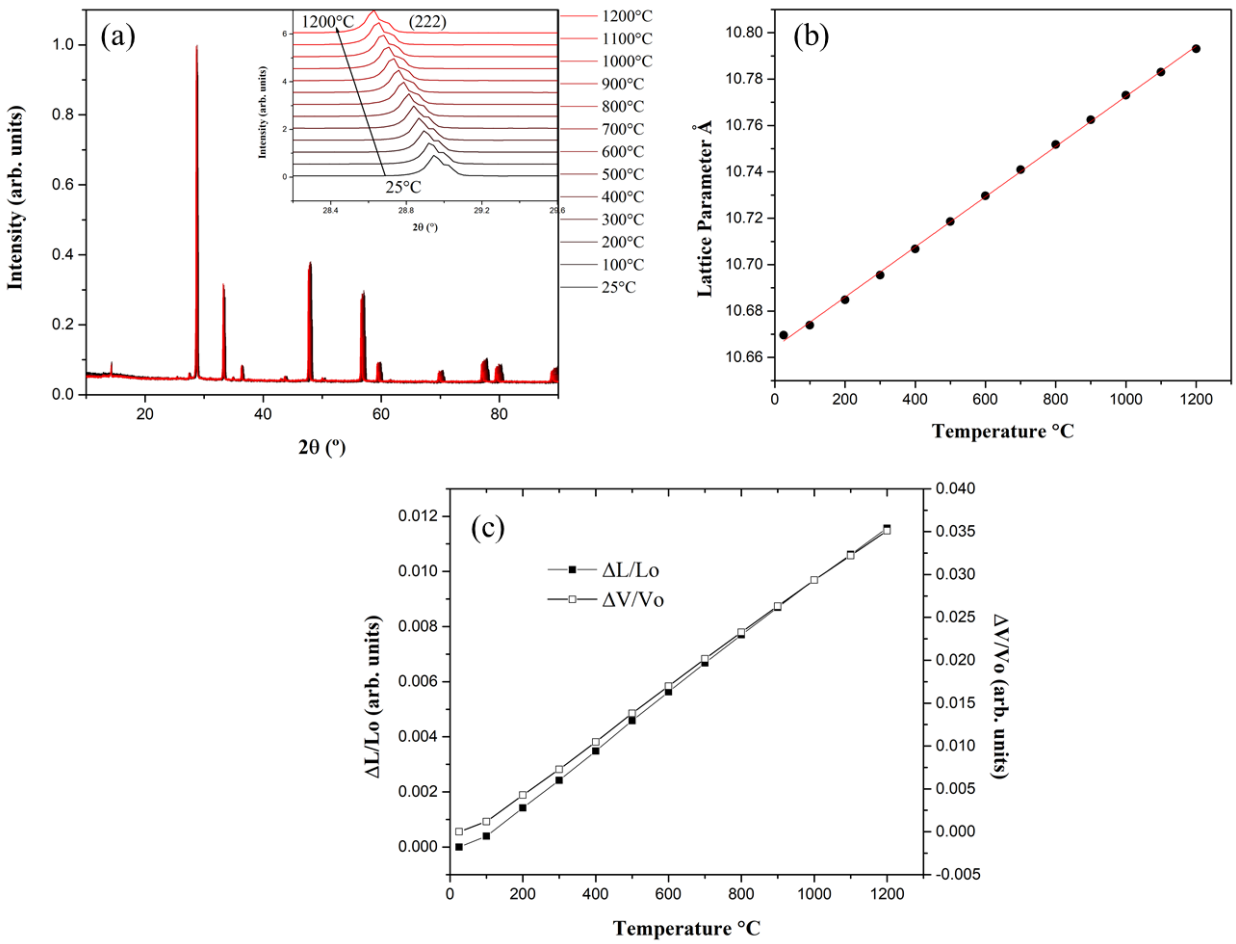

Figure 6.4: (a) Non-ambient X-ray diffraction plot for $(GdNdSmLaPr)_2Zr_2O_7$ showing the pyrochlore structure expanding uniformly from 25˚C to 1200˚C. Inset is the expanded view of a diffraction peak from 28.4 to 29.6 ˚2θ. (b) Lattice parameter shift as a function of temperature up to 1200˚C. (c) Length and volume trends with respect to temperature.

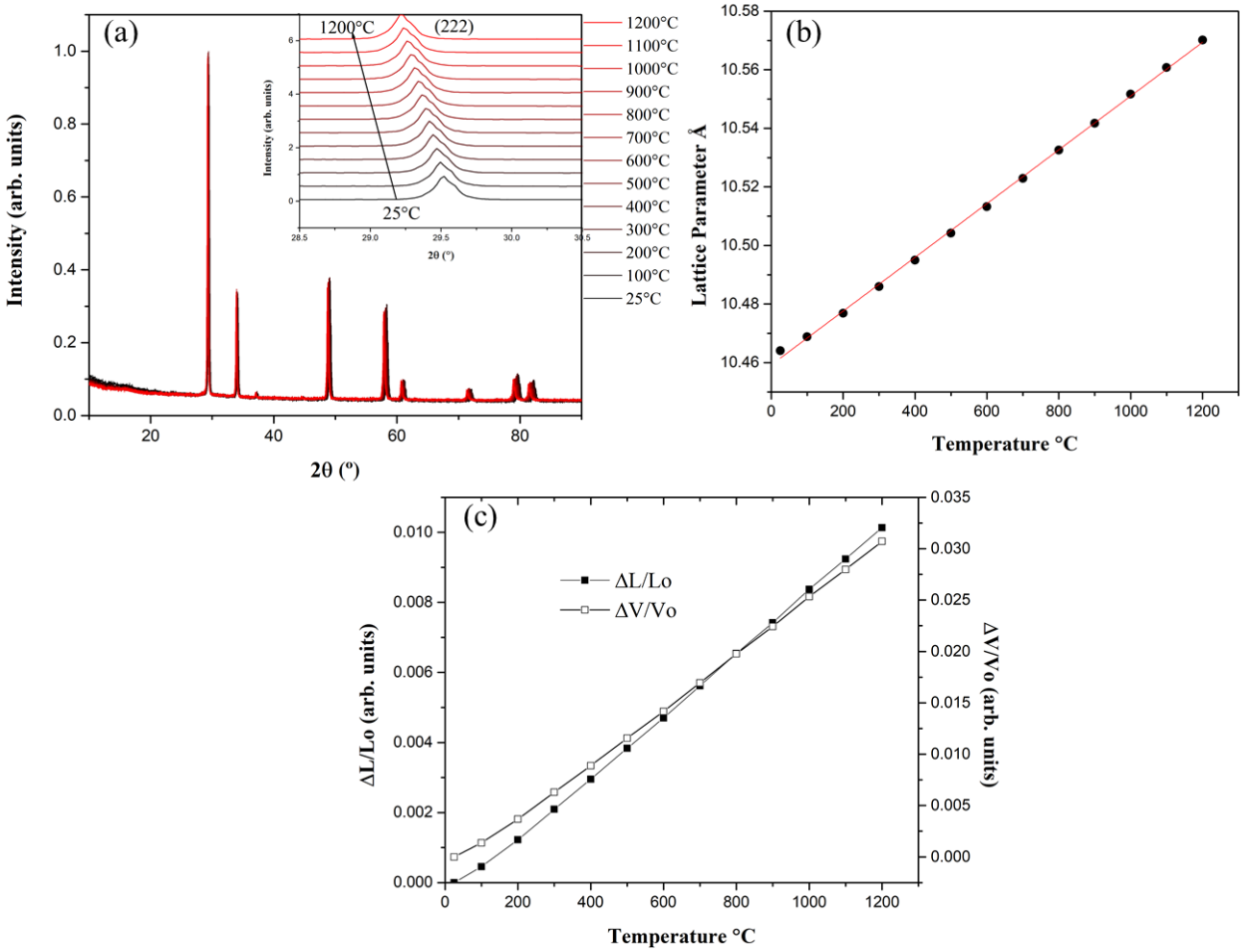

Figure 6.5: (a) Non-ambient X-ray diffraction plot for $(DyHoSmGdNd)_2Sn_2O_7$ showing the pyrochlore structure expanding uniformly from 25˚C to 1200˚C. Inset is the expanded view of a diffraction peak from 28.5 to 30.5 ˚2θ. (b) Lattice parameter shift as a function of temperature up to 1200˚C. (c) Length and volume trends with respect to temperature.

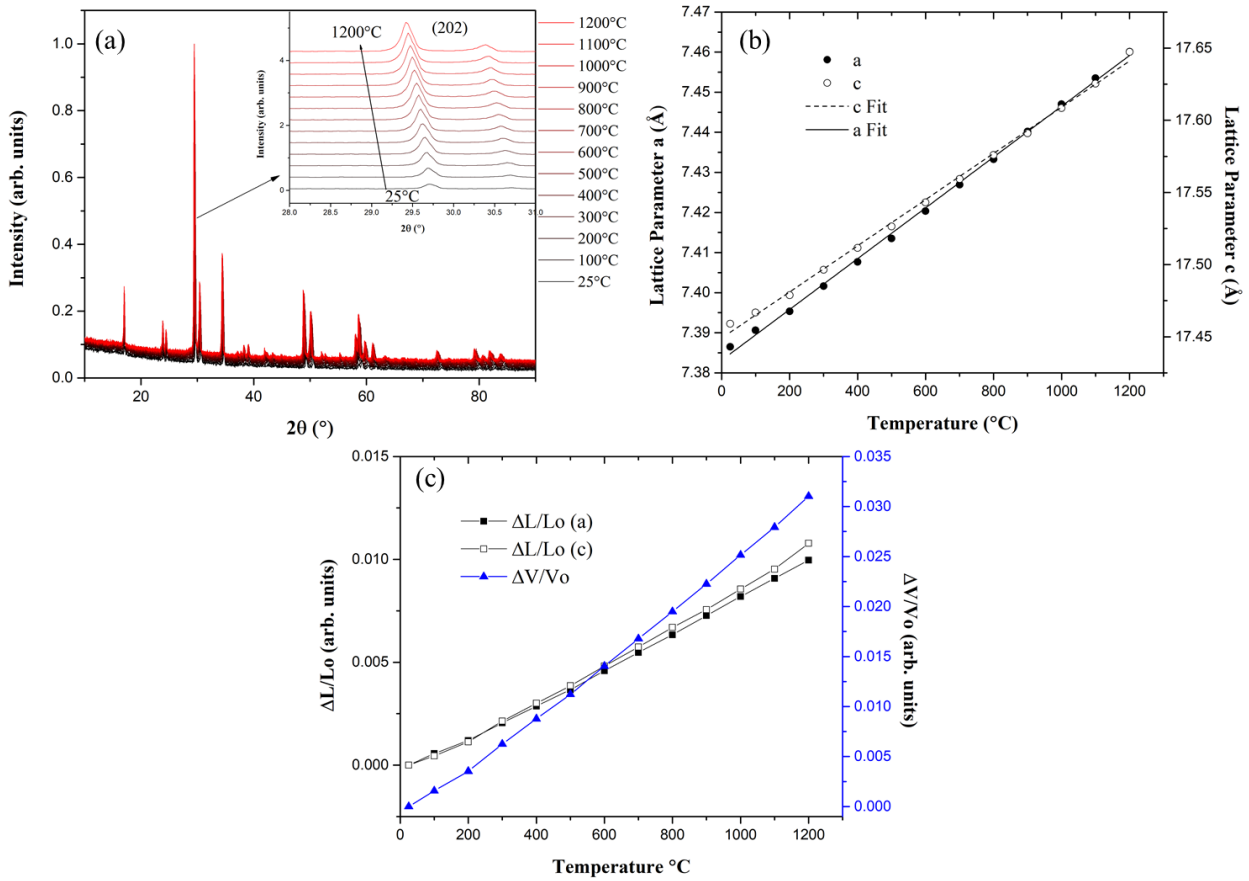

Figure 6.6: (a) Non-ambient X-ray diffraction plot for $(NdSmEuGd)_3Sb_3Mg_2O_{14}$ showing the rhombohedral kagome structure expanding uniformly from 25˚C to 1200˚C. Inset is the expanded view of a diffraction peak from 28 to 31˚2θ. (b) Lattice parameter shift as a function of temperature up to 1200˚C. (c) Length and volume trends with respect to temperature.

Table 6.1: List of experimentally derived linear thermal expansion coefficients for each HEO pyrochlore-type composition.

HEO Composition	Linear Expansion Coefficient α_L (°C^{-1})
$(YbTbGdErDy)_2Ti_2O_7$	11.0×10^{-6}
$(YbHoTmErLu)_2Ti_2O_7$	10.8×10^{-6}
$(DyHoSmGdNd)_2Sn_2O_7$	8.77×10^{-6}
$(EuPrSmLaNd)_2Hf_2O_7$	9.06×10^{-6}
$(GdNdSmPrLa)_2Zr_2O_7$	10.1×10^{-6}
$(NdSmEuGd)_3Sb_3Mg_2O_{14}$	8.58×10^{-6}
	9.16×10^{-6}

6.3 Discussion and Summary

High-temperature X-ray diffraction results (Figures 6.1 through 6.6) indicate that these HEO compositions expand uniformly from 25˚C to 1200˚C with no observable irregularities or change in phase. Equation 6.1 was used to determine the linear expansion coefficient for each composition (Table 6.1),

$$\alpha_L = \frac{1}{L_o}\frac{\Delta L}{\Delta T}, \tag{6.1}$$

where α_L is the linear expansion coefficient, L_o is initial length, ΔL is change in length, and ΔT temperature change, All expansion coefficients are comparable (~ < 22% difference). The HEO pyrochlore compositions' expansion coefficients presented here fall in the range of previously published thermal expansion coefficients of single component pyrochlores [43-45]. Kutty et al. found that RE zirconates and hafnates' thermal expansion coefficients fell in the range of 8 to 11×10^{-6} K^{-1}, which is agreeable with the HEO hafnate and zirconate pyrochlores. Similarly, a study on RE stannate pyrochlores found thermal expansion coefficients in the range of 7 to 9×10^{-6} K^{-1} [43], which is consistent with the results for our HEO stannate pyrochlore.

The initial goal of this study was to determine if the addition of multiple cations on the A-sites contributed to any abnormalities in the expansion of the lattice. Typical lattice expansion with increasing temperature occurs when the diffraction peaks shift to lower ˚2θ due to the inverse proportionality of the peak positions with lattice parameter. This behavior was observed for all HEO pyrochlore-type compositions investigated, confirming that configurational entropy does not prevent thermal phase stability in these specific oxide compositions. As a result, these multicomponent oxides are stable structurally up to 1200˚C and possess low thermal expansion coefficients, indicating the potential for use in high-temperature applications.

CHAPTER SEVEN
MECHANICAL PROPERTIES OF HIGH ENTROPY PYROCHLORES USING RESONANT ULTRASOUND SPECTROSCOPY

7.1 Introduction

The mechanical properties of RE pyrochlore oxides have been well studied throughout the last decade both experimentally and computationally [21,46-48,138-141]. Depending on the composition, atomic bonding, and B cation size, these reports found that the mechanical properties of pyrochlores can vary widely. Feng et al., who conducted a study comparing the experimentally derived mechanical moduli results to the theoretical predictions for RE stannate pyrochlores, showed that elastic moduli values were larger than theoretically predicted. Because of these differences between experimental and theoretical results and the many variables that can affect the elastic constants in pyrochlore oxides, it is interesting to investigate how entropy and configurational complexity play a role in the mechanical properties and compare the findings to the non-HEO counterparts. As described in earlier chapters, some studies on HEO pyrochlores have reported experimental results of mechanical properties [81-87], providing some insight into specific HEO compositions and their mechanical elasticity and hardness. However, most of these studies only provide mechanical property analysis at ambient temperature. In this chapter, we report and discuss the room temperature and temperature-dependent resonant ultrasound studies on two HEO pyrochlore titanate single crystals and one dense HEO pyrochlore hafnate polycrystal and compare their results to selected single component pyrochlores with similar composition. The synthesis and preparation of these HEO pyrochlores for RUS are described in Chapter 3.

7.2 Results and Discussion

7.2.1 HEO Rare-Earth Titanate Pyrochlores

In this section, the elastic behavior of two HEO RE titanate pyrochlore single crystals will be discussed: $(YbTbGdErDy)_2Ti_2O_7$ and $(YbHoTmErLu)_2Ti_2O_7$. These single crystals were grown and synthesized at the University of Tennessee Knoxville, as described in chapters 3, 4, and 5, using solid state reactions and floating-zone growth techniques. Resulting crystals were aligned along the [100] direction and cut from larger (centimeters) sized crystal rods, which were shaped and polished down into rectangular parallelopipeds. As previously discussed, cubic single crystals possess three independent elastic moduli, typically referred to as C_{11}, C_{12}, and C_{44}. When using RUS, these three elastic moduli are determined from the position of the sample's free resonances. As these resonances are proportional to the square-root of the elastic moduli, any shift of these resonances with temperature is a direct reflection of the elastic moduli shift with temperature. In the results that follow, we show room temperature RUS fits and moduli temperature dependence for only one of the HEO single crystal compositions. However, for the other composition, we were still able to evaluate the elastic behavior's temperature dependence by tracking its resonances with temperature. Both HEO pyrochlore titanate compositions contain a mix of magnetic RE cations on the A-site, making for interesting materials to investigate using RUS. Determining the differences in elastic response between the HEO compositions and their single component counterparts is crucial to further understand potential applications for these materials.

Table 7.1 lists the room temperature elastic constants for HEO pyrochlore $(YbHoTmErLu)_2Ti_2O_7$ and comparable single component titanate pyrochlores. The elastic constant results for the single component pyrochlores were taken from an experimental study [139] and a computational work [140]. It is determined from these results that this HEO follows the rule of mixtures and suggests that its mechanical properties are neither superior nor inferior to its parent pyrochlores, as the values of its elastic moduli fall in between those of the non-HEOs.

Table 7.1: Room temperature elastic moduli values for single crystalline HEO pyrochlore $(YbHoTmErLu)_2Ti_2O_7$ and parent non-HEO pyrochlores.

*Represents a computational study.

Composition	C_{11} (GPa)	C_{12} (GPa)	C_{44} Shear Modulus (GPa)	rms error (%)	Bulk Modulus (GPa)	Young's Modulus (GPa)	Poisson's Ratio	Reference
$(YbHoTmErLu)_2Ti_2O_7$	366	146	92	0.50	219	241	0.32	This work
$Yb_2Ti_2O_7$	318	114	82	-	182	214	0.30	[139]
$Ho_2Ti_2O_7$	355	123	98	-	200	254	0.29	[139]
$Tm_2Ti_2O_7$*	377	126	109	-	210	278	0.28	[140]
$Er_2Ti_2O_7$*	373	127	110	-	209	280	0.28	[140]
$Lu_2Ti_2O_7$*	382	125	108	-	211	277	0.28	[140]

Figure 7.1 shows the temperature dependence of the elastic constants for $(YbHoTmErLu)_2Ti_2O_7$. The data were collected from 50 to 300 K in 5 K increments using a Quantum Design VersaLab system. In this plot, C' represents the difference between C_{11} and C_{12} divided by 2 (corresponding to one of the transverse sound velocities) and is plotted alongside the shear modulus C_{44}. It can be determined from these elastic moduli trends that this HEO has typical elastic behavior in this temperature range, which is a consistent increase of the moduli going from ambient temperature (higher temperature) down to 50 K (lower temperature). Therefore, there is no indication of a transition in this material between 50 and 300 K.

Figure 7.2 is a plot of three individual resonant frequencies tracked with temperature from 5 to 350 K in 5 K increments for HEO single crystal $(YbTbGdDyEr)_2Ti_2O_7$. Like that of $(YbHoTmErLu)_2Ti_2O_7$, the material's stiffness steadily increases from 350 down to 5 K with no sign of thermodynamic irregularities, hence this composition shows normal elastic behavior which is supported by the DC magnetic susceptibility curves shown and discussed in Chapter 4.

Given the temperature ranges examined with RUS, both HEO titanate pyrochlore compositions exhibit typical elastic behavior. The room temperature elastic moduli fit for $(YbHoTmErLu)_2Ti_2O_7$ is comparable to those of the single component titanate pyrochlores, indicating analogous mechanical properties.

7.2.2 HEO Rare-Earth Hafnate Pyrochlore

This section covers the elastic response of one polycrystalline HEO hafnate pyrochlore and two single-component hafnate pyrochlores for comparison. As described in Chapter 3, the polycrystalline samples used for this study were synthesized using the solid state reaction technique. Dense pellets were achieved by hot pressing single-phase polycrystalline pellets in an argon atmosphere using a consistent pressure of 0.6 tons and temperatures ranging from 1400 to 1500˚C for 12 to 20 hours. Following a 10-hour graphite burn off, resulting pellets were checked with XRD to confirm that they maintained their single phase pyrochlore structure. These pellets were carefully shaped into rectangular parallelepiped pieces for RUS measurements, and their dimensions and masses were recorded to obtain approximate densities.

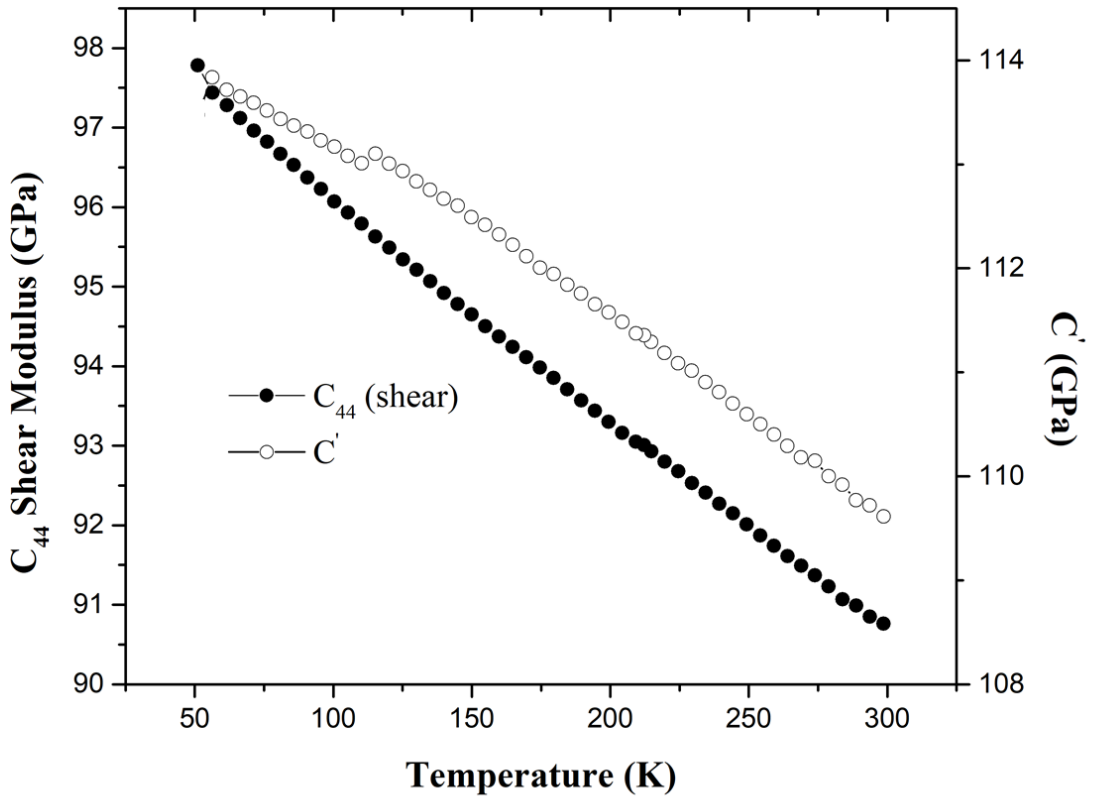

Figure 7.1: Temperature dependence of elastic constants C' and C_{44} for $(YbHoTmErLu)_2Ti_2O_7$ single crystal from 50 to 300 K.

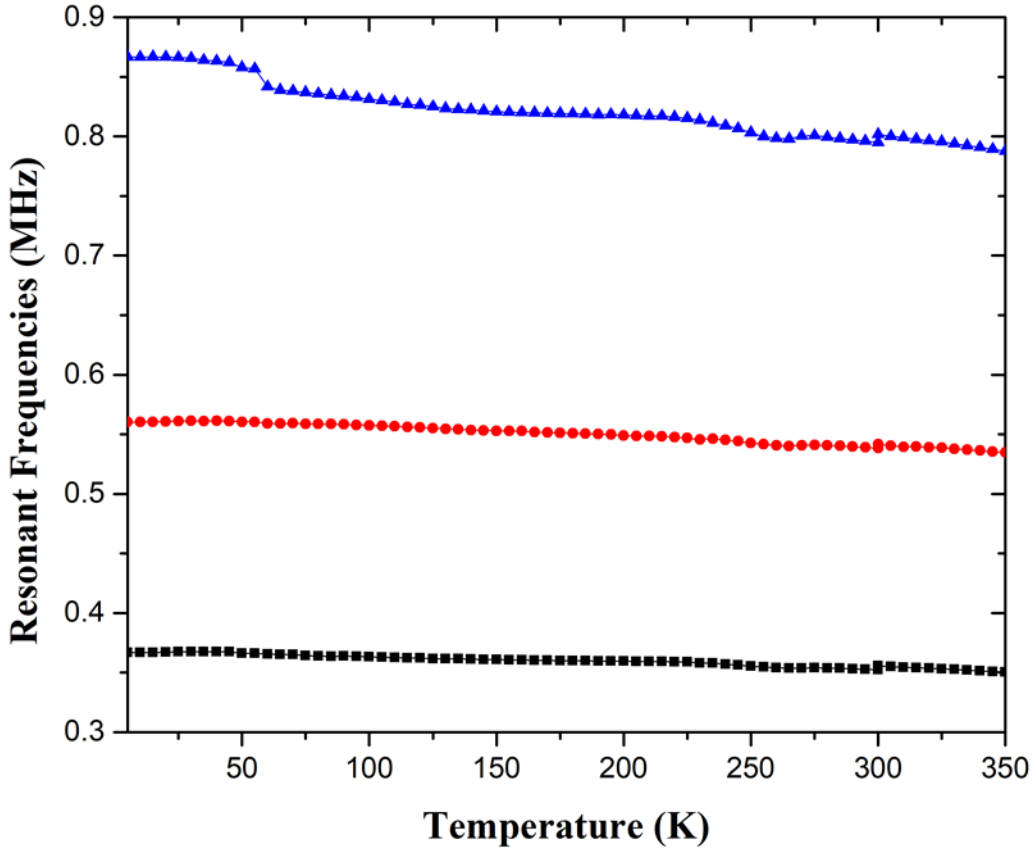

Figure 7.2: Temperature dependence showing individually tracked resonant frequencies for $(YbTbGdDyEr)_2Ti_2O_7$ single crystal from 5 to 350 K.

For polycrystals, there are only two independent elastic constants (C_{11} and C_{44}) to be determined with RUS. These, along with the calculated Bulk modulus, Young's modulus, and Poisson's ratio are reported.

Room temperature RUS measurements were carried out on each sample, with results displayed in Table 7.2 listing the experimentally derived elastic moduli, rms errors (for samples analyzed in this study), and elastic moduli published in another work [141]. When comparing the HEO hafnate's room temperature elastic constants with its non-HEO parents, it can be noted that the values are within an agreeable range. Like the titanates, further examination of this HEO and its single component counterparts was necessary by way of temperature dependent RUS to probe their elastic behavior with temperature change. Figure 7.3 presents the HEO $(EuNdSmLaPr)_2Hf_2O_7$ polycrystal's C_{11} and C_{44} values analyzed from 50 to 325 K. The HEO hafnate's elastic constants show typical elastic behavior at lower temperatures (from 50 to ~290 K). However, beginning near room temperature and increasing up to 325 K, a sharp change in the elastic behavior, or softening of the elastic constants, is observed. Alternatively, this change in elasticity cannot be explained via high-temperature X-ray diffraction, as shown in Chapter 6, where this HEO hafnate was examined from room temperature up to 1200˚C. The XRD patterns at these temperatures show no sign of a structural change. Likewise, magnetic susceptibility versus temperature (Figure E2 in Appendix E) measurements on this composition show no indication of a magnetic transition.

To better understand this behavior, the elastic constants of polycrystalline $La_2Hf_2O_7$ and $Nd_2Hf_2O_7$ were also studied for comparison purposes. Figure 7.4(a) and (b) unveils the C_{44} elastic constant trend from 50 to 350 K for the $La_2Hf_2O_7$ and $Nd_2Hf_2O_7$ samples compared to $(EuNdSmLaPr)_2Hf_2O_7$. Both compositions exhibit typical elastic behavior in this temperature range, with the HEO hafnate having lower shear modulus values in comparison.

Table 7.2: Room temperature elastic moduli values for polycrystalline HEO pyrochlore $(EuPrSmLaNd)_2Hf_2O_7$ and parent non-HEO pyrochlores.

*Represents a computational study.

Composition	C_{11} (GPa)	C_{44} Shear Modulus (GPa)	rms error (%)	Bulk Modulus (GPa)	Young's Modulus (GPa)	Poisson's Ratio	Reference
$(EuPrSmLaNd)_2Hf_2O_7$	261	86	0.56	147	215	0.26	This work
$La_2Hf_2O_7$	286	90	0.56	167	228	0.27	This work
$Nd_2Hf_2O_7$	272	90	0.63	152	226	0.25	This work
$Sm_2Hf_2O_7$*	302	95	-	172	242	0.26	[141]
$Pr_2Hf_2O_7$*	288	97	-	168	243	0.27	[141]

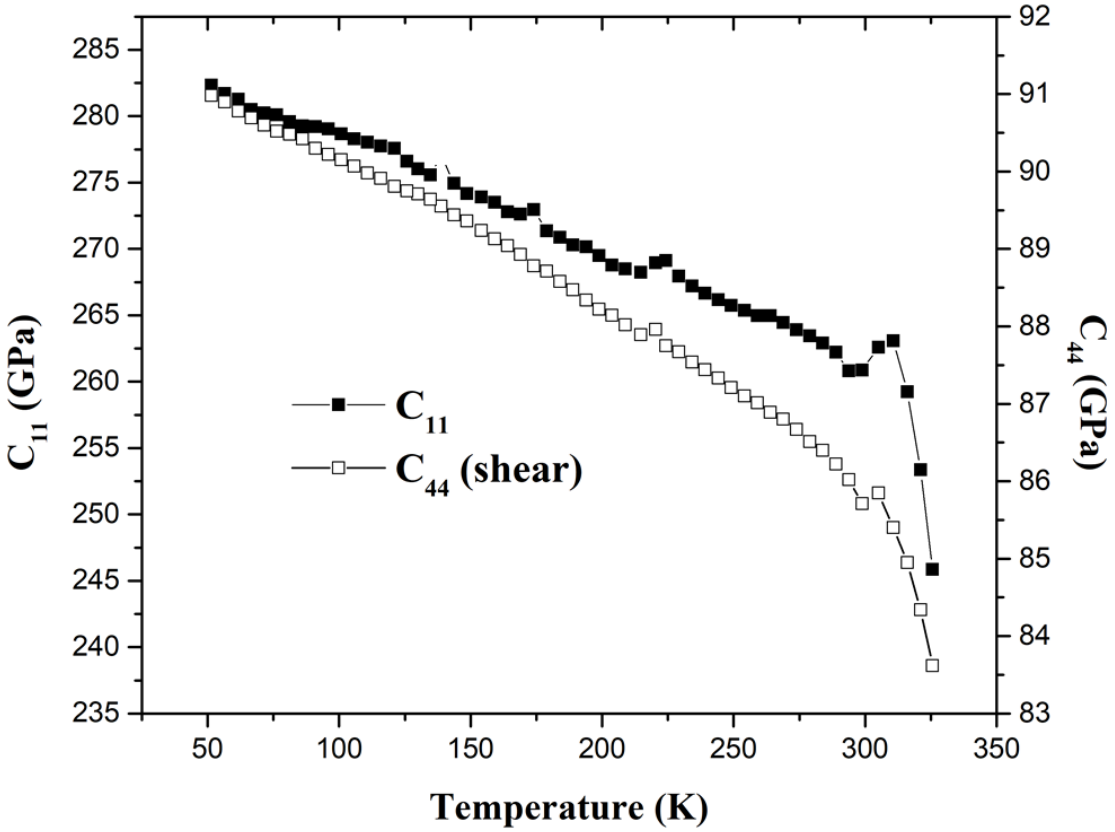

Figure 7.3: Temperature dependence of elastic constants C_{11} and C_{44} for $(EuNdSmLaPr)_2Hf_2O_7$ polycrystal from 50 to 325 K.

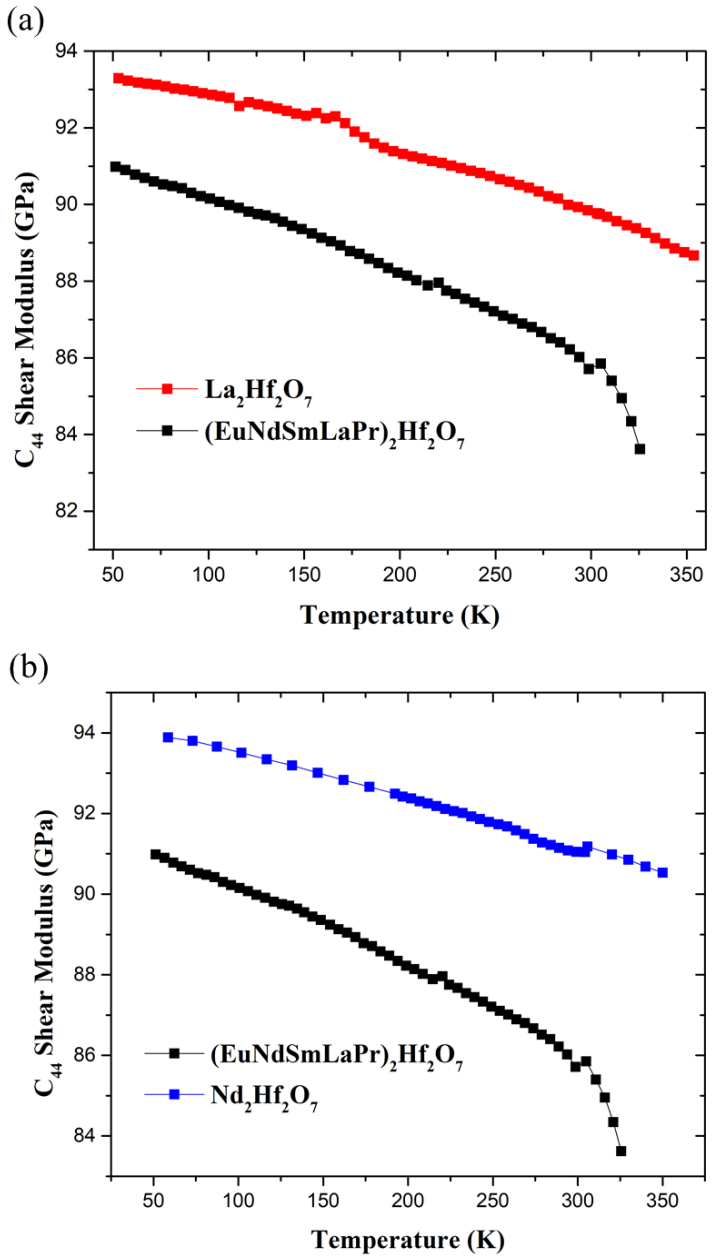

Figure 7.4: Comparison of the C_{44} (shear modulus) temperature dependence for $(EuNdSmLaPr)_2Hf_2O_7$ with polycrystalline (a) $La_2Hf_2O_7$ and (b) $Nd_2Hf_2O_7$ from 50 to 350 K.

7.3 Summary

Resonant ultrasound spectroscopy was employed to study the mechanical stiffness of three HEO pyrochlores and two parent compounds: single crystalline $(YbHoTmErLu)_2Ti_2O_7$ and $(YbTbGdDyEr)_2Ti_2O_7$ and polycrystalline $(EuNdSmLaPr)_2Hf_2O_7$, $La_2Hf_2O_7$, and $Nd_2Hf_2O_7$. Mechanical properties of the single component pyrochlores were either synthesized in this study or gathered from other publications for comparison. The HEO titanate pyrochlores exhibit typical elastic behavior with temperature change, and $(YbHoTmErLu)_2Ti_2O_7$ has room temperature elastic constants that fall within an expected range when compared to single component compositions. These results point to comparable mechanical properties. Likewise, HEO hafnate pyrochlore $(EuNdSmLaPr)_2Hf_2O_7$ possesses elastic constants that are within range in comparison to the single component compositions; however, there is a significant softening in its elasticity between 300 and 330 K that has yet to be fully understood, warranting further investigation.

CHAPTER EIGHT
CONCLUSIONS AND RECOMMENDATIONS

In this dissertation, we report multiple RE HEO pyrochlore-type compositions that were successfully synthesized and characterized for their magnetic, mechanical, structural, and irradiation resistant properties. We expanded the study of HEOs by synthesizing large, bulk single crystals of the titanates, and probed deeper into areas of characterization that had been previously overlooked. Following the initial characterization of confirming high-quality, single-phase samples using XRD and scanning electron microscopy for elemental distribution and homogeneity, further analysis of each composition comprised of bulk magnetization and DC susceptibility measurements which led to determining the approximate effective magnetic moments and Curie-Weiss temperatures for each composition. The magnetic susceptibility measurements also showed evidence of paramagnetic behavior from 3 to 300 K. For the $(YbTbGdErDy)_2Ti_2O_7$ single crystal, low temperature AC susceptibility measurements indicated a spin freezing temperature of ~ 0.84 K with evidence to support a spin-glass ground state. Magnetism in HEOs, especially with many magnetic cations, has proven to be challenging to understand. Future suggestions for work would be to analyze the local magnetic structure by way of inelastic neutron scattering. Since we have shown that large single crystal can be synthesized, neutron scattering studies can be used for delving deeper into the local structure.

Similarly, ion-irradiation and Rutherford Backscattering Spectrometry has not yet been reported on HEO single crystals. It was discovered from this work that the $(YbTmLuErHo)_2Ti_2O_7$ composition has room temperature irradiation resistance (~ 0.13 dpa) resembling that of the single component pyrochlores previously studied and is less irradiation resistant than the heavily examined $Gd_2Ti_2O_7$. Alternatively, this same composition is being studied at higher temperatures using in-situ TEM to further understand how its amorphization resistance is affected by temperature. Likewise, preliminary ion-irradiation and Raman spectroscopy results indicate that the $(YbTbGdErDy)_2Ti_2O_7$ single crystal may possess higher amorphization resistance. Future work would be to conduct a complete room temperature ion-irradiation and RBS/C study on this composition. Furthermore, the possibility of improved

properties, such as ionic conductivity and enhanced magnetism, of multicomponent pyrochlore oxides from ion-irradiation could lead to interesting discoveries and new functionalities that have yet to be explored.

The thermal stability of the HEOs' structure was studied employing non-ambient X-ray diffraction (otherwise known as high temperature X-ray diffraction or HTXRD). All successfully synthesized HEO pyrochlore compositions were analyzed by HTXRD from room temperature up to 1200˚C and the lattice parameters extracted via sequential Rietveld refinements at each temperature interval from the resulting XRD patterns. The linear expansion coefficients were determined from these data, concluding that the HEO pyrochlores possess normal, consistent thermal expansion with no abnormalities in the structure as temperature increased. The lattice expansions displayed a linear trend for all compositions, and comparisons to reported parent compounds' expansion coefficients proved that these results were reasonable and agreeable. Due to the relatively low linear expansion coefficients and structural stability up to 1200˚C, the possibility for use in high temperature applications is significant.

Finally, resonant ultrasound spectroscopy was used for the determination of the room temperature elastic constants and mechanical response at different temperatures. The two HEO titanate pyrochlore compositions exhibited typical elastic behavior from low to high temperatures and did not show any irregularities indicative of a structural or magnetic transition. A room temperature comparison for $(YbTmLuErHo)_2Ti_2O_7$ and $(EuNdSmLaPr)_2Hf_2O_7$ with reported stiffness constants for selected single component compositions confirmed that these HEO pyrochlores have comparable mechanical properties. However, temperature dependent RUS work on $(EuNdSmLaPr)_2Hf_2O_7$ compared to its parent hafnate pyrochlores show that it has lower than expected elastic moduli, with a sharp softening occurring at higher temperatures (~ 325K). This abnormality in elastic response is not fully understood and cannot be identified by current HTXRD and magnetic susceptibility results. Further examination and characterization are necessary to determine the cause of this phenomenon.

LIST OF REFERENCES

[1] D.B. Miracle and O.N. Senkov, A critical review of high entropy alloys and related concepts, Acta. Mater. 122, 448 (2017).

[2] J.W. Yeh, S.K. Chen, S.J. Lin, J.Y. Gan, T.S. Chin, T.T. Shun, C.H. Tsau, and S.Y. Chang, Nanostructured high-entropy alloys with multiple principal elements: Novel alloy design concepts and outcomes, Adv. Eng. Mater. 6, 299 (2004).

[3] C.M. Rost, E. Sachet, T. Borman, A. Moballegh, E. Dickey, D. Hou, J. Jones, S. Curtarolo, and J.-P. Maria, Entropy-stabilized oxides, Nat. Commun. 6, 8485 (2015).

[4] R. Djenadic, A. Sarkar, O. Clemens, C. Loho, M. Botros, V. Chakravadhanula, C. Kubel, S.S. Bhattacharya, A. Gandhi, and H. Hahn, Multicomponent equiatomic rare earth oxides, Mater. Res. Lett. 5, 102 (2017).

[5] J. Gild, M. Samiee, J.L. Braun, T. Harrington, H. Vega, P.E. Hopkins, K. Vecchio, and J. Luo, High-entropy fluorite oxides, J. Eur. Ceram. Soc. 38, 3578 (2018).

[6] S. Jiang, T. Hu, J. Gild, N. Zhou, J. Nie, M. Qin, T. Harrington, K. Vecchio, and J. Luo, A new class of high-entropy perovskite oxides, Scr. Mater. 142, 116 (2018).

[7] A. Sarkar, R. Djenadic, D. Wang, C. Hein, R. Kautenburger, O. Clemens, and H. Hahn, Rare earth and transition metal based entropy stabilised perovskite type oxides, J. Eur. Ceram. Soc. 38, 2318 (2018).

[8] R. Witte, A. Sarkar, R. Kruk, B. Eggert, R.A. Brand, H. Wende, and H. Hahn, High-entropy oxides: An emerging prospect for magnetic rare-earth transition metal perovskites, Phys. Rev. Mater. 3, 034406 (2019).

[9] Y. Sharma, B.L. Musico, X. Gao, C. Hua, A.F. May, A. Herklotz, A. Rastogi, D. Mandrus, J.Yan, H.N. Lee, M.F. Chisholm, V. Keppens, and T.Z. Ward, Single-crystal high entropy perovskite oxide epitaxial films, Phys. Rev. Mater. 2, 060404 (2018).

[10] J. Dabrowa, M. Stygar, A. Mikula, A. Knapik, K. Mroczka, W. Tejchman, M. Danielewski, and M. Martin, Synthesis and microstructure of the $(Co,Cr,Fe,Mn,Ni)_3O_4$ high entropy oxide characterized by spinel structure, Mater. Lett. 216, 32 (2018).

[11] B.L. Musico, Q. Wright, T.Z. Ward, A. Grutter, E. Arenholz, D. Gilbert, D. Mandrus, and V. Keppens, Tunable magnetic ordering through cation selection in entropic spinel oxides, Phys. Rev. Mater. 3, 104416 (2019).
[12] M. Fracchia, M. Manzoli, U. Anselmi-Tamburini, and P. Ghigna, A new eight-cation inverse high entropy spinel with large configurational entropy in both tetrahedral and octahedral sites: Synthesis and cation distribution by X-ray absorption spectroscopy, Scr. Mater. 188, 26 (2020).
[13] A. Mao, H.-Z. Xiang, Z.-G. Zhang, K. Kuramoto, H. Zhang, and Y. Jia, A new class of spinel high-entropy oxides with controllable magnetic properties, J. Magn. Magn. Mater. 497, 165884 (2020).
[14] A. Sarkar, L. Velasco, D. Wang, Q. Wang, G. Talasila, L. de Biasi, C. Kubel, T. Brezesinski, S.S. Bhattacharya, H. Hahn, and B. Breitung, High entropy oxides for reversible energy storage, Nat. Commun. 9, 3400 (2018).
[15] Y. Dong, K. Rena, Y. Lu, Q. Wang, J. Liu, and Y. Wang, High-entropy environmental barrier coating for the ceramic matrix composites, J. Eur. Ceram. Soc. 39, 2574 (2019).
[16] B.L. Musico, D. Gilbert, T.Z. Ward, K. Page, E. George, J. Yan, D. Mandrus, and V. Keppens, The emergent field of high entropy oxides: Design, prospects, challenges, and opportunities for tailoring material properties, APL Mater. 8, 040912 (2020).
[17] D. Bérardan, S. Franger, A.K. Meenab, and N. Dragoe, Room temperature lithium superionic conductivity in high entropy oxides, J. Mater. Chem. A. 4, 9536 (2016).
[18] J. Zhang, J. Yan, S. Calder, Q. Zheng, M. McGuire, D. Abernathy, Y. Ren, S. Lapidus, K. Page, H. Zheng, J. Freeland, J. Budai, and R. Hermann, Long range antiferromagnetic order in a rocksalt high entropy oxide, Chem. Mater. 31, 3705 (2019).
[19] J. Zhang *et al*., Enhanced radiation resistance of nanocrystalline pyrochlore $Gd_2(Ti_{0.65}Zr_{0.35})_2O_7$, Appl. Phys. Lett. 94, 243110 (2019).
[20] R.C. Ewing, W.J. Weber, and J. Lian, Nuclear waste disposal-pyrochlore ($A_2B_2O_7$): Nuclear waste form for the immobilization of plutonium and “minor” actinides, J. Appl. Phys. 95, 5949 (2004).

[21] L. Yang, C. Zhu, Y. Sheng, H. Nian, Q. Li, P. Song, W. Lu, J. Yang, and B. Liu, Investigation of mechanical and thermal properties of rare earth pyrochlore oxides by first-principles calculations, J. Am. Ceram. Soc. 102, 2830 (2019).
[22] J. Lian, J. Chen, L.M. Wang, and R.C. Ewing, Radiation-induced amorphization of rare-earth titanate pyrochlores, Phys. Rev. B. 68, 134107 (2003).
[23] D. Yang, Y. Xia, J. Wen, J. Liang, P. Mu, Z. Wang, Y. Li, Y. Wang, Role of ion species in radiation effects of $Lu_2Ti_2O_7$ pyrochlore, J. Alloys Compd. 693, 565 (2017).
[24] I. A. Ryzhkin, Magnetic Relaxation in Rare-Earth Oxide Pyrochlores, J. Exp. Theor. Phys. 101, 481 (2005).
[25] J.S. Gardner, M.J.P. Gingras, J.E. Greedan, Magnetic pyrochlore oxides, Rev. Mod. Phys. 82, 53 (2010).
[26] J.E. Greedan, Frustrated rare earth magnetism: Spin glasses, spin liquids and spin ices in pyrochlore oxides, J. Alloys Compd. 408-412, 444 (2006).
[27] J.G. Rau and M.J. Gingras, Frustrated Quantum Rare-Earth Pyrochlores, Annu. Rev. Condens. Matter Phys. 10, 357 (2019).
[28] R. Sachan, M.F. Chisholm, X. Ou *et al.* Energetic Ion Irradiation-Induced Disordered Nanochannels for Fast Ion Conduction. *JOM* 71, 103–108 (2019). https://doi.org/10.1007/s11837-018-3171-y
[29] A. N. Radhakrishnan, P. Prabhakar Rao, S. K. Mahesh, D. S. Vaisakhan Thampi, and P. Koshy, Role of Bond Strength on the Lattice Thermal Expansion and Oxide Ion Conductivity in Quaternary Pyrochlore Solid Solutions, Inorganic Chemistry, 51 (4), 2409-2419 (2012). DOI: 10.1021/ic202383f
[30] B.J. Wuensch, K.W. Eberman, C. Heremans, E.M. Ku, Per Onnerud, Evangeline M.E. Yeo, S.M. Haile, J.K. Stalick, J.D. Jorgensen, Connection between oxygen-ion conductivity of pyrochlore fuel-cell materials and structural change with composition and temperature, Solid State Ionics, 129, (1–4), 111-133, (2000).
[31] Y.N. Han, S. Jiao, M. Xu, Y. Xu, G. Pang, S. Feng, The luminescence of ion-exchangeable defect pyrochlore $KNbWO_6 \cdot H_2O{:}xEu^{3+}$, RSC Adv.,4, 24142-24146, (2014).
[32] M.H. Du, Mn4+ emission in pyrochlore oxides, Journal of Luminescence, 157, 69-73, (2015).

[33] S-H. Choe, C-J. Yu, M. Choe, Y-H. Kye, Y-N. Han, and G. Pang, First-principles study of luminescence properties of the Eu-doped defect pyrochlore oxide KNbWO6·H2O:0.125Eu3+, Phys. Rev. B. 102, 035131 (2020).
[34] A.V. Shlyakhtina *et al*., Effect of Ca-doping on the electrical conductivity of oxide ion conductor $Yb_2Ti_2O_7$, Solid State Ionics. 179, 1004 (2008).
[35] F. Li, L. Zhou, J.X. Liu, Y. Liang, and G.J. Zhang, High-entropy pyrochlores with low thermal conductivity for thermal barrier coating materials, J. Adv. Ceram. 8, 576 (2019).
[36] Z. Zhao, H. Xiang, F.Z. Dai, Z. Peng, and Y. Zhou, $(La_{0.2}Ce_{0.2}Nd_{0.2}Sm_{0.2}Eu_{0.2})_2Zr_2O_7$: A novel high-entropy ceramic with low thermal conductivity and sluggish grain growth rate, J. Mater. Sci. Technol. 35, 2647 (2019).
[37] Z. Teng, L. Zhu, Y. Tan, S. Zeng, Y. Xia, Y. Wang, H. Zhang, Synthesis and structures of high-entropy pyrochlore oxides, J. Eur. Ceram. Soc. 40, 1639 (2020).
[38] A.J. Wright, Q. Wang, S.-T. Ko, K.-M. Chung, R. Chen, and J. Luo, Size Disorder as a Descriptor for Predicting Reduced Thermal Conductivity in Medium- and High-Entropy Pyrochlores, Scr. Mater. 181, 76 (2020).
[39] C. Kinsler-Fedon, Q. Zheng, Q. Huang, E.S. Choi, J. Yan, H. Zhou, D. Mandrus, and V. Keppens, Synthesis, characterization, and single-crystal growth of a high-entropy rare-earth pyrochlore oxide, Phys. Rev. Mater. 4 104411 (2020).
[40] Y. Fujita, K. Kinami, Y. Hanada, M. Nagao, A. Miura, S. Hirai, Y. Maruyama, S. Watauchi, Y. Takano, and I. Tanaka, Growth and Characterization of ROBiS2 High-Entropy Superconducting Single Crystals, ACS Omega, 5 (27), 16819-16825, (2020). DOI: 10.1021/acsomega.0c01969
[41] M. Pianassola, M. Loveday, B.C. Chakoumakos, M. Koschan, C.L. Melcher, and M. Zhuravleva, Crystal Growth and Elemental Homogeneity of the Multicomponent Rare-Earth Garnet (Lu1/6Y1/6Ho1/6Dy1/6Tb1/6Gd1/6)3Al5O12, Crystal Growth & Design, 20 (10), 6769-6776 (2020). DOI: 10.1021/acs.cgd.0c00887
[42] M. Pianassola, L. Stand, M. Loveday, B.C. Chakoumakos, M. Koschan, C.L. Melcher, and M. Zhuravleva, Czochralski growth and characterization of the multicomponent garnet (Lu1/4Yb1/4Y1/4Gd1/4)3Al5O12, Phys. Rev. Mater. 5 083401 (2021).

[43] J. Feng, B. Xiao, R. Zhou, W. Pan, Thermal expansion and conductivity of RE2Sn2O7 (RE=La, Nd, Sm, Gd, Er and Yb) pyrochlores, Scripta Materialia, 69, (5), 401-404, (2013).
[44] G. Lan, B. Ouyang, Y. Xu, J. Song, and Y. Jiang, Predictions of thermal expansion coefficients of rare-earth zirconate pyrochlores: A quasi-harmonic approximation based on stable phonon modes, Journal of Applied Physics, 119, 235103 (2016).
[45] K.V. Govindan Kutty, S. Rajagopalan, C.K. Mathews, U.V. Varadaraju, Thermal expansion behaviour of some rare earth oxide pyrochlores, Materials Research Bulletin, 29, 759-766, (1994).
[46] J. Feng, B. Xiao, Z.X. Qu, R. Zhou, and W. Pan, Mechanical properties of rare earth stannate pyrochlores, Appl. Phys. Lett. 99, 201909 (2011).
[47] J. Feng, B. Xiao, C.L. Wan, Z.X. Qu, Z.C. Huang, J.C. Chen, R. Zhou, W. Pan, Electronic structure, mechanical properties and thermal conductivity of Ln2Zr2O7 (Ln=La, Pr, Nd, Sm, Eu and Gd) pyrochlore, Acta Materialia, 59, 1742-1760 (2011).
[48] B. Liu, J.Y. Wang, F.Z. Li, Y.C. Zhou, Theoretical elastic stiffness, structural stability and thermal conductivity of La2T2O7 (T=Ge, Ti, Sn, Zr, Hf) pyrochlore, Acta Materialia, 58, 4369-4377 (2010).
[49] R. Sachan, E. Zarkadoula, X. Ou, C. Trautmann, Y. Zhang, M. F. Chisholm, and W. J. Weber, Sculpting Nanoscale Functional Channels in Complex Oxides Using Energetic Ions and Electrons, ACS Applied Materials & Interfaces, 10 (19), 16731-16738 (2018). DOI: 10.1021/acsami.8b02326
[50] C. A. Taylor, M. K. Patel, J. A. Aguiar, Y. Zhang, M. L. Crespillo, J. Wen, H. Xue, Y. Wang, W. J. Weber, Combined effects of radiation damage and He accumulation on bubble nucleation in Gd2Ti2O7, Journal of Nuclear Materials, 479, 542-547 (2016).
[51] M.A. Subramanian, G. Aravamudan, and G.V. Subba Rao, Oxide pyrochlores—a review, Prog. Solid State Chem. 15, 55 (1983).
[52] H. Zhou and C.R. Wiebe, High-Pressure Routes to New Pyrochlores and Novel Magnetism, Inorganics 7, 49 (2019).
[53] C.R. Wiebe and A.M. Hallas, Frustration under pressure: Exotic magnetism in new pyrochlore oxides, APL Materials 3, 041519 (2015).

[54] A. R. Heredia, M. Quintana Garcia, J.L. Perez Mazariego, and R. Escamilla, X-ray diffraction and Raman spectroscopy on $Gd_2(Ti_{2-y}\ Te_y)O_7$ prepared at high pressure and high temperature, J. Alloys Compd. 504, 446 (2010).
[55] G. Ehlers, J. S. Gardner, C. H. Booth, M. Daniel, K. C. Kam, A. K. Cheetham, D. Antonio, H. E. Brooks, A. L. Cornelius, S. T. Bramwell, J. Lago, W. Häussler, and N. Rosov, Dynamics of diluted Ho spin ice Ho2−xYxTi2O7 studied by neutron spin echo spectroscopy and ac susceptibility, Phys. Rev. B 73, 174429 (2006).
[56] Z.L. Dun, J. Trinh, K. Li, M. Lee, K. W. Chen, R. Baumbach, Y. F. Hu, Y. X. Wang, E. S. Choi, B. S. Shastry, A. P. Ramirez, and H. D. Zhou, Magnetic Ground States of the Rare-Earth Tripod Kagome Lattice Mg2RE3Sb3O14 (RE=Gd,Dy,Er), Phys. Rev. Lett. 116, 157201 (2016).
[57] Z.L. Dun, X. Bai, M.B. Stone, H.D. Zhou, and M. Mourigal, Effective point-charge analysis of crystal electric fields -- application to rare-earth pyrochlores and tripod kagome magnets R3Mg2Sb3O14, arXiv:2004.10957 (2020).
[58] K. Li, Y. Hu, Y. Wang, T. Kamiyama, B. Wang, Z. Li, and J. Lin, Syntheses and properties of a family of new compounds RE3Sb3Co2O14 (RE=La, Pr, Nd, Sm–Ho) with an ordered pyrochlore structure, Journal of Solid State Chemistry, 217, 80-86, (2014).
[59] M. B. Sanders, J.W. Krizan, and R. J. Cava, RE3Sb3Zn2O14 (RE = La, Pr, Nd, Sm, Eu, Gd): a new family of pyrochlore derivatives with rare earth ions on a 2D Kagome lattice, J. Mater. Chem. C, 4, 541-550, (2016).
[60] B. Cantor, I.T.H. Chang, P. Knight, A.J.B. Vincent, Microstructural development in equiatomic multicomponent alloys, Materials Science and Engineering: A, 375–377, 213-218 (2004).
[61] M. Dada, P. Popoola, and N. Mathe, "Recent advances of high entropy alloys for aerospace applications: a review", World Journal of Engineering, Vol. ahead-of-print No. ahead-of-print, (2021). https://doi.org/10.1108/WJE-01-2021-0040.
[62] E.P. George, D. Raabe, and R.O. Ritchie, High-entropy alloys. Nat Rev Mater 4, 515–534 (2019). https://doi.org/10.1038/s41578-019-0121-4
[63] J. Gild, Y. Zhang, T. Harrington, S. Jiang, T. Hu, M. C. Quinn, W. M. Mellor, N. Zhou, K. Vecchio, and J. Luo, High-Entropy Metal Diborides: A New Class of High-Entropy Materials and a New Type of Ultrahigh Temperature Ceramics, Sci. Rep. 6, 37946 (2016).

[64] J. Zhou, J. Zhang, F. Zhang, B. Niu, L. Lei, and W. Wang, High-entropy carbide: A novel class of multicomponent ceramics, Ceram. Int. 44, 22014 (2018).
[65] R.-Z. Zhang, F. Gucci, H. Zhu, K. Chen, and M. J. Reece, Data-Driven Design of Ecofriendly Thermoelectric High-Entropy Sulfides, Inorg. Chem. 57, 13027 (2018).
[66] X. Chen and Y. Wu, High-entropy transparent fluoride laser ceramics, J. Am. Ceram. Soc. 103, 750 (2020).
[67] A. Salian and S. Mandal, Entropy stabilized multicomponent oxides with diverse functionality – a review, Critical Reviews in Solid State and Materials Sciences, (2021).
[68] S. Akrami, P. Edalati, M. Fuji, K. Edalati, High-entropy ceramics: Review of principles, production and applications, Materials Science and Engineering: R: Reports, 146, 100644 (2021).
[69] B.S. Murty, J.W. Yeh, S. Ranganathan, P.P. Bhattacharjee, High-entropy ceramics, High-Entropy Alloys (Second Edition), Elsevier, Pgs. 165-176, ISBN 9780128160671 (2019). https://doi.org/10.1016/B978-0-12-816067-1.00009-6.
[70] S.J. McCormack and A. Navrotsky, Thermodynamics of high entropy oxides, Acta Materialia, 202, 1-21, 1359-6454 (2021).
[71] K. Ren, Q. Wang, G. Shao, X. Zhao, Y. Wang, Multicomponent high-entropy zirconates with comprehensive properties for advanced thermal barrier coating,
Scripta Materialia, 178, 382-386, ISSN 1359-6462, (2020).
https://doi.org/10.1016/j.scriptamat.2019.12.006.
[72] L. Zhou, F. Li, J.-X. Liu, Q. Hu, W. Bao, Y. Wu, X. Cao, F. Xu, G.-J. Zhang, High-entropy thermal barrier coating of rare-earth zirconate: A case study on (La0.2Nd0.2Sm0.2Eu0.2Gd0.2)2Zr2O7 prepared by atmospheric plasma spraying, Journal of the European Ceramic Society, 40 (15), 5731-5739, ISSN 0955-2219, (2020).
https://doi.org/10.1016/j.jeurceramsoc.2020.07.061.
[73] K. Zhang, W. Li, J. Zeng, T. Deng, B. Luo, H. Zhang, X. Huang, Preparation of (La0.2Nd0.2Sm0.2Gd0.2Yb0.2)2Zr2O7 high-entropy transparent ceramic using combustion synthesized nanopowder, Journal of Alloys and Compounds, 817, 153328, ISSN 0925-8388, (2020). https://doi.org/10.1016/j.jallcom.2019.153328.

[74] H. Yang, G. Lin, H. Bu, H. Liu, L. Yang, W. Wang, X. Lin, C. Fu, Y. Wang, C. Zeng, Single-phase forming ability of high-entropy ceramics from a size disorder perspective: A case study of (La0.2Eu0.2Gd0.2Y0.2Yb0.2)2Zr2O7, Ceramics International, 48 (5), 6956-6965, ISSN 0272-8842, (2022). https://doi.org/10.1016/j.ceramint.2021.11.252.
[75] B. Matović, D. Zagorac, I. Cvijović-Alagić, J. Zagorac, S. Butulija, J. Erčić, O. Hanzel, R. Sedlák, M. Lisnichuk, and P. Tatarko, Fabrication and characterization of high entropy pyrochlore ceramics, Boletín de la Sociedad Española de Cerámica y Vidrio, ISSN 0366-3175, (2021). https://doi.org/10.1016/j.bsecv.2021.11.002.
[76] X. Meng, J. Xu, J. Zhu, P. Zhang, A. Rydosz, M.J. Reece, and F. Gao, Pyrochlore-fluorite dual-phase high-entropy ceramic foams with extremely low thermal conductivity from particle-stabilized suspension, Scripta Materialia, 194, 113714, ISSN 1359-6462, (2021). https://doi.org/10.1016/j.scriptamat.2020.113714.
[77] D. Liu, Y. Wang, F. Zhou, B. Xu, and B. Lv, A novel high-entropy (Sm0.2Eu0.2Tb0.2Dy0.2Lu0.2)2Zr2O7 ceramic aerogel with ultralow thermal conductivity, Ceramics International, 47(21), 29960-29968, ISSN 0272-8842 (2021). https://doi.org/10.1016/j.ceramint.2021.07.170.
[78] Y. Han, R. Yu, H. Liu, and Y. Chu, Synthesis of the superfine high-entropy zirconate nanopowders by polymerized complex method. J Adv Ceram, 11, 136–144 (2022). https://doi.org/10.1007/s40145-021-0522-x.
[79] X. Luo, L. Luo, X. Zhao, H. Cai, S. Duan, C. Xu, S. Huang, H. Jin, and S. Hou, Single-phase rare-earth high-entropy zirconates with superior thermal and mechanical properties, Journal of the European Ceramic Society, 42(5), 2391-2399, ISSN 0955-2219 (2022). https://doi.org/10.1016/j.jeurceramsoc.2021.12.080.
[80] K. Pitike, A. Macias, M. Eisenbach, C.A. Bridges, and V.R. Cooper, Computationally Accelerated Discovery of High Entropy Pyrochlore Oxides, Chemistry of Materials, 34, 1459-1472 (2022).
[81] H. Junjie, H. Guo, L. Jing, and T. Jingchao, New class of high-entropy defect fluorite oxides RE2(Ce0.2Zr0.2Hf0.2Sn0.2Ti0.2)2O7 (RE = Y, Ho, Er, or Yb) as promising thermal barrier coatings, Journal of the European Ceramic Society, 41, 6080-6086 (2021). https://doi.org/10.1016/j.jeurceramsoc.2021.05.044.

[82] Z. Teng, Y. Tan, and H. Zhang, High-Entropy Pyrochlore $A_2B_2O_7$ with Both Heavy and Light Rare-Earth Elements at the A Site. Materials, 15, 129 (2022). https://doi.org/10.3390/ma15010129
[83] F. Vayer, C. Decorse, D. Bérardan, and N. Dragoe, New entropy-stabilized oxide with pyrochlore structure: Dy2(Ti0.2Zr0.2Hf0.2Ge0.2Sn0.2)2O7, Journal of Alloys and Compounds, 883, 160773 (2021). https://doi.org/10.1016/j.jallcom.2021.160773.
[84] Z. Teng, Y. Tan, S. Zeng, Y. Meng, C. Chen, X. Han, and H. Zhang, Preparation and phase evolution of high-entropy oxides A2B2O7 with multiple elements at A and B sites, Journal of the European Ceramic Society, 41, 3614-3620 (2021). https://doi.org/10.1016/j.jeurceramsoc.2021.01.013.
[85] G. Karthick, L. Raman, and B.S. Murty, Phase evolution and mechanical properties of novel nanocrystalline Y2(TiZrHfMoV)2O7 high entropy pyrochlore, Journal of Materials Science & Technology, 82, 214-226 (2021). https://doi.org/10.1016/j.jmst.2020.12.025.
[86] B. Jiang, C.A. Bridges, R.R. Unocic, K.C. Pitike, V.R. Cooper, Y. Zhang, D.-Y. Lin, and K. Page, Probing the Local Site Disorder and Distortion in Pyrochlore High-Entropy Oxides, Journal of the American Chemical Society, 143 (11), 4193-4204 (2021). DOI: 10.1021/jacs.0c10739
[87] Z. Zhao, H. Chen, H. Xiang, F.-Z. Dai, X. Wang, W. Xu, K. Sun, Z. Peng, and Y. Zhou, (Y0.25Yb0.25Er0.25Lu0.25)2(Zr0.5Hf0.5)2O7: A defective fluorite structured high entropy ceramic with low thermal conductivity and close thermal expansion coefficient to Al2O3, Journal of Materials Science & Technology, 39, 167-172, ISSN 1005-0302 (2020). https://doi.org/10.1016/j.jmst.2019.08.018.
[88] A.J. Wright, and J. Luo, A step forward from high-entropy ceramics to compositionally complex ceramics: a new perspective. J Mater Sci 55, 9812–9827 (2020). https://doi.org/10.1007/s10853-020-04583-w
[89] P.R. Jothi, W. Liyanage, B. Jiang, S. Paladugu, D. Olds, D.A. Gilbert, K. Page, Persistent Structure and Frustrated Magnetism in High Entropy Rare-Earth Zirconates. Small, 18, 2101323 (2022). https://doi.org/10.1002/smll.202101323
[90] K. Yang, K. Bryce, W. Zhu, D. Zhao, J. Lian, Multicomponent pyrochlore solid solutions with uranium incorporation – A new perspective of materials design for nuclear applications,

Journal of the European Ceramic Society, 41, 2870-2882, ISSN 0955-2219 (2021). https://doi.org/10.1016/j.jeurceramsoc.2020.12.012.
[91] L. Zhou, F. Li, J.-X.Liu, S.-K.Sun, Y. Liang, G.-J. Zhang, High-entropy A2B2O7-type oxide ceramics: A potential immobilising matrix for high-level radioactive waste, Journal of Hazardous Materials, 415, 125596, ISSN 0304-3894 (2021). https://doi.org/10.1016/j.jhazmat.2021.125596.
[92] B. H. Toby and R. B. Von Dreele, GSAS-II: The genesis of amodern open-source all purpose crystallography software package, J. Appl. Crystallogr.46, 544 (2013).
[93] A.P. Ramirez, Strongly Geometrically Frustrated Magnets, Ann. Rev. Mater. Sci. 24, 453-480 (1994).
[94] J. A. Mydosh, Disordered magnetism and spin glasses, J. Magn. Magn. Mater., 157–158, 606-610 (1996).
[95] K. Binder, and A. P. Young, Spin glasses: Experimental facts, theoretical concepts, and open questions, Rev. Mod. Phys. 58, 801 (1986).
[96] A. Migliori, J.L. Sarrao, William M. Visscher, T.M. Bell, Ming Lei, Z. Fisk, and R.G. Leisure, Resonant ultrasound spectroscopic techniques for measurement of the elastic moduli of solids, Physica B: Condensed Matter, 183, 1-24 (1993).
[97] R.G. Leisure and F.A. Willis, Resonant ultrasound spectroscopy, J. Phys.: Condens. Matter, 9, 6001 (1997).
[98] Y. Zhang, J. Jagielski, I-T., Bae, X. Xiang, L. Thomé, G. Balakrishnan, D.M. Paul, W.J. Weber, Damage evolution in Au-implanted Ho2Ti2O7 titanate pyrochlore, Nuclear Instruments and Methods in Physics Research Section B: Beam Interactions with Materials and Atoms, 268, (19), 3009-3013, (2010).
[99] Y. Zhang, W.J. Weber, V. Shutthanandan, R. Devanathan, S. Thevuthasan, G. Balakrishnan, and D.M. Paul, Damage evolution on Sm and O sublattices in Au-implanted samarium titanate pyrochlore, Journal of Applied Physics, 95, 2866 (2004).
[100] Y. Zhang, M.L. Crespillo, H. Xue, K. Jin, C.H. Chen, C.L. Fontana, J.T. Graham, W.J. Weber, New ion beam materials laboratory for materials modification and irradiation effects research, Nuclear Instruments and Methods in Physics Research Section B: Beam Interactions with Materials and Atoms, 338, 19-30 (2014).

[101] B.D. Begg, N.J. Hess, W.J. Weber, R. Devanathan, J.P. Icenhower, S. Thevuthasan, B.P. McGrail, Heavy-ion irradiation effects on structures and acid dissolution of pyrochlores, J. Nucl. Mater., 288, 208–216, (2001). doi:10.1016/S0022-3115(00)00708-X.

[102] S. O. Kucheyev, J. S. Williams, C. Jagadish, J. Zou, C. Evans, A. J. Nelson, A. V. Hamza, Phys. Rev. B 67, 11 (2003).

[103] S. Eichler, J. Gebauer, F. Borner, A. Polity, R. KrauseRehberg, E. Wendler, B. Weber, W. Wesch, H. Borner, Phys. Rev. B 56, 1393-1403 (1997).

[104] L. C. Feldman, J. W. Mayer, S. T. Picraux, Materials analysis by ion channeling: submicron crystallography. Academic Press: 1982.

[105] A. J. Princep, H. C. Walker, D. T. Adroja, D. Prabhakaran, andA. T. Boothroyd, Crystal field states of Tb3+ in the pyrochlore spin liquid Tb2Ti2O7from neutron spectroscopy, Phys. Rev. B91, 224430 (2015).

[106] A. Garbout, I. Ben Taazayet-Belgacem, and M. Ferid, Struc-tural, FTIR, XRD and Raman scattering of new rare-earth-titanate pyrochlore-type oxides Ln EuTi2O7(Ln=Gd, Dy), J.Alloys Compd. 573, 43 (2013).

[107] O. Knop, F. Brisse, and L. Castelliz, Pyrochlores V. Thermoana-lytic, X-ray, neutron, infrared, and dielectric studies of A2Ti2O7 titanates, Can. J. Chem. 47, 971 (1969).

[108] Q. J. Li, L. M. Xu, C. Fan, F. B. Zhang, Y. Y. Lv, B. Ni, Z. Y.Zhao, and X. F. Sun, Single crystal growth of the pyrochlores R2Ti2O7(R=rare earth) by the optical floating-zone method, J. Cryst. Growth. 377, 96 (2013).

[109] T. Malis, S.C. Cheng, and R.F. Egerton, EELS log-ratio technique for specimen-thickness measurement in the TEM, J.Electron Microsc. Technol. 8, 193 (1988).

[110] R.F. Egerton, Electron energy-loss spectroscopy in the TEM, Rep. Prog. Phys.72, 016502 (2009).

[111] N. Spaldin, Magnetic Materials: Fundamentals and Applications (Cambridge University Press, Cambridge, 2011).

[112] S. T. Bramwell, M. N. Field, M. J. Harris, and I. P. Parkin, Bulk magnetization of the heavy rare earth titanate pyrochlores – A series of model frustrated magnets, J. Phys.: Condens. Matter. 12, 483 (1999).

[113] J. A. Hodges, P. Bonville, A. Forget, A. Yaouanc, P. Dalmasde Reotier, G. Andre, M. Rams, K. Krolas, C. Ritter, P. C. M. Gubbens, C. T. Kaiser, P. J. C. King, and C. Baines, First-Order Transition in the Spin Dynamics of Geometrically Frustrated Yb2Ti2O7, Phys. Rev. Lett. 88, 077204 (2002).
[114] J. S. Gardner, S. R. Dunsiger, B. D. Gaulin, M. J. P. Gingras, J. E. Greedan, R. F. Kiefl, M. D. Lumsden, W. A. MacFarlane, N. P. Raju, J. E. Sonier, I. Swainson, and Z. Tun, Cooperative Paramagnetism in the Geometrically Frustrated Pyrochlore Antiferromagnet Tb2Ti2O7, Phys. Rev. Lett. 82, 1012 (1999).
[115] M. J. P. Gingras, B. C. den Hertog, M. Faucher, J. S. Gardner,S. R. Dunsiger, L. J. Chang, B. D. Gaulin, N. P. Raju, andJ. E. Greedan, Thermodynamic and single-ion properties of Tb3+within the collective paramagnetic-spin liquid state of the frustrated pyrochlore antiferromagnet $Tb_2Ti_2O_7$, Phys. Rev. B. 62, 6496 (2000).
[116] N. P. Raju, M. Dion, M.J.P. Gingras, T.E. Mason, and J.E. Greedan, Transition to long-range magnetic order in the highly frustrated insulating pyrochlore antiferromagnet $Gd_2Ti_2O_7$, Phys. Rev. B. 59, 14489 (1999).
[117] Y. M. Jana, A. Sengupta, and D. Ghosh, Estimation of single ion anisotropy in pyrochlore $Dy_2Ti_2O_7$, a geometrically frustrated system, using crystal field theory, J. Magn. Magn. Mater. 248, 7 (2002).
[118] J.D. Cashion, A.H.Cooke, M.J.M. Leask, T.L. Thorp, and M.R. Wells, Crystal growth and magnetic susceptibility of some rare-earth compounds, J. Mater. Sci. 3, 402 (1968).
[119] J.D.M. Champion, M.J. Harris, P.C.W. Holdsworth, A.S. Wills, G. Balakrishnan, S.T. Bramwell, E. Cizmar, T. Fennell, J.S. Gardner, J. Lago, D.F. McMorrow, M. Orendac, A. Orendacova, D. McK. Paul, R.I. Smith, M.T.F. Telling, and A. Wildes, ErTiO: Evidence of quantum order by disor-der in a frustrated antiferromagnet, Phys. Rev. B. 68, 020401(2003).
[120] J. A. Mydosh and I. Ebrary, Spin Glasses: An Experimental Introduction (Taylor & Francis, London, 1993).
[121] J. W. Krizan and R. J. Cava, NaCaCoF: A single crystal high-temperature pyrochlore antiferromagnet, Phys. Rev. B. 89, 214401 (2014).

[122] C. Kinsler-Fedon, L. Nuckols, C. Nelson, Z. Qi, Q. Huang, D. Mandrus, Y. Zhang, W.J. Weber, and V. Keppens, Effects of Au^{2+} irradiation induced damage in a high-entropy pyrochlore oxide single crystal, Scripta Materialia, Manuscript submitted (2022).
[123] W.J. Weber, A. Navrotsky, S. Stefanovsky, E.R. Vance, E. Vernaz, Materials Science of High-Level Nuclear Waste Immobilization, MRS Bulletin, 34, 46–53 (2009).
[124] P.E. Raison, R.G. Haire, T. Sato, T. Ogawa, Fundamental and Technological Aspects of Actinide Oxide Pyrochlores: Relevance for Immobilization Matrices, MRS Online Proc. Library, 556, 3 (1998).
[125] W.J. Weber, R.C. Ewing, Radiation Effects in Crystalline Oxide Host Phases for the Immobilization of Actinides, MRS Online Proc. Library, 713, 31 (2001).
[126] E.J. Pickering, A.W. Carruthers, P.J. Barron, S.C. Middleburgh, D.E.J. Armstrong, A.S. Gandy, High-Entropy Alloys for Advanced Nuclear Applications, Entropy, 23, 98 (2021).
[127] T. Egami, M. Ojha, O. Khorgolkhuu, D.M. Nicholson, G.M. Stocks, Local Electronic Effects and Irradiation Resistance in High-Entropy Alloys, JOM, 67, 2345–2349 (2015).
[128] S-Q. Xia, Z. Wang, T-F. Yang, Y. Zhang, Irradiation Behavior in High Entropy Alloys, J. Iron Steel Res. Int., 22, 879–884 (2015).
[129] N.A.P. Kiran Kumar, C. Li, K.J. Leonard, H. Bei, S.J. Zinkle, Microstructural stability and mechanical behavior of FeNiMnCr high entropy alloy under ion irradiation, Acta Mater., 113, 230-244 (2016).
[130] F. Wang, X. Yan, T. Wang, Y. Wu, L. Shao, M. Nastasi, Y. Lu, B. Cui, Irradiation damage in (Zr =0.25Ta0.25Nb0.25Ti0.25)C high-entropy carbide ceramics, Acta Mater., 195, 739-749 (2020).
[131] S. Moll, G. Sattonnay, L. Thomé, J. Jagielski, C. Decorse, P. Simon, I. Monnet, W. J. Weber, Irradiation damage in Gd2Ti2O7 single crystals: Ballistic versus ionization processes, Phys. Rev. B, 84, 064115 (2011).
[132] Y. Zhang, J. Lian, Z. Zhu, W.D. Bennett, L. V. Saraf, J.L. Rausch, C.A. Hendricks, R.C. Ewing, W.J. Weber, Response of strontium titanate to ion and electron irradiation, J. Nucl. Mater., 389, 303–310 (2009).

[133] J.F. Ziegler, M.D. Ziegler, J.P. Biersack, SRIM - The stopping and range of ions in matter, Nucl. Instruments Methods Phys. Res. Sect. B Beam Interact. with Mater. Atoms., 268, 1818–1823 (2010).
[134] W.J. Weber, Y. Zhang, Predicting damage production in monoatomic and multi-elemental targets using stopping and range of ions in matter code: Challenges and recommendations, Curr. Opin. Solid State Mater. Sci., 23, 100757 (2019).
[135] W.J Weber, Models and mechanisms of irradiation-induced amorphization in ceramics, Nuclear Instruments and Methods in Physics Research Section B: Beam Inter. Mater. and Atoms, 166–167, 98-106 (2000).
[136] D. Aidhy, R. Sachan, E. Zarkadoula, O. Pakarinen, M.F. Chisholm, Y. Zhang, W.J. Weber, Fast ion conductivity in strained defect-fluorite structure created by ion tracks in $Gd_2Ti_2O_7$, Sci Rep, 5, 16297 (2015).
[137] R. Sachan, V.R. Cooper, B. Liu, D.S. Aidhy, B.K. Voas, M. Lang, X. Ou, C. Trautmann, Y. Zhang, M.F. Chisholm, W.J. Weber, Forging Fast Ion Conducting Nanochannels with Swift Heavy Ions: The Correlated Role of Local Electronic and Atomic Structure, The Journal of Phys. Chem. C, 121, 975-981 (2017).
[138] G.R. Lumpkin and R.D. Aughterson, Perspectives on Pyrochlores, Defect Fluorites, and Related Compounds: Building Blocks for Chemical Diversity and Functionality, Front. Chem., 9, (2021). DOI=10.3389/fchem.2021.778140
[139] Y. Luan and V. Keppens. “Elastic Properties of Complex Transition Metal Oxides Studied by Resonant Ultrasound Spectroscopy.” The University of Tennessee, Knoxville, (2011).
[140] V.A. Chernyshev, V.P. Petrov, A.E. Nikiforov, P.A. Agzamova, N.M. Avram, “Elastic properties of rare earth pyrochlores $R_2Ti_2O_7$ (R = Gd, Tb, Dy, Ho, Er, Tm, Yb, Lu): Ab initio calculations”, Optical Materials, 72, 565-570 (2017).
[141] M. Sun, Y. Sui, K. Gao, C. Tan, L. Dai, G. Zhou, and Y. Zhang, Theoretical investigation of mechanical and thermal properties of $RE_2Hf_2O_7$ (RE=La, Ce, Pr, Nd, Pm and Sm) pyrochlore oxides, Ceramics International, 45, 9,12101-12105 (2019).

APPENDICES

APPENDIX A

LIST OF ADDITIONAL HIGH ENTROPY OXIDES SYNTHESIZED

Table A1: List of additional multicomponent oxides, their structures, synthesis technique used (solid state or polymeric steric entrapment), phase status, and characterization completed.

Composition	Structure	Synthesis technique	Single phase ?	Characterization completed
$(EuNdSmLaGd)_2Hf_2O_7$	cubic pyrochlore	SS	yes	XRD
$(YbTbGdErDy)_2Hf_2O_7$	cubic pyrochlore	SS	no	XRD
$(NdHoDySmGd)_2Mo_2O_7$	cubic pyrochlore	SS	no	XRD
$(LaPrSmHoDy)_3Sb_3Mg_2O_{14}$	tripod kagome lattice	SS and PSE	no	XRD
$Sr(TiMnNb)O_3$	perovskite	SS	yes	XRD
$(LaPrNdSmEu)_2Si_2O_7$	pyro-silicate tetragonal	SS	no	XRD
$(CeHoNdGdSm)_2Sn_2O_7$	pyrochlore	SS	yes	XRD
$(CeHoNdGdSm)_2Zr_2O_7$	pyrochlore	SS	yes	XRD
$(Yb_{0.2}Hf_{0.2}Zr_{0.2}Ce_{0.2}Y_{0.2})O_2$	fluorite	SS	yes	XRD,SEM/EDX,RUS (RT only)
$(Zr_{0.25}Hf_{0.25}Ce_{0.25})(Y_{0.0625}Gd_{0.0625}Yb_{0.0625}Ca_{0.0625})O_2$	fluorite	SS	yes	XRD,SEM/EDX,RUS (RT only)

APPENDIX B

ADDITIONAL X-RAY DIFFRACTION DATA

Table B1: Crystallographic parameters, crystal data, and room temperature structure refinement for $(YbTbGdDyEr)_2Ti_2O_7$

*Estimated standard deviations are 1σ

Powder diffraction data collection	**$(Yb_{0.2}Tb_{0.2}Gd_{0.2}Dy_{0.2}Er_{0.2})_2Ti_2O_7$**
Wavelength (Å)	1.540562
Scan Range (degree 2θ)	10 < 2θ < 90
Step Size (degree 2θ)	0.01
Temperature (K)	298
Pressure	Atmospheric
Refinement	
wRp	6.34%
Rexp	4.38%
Goodness of Fit, χ2	1.45
Software	GSAS -II
Variables:	
Overall	6 Background
Sample Displacement (μm)	78.7(3)
Instrument Parameters:	
X	1.0(3)
Crystal Data	
Crystal system	Cubic
Space group	F d -3 m
Lattice Parameter (Å)	10.1152(3)
Volume, (Å^3)	1034.9(1)
Z	8
Formula weight (g/mol)	535.321
Calculated Density (g/cm^3)	6.871

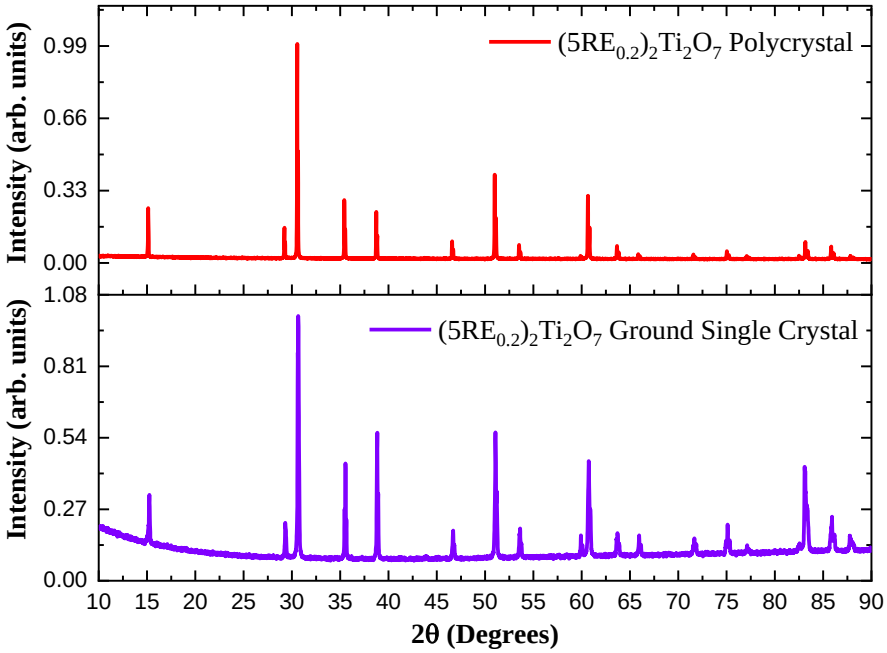

Figure B1: Room temperature powder X-ray diffraction pattern of the ground single crystal $(YbTbGdDyEr)_2Ti_2O_7$ (purple line) compared to the polycrystal (red line) having the cubic pyrochlore structure, indicating no change in phase.

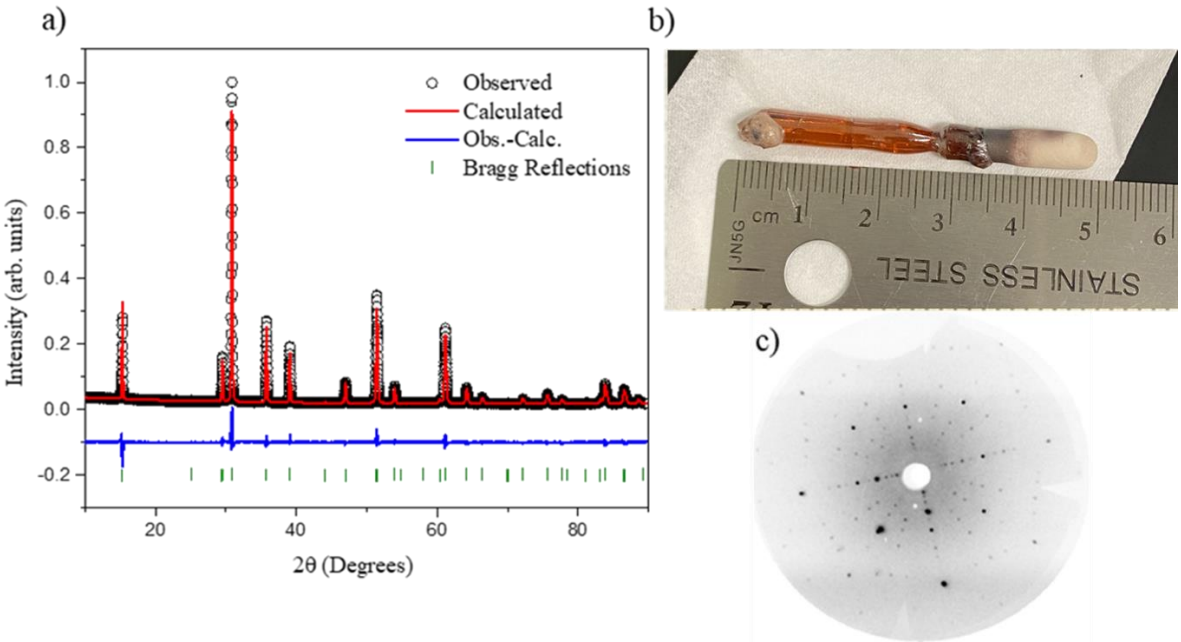

Figure B2: a) Room temperature powder X-ray diffraction of $(YbHoTmLuEr)_2Ti_2O_7$ with structure refinement. b) Resulting crystal rod from floating zone crystal growth of 2.5 cm in length c) Laue diffraction pattern of crystal in the [100] direction.

Table B2: Rietveld refinement results for the crystallographic parameters, crystal data, and room temperature structure refinement of the HEO pyrochlore $(YbTmLuHoEr)_2Ti_2O_7$.

*Estimated standard deviations are 1σ

Powder diffraction data collection	$(Yb_{0.2}Tm_{0.2}Lu_{0.2}Ho_{0.2}Er_{0.2})_2Ti_2O_7$
Wavelength (Å)	1.540562
Scan Range (degree 2θ)	10 < 2θ < 90
Step Size (degree 2θ)	0.01
Temperature (K)	298
Pressure	Atmospheric
Refinement	
wRp	5.96%
Rexp	2.12%
Goodness of Fit, χ2	2.81
Software	GSAS -II
Variables:	
Overall	4 Background
Sample Displacement (μm)	-73.0(9)
Instrument Parameters:	
X	2.4(6)
Crystal Data	
Crystal system	Cubic
Space group	F d -3 m
Lattice Parameter (Å)	10. 0551(3)
Volume, (Å^3)	1016.6(3)
Z	8
Formula weight (g/mol)	547.37
Calculated Density (g/cm^3)	7.154

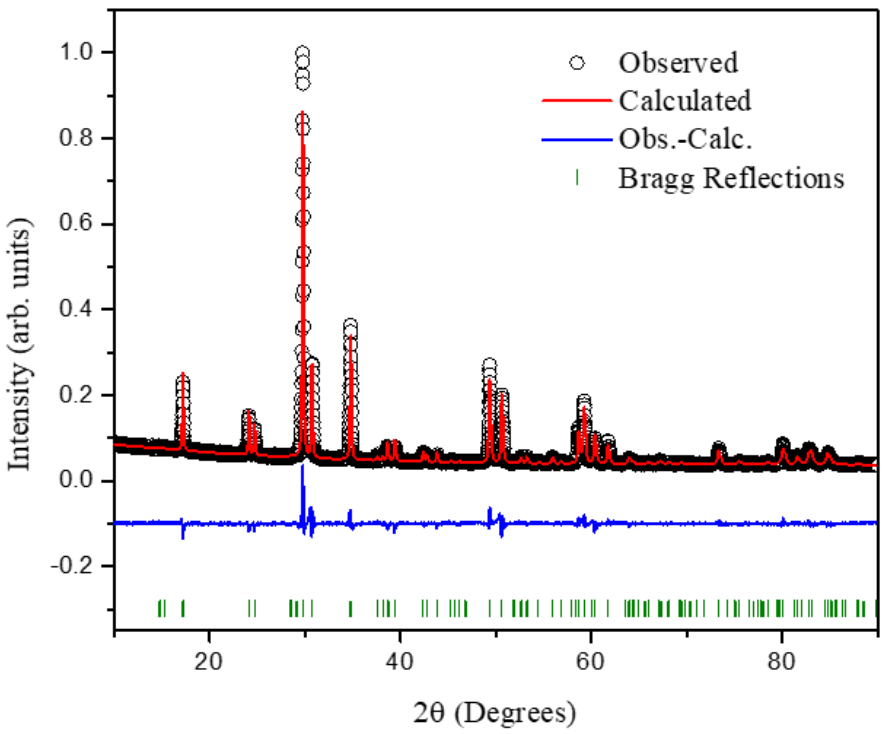

Figure B3: Room temperature powder X-ray diffraction of $(EuNdSmGd)_3Sb_3Mg_2O_{14}$ with structure refinement.

Table B3: Crystallographic parameters, crystal data, and room temperature structure refinement for $(EuSmNdGd)_3Sb_3Mg_2O_{14}$

*Estimated standard deviations are 1σ

Powder diffraction data collection	**$Gd_{0.75}Nd_{0.75}Sm_{0.75}Eu_{0.75}Sb_3Mg_2O_{14}$**
Wavelength, Å	1.540562
Scan Range, degree 2θ	10 < 2θ < 90
Step Size, degree 2θ	0.01
Temperature, K	298
Refinement	
wRp	5.64%
Rexp	2.25%
Goodness of Fit, χ2	2.51
Software	GSAS -II
Variables:	
Overall	4 Background
Instrument Parameters	
W	10.00(0)
X	91.43(3)
Crystal Data	
Crystal system	Rhombohedral
Space group	R -3 m
Lattice Parameters, Å	a=b= 7.385(3)
	c = 17.462(4)
Volume, $Å^3$	824.97(3)
Formula weight, g/mol	1090.73
Calculated Density, g/cm^3	6.586

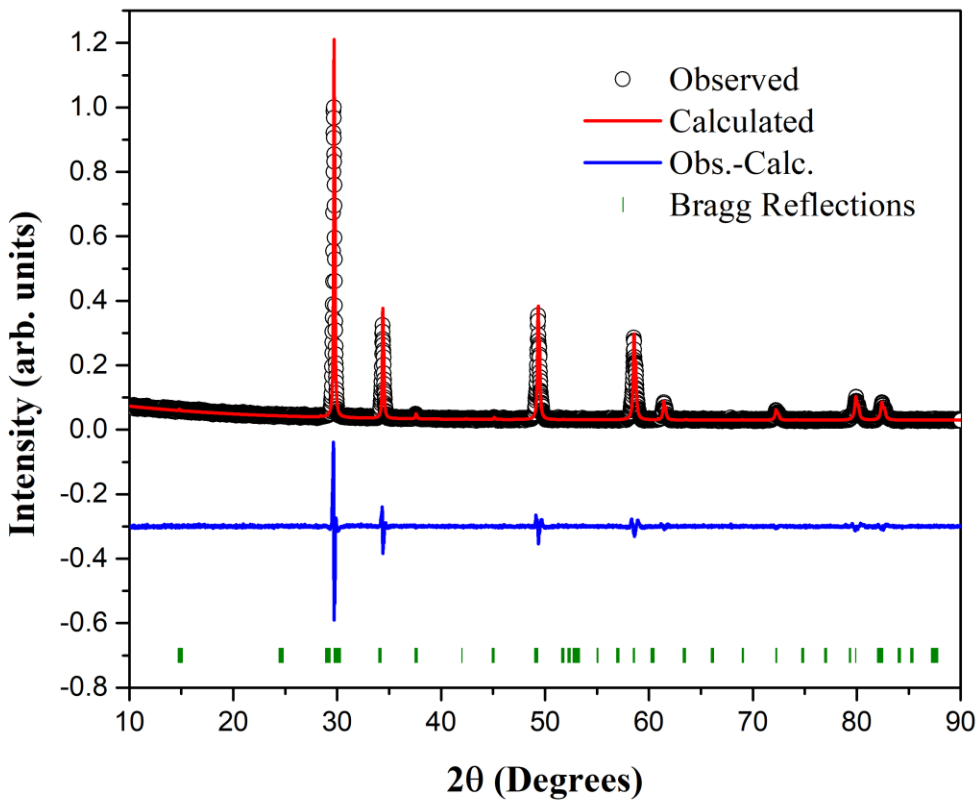

Figure B4: Room temperature powder X-ray diffraction of $(DyHoSmGdNd)_2Sn_2O_7$ with structure refinement.

Table B4: Crystallographic parameters, crystal data, and room temperature structure refinement for $(DyHoSmNdGd)_2Sn_2O_7$

*Estimated standard deviations are 1σ

Powder diffraction data collection	**$(Dy_{0.2}Ho_{0.2}Sm_{0.2}Nd_{0.2}Gd_{0.2})_2Sn_2O_7$**
Wavelength, Å	1.540562
Scan Range, degree 2θ	10 < 2θ < 90
Step Size, degree 2θ	0.01
Temperature, K	298
Refinement	
wRp	7.59%
Rexp	4.20%
Goodness of Fit, χ2	1.81
Software	GSAS -II
Variables:	
Overall	6 Background
Instrument Parameters	
W	-441.84
Crystal Data	
Crystal system	Cubic
Space group	F d -3 m
Lattice Parameter, Å	10.464(8)
Volume, $Å^3$	1146.03(2)
Z	8
Formula weight, g/mol	661.13
Calculated Density, g/cm^3	7.663

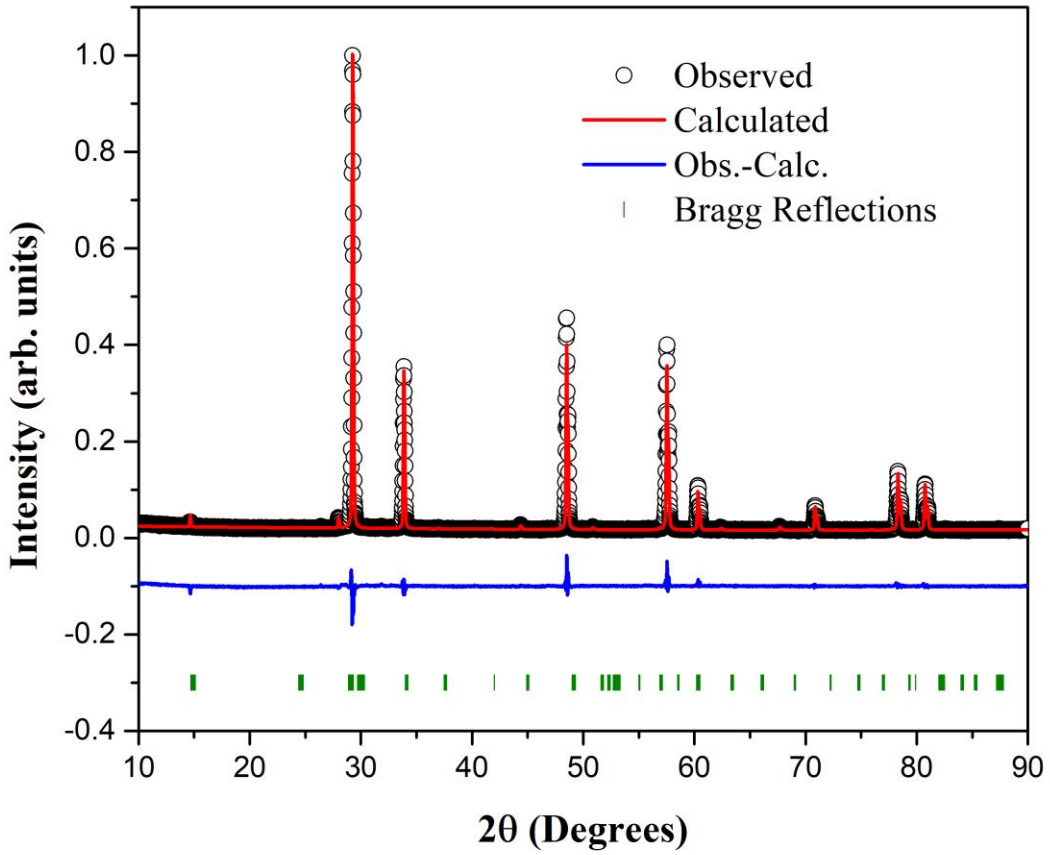

Figure B5: Room temperature powder X-ray diffraction of $(EuPrSmLaNd)_2Hf_2O_7$ with structure refinement.

Table B5: Crystallographic parameters, crystal data, and room temperature structure refinement for $(EuNdSmLaPr)_2Hf_2O_7$

*Estimated standard deviations are 1σ

Powder diffraction data collection	**$(Eu_{0.2}Nd_{0.2}Sm_{0.2}La_{0.2}Pr_{0.2})_2Hf_2O_7$**
Wavelength, Å	1.540562
Scan Range, degree 2θ	10 < 2θ < 90
Step Size, degree 2θ	0.01
Temperature, K	298
Refinement	
wRp	6.73%
Rexp	2.50%
Goodness of Fit, χ2	2.69
Software	GSAS -II
Variables:	
Overall	3 Background
Instrument Parameters	
W	14.27(6)
Crystal Data	
Crystal system	Cubic
Space group	F d -3 m
Lattice Parameter, Å	10.656(1)
Volume, $Å^3$	1210.3(0)
Z	8
Formula weight, g/mol	759.53
Calculated Density, g/cm^3	8.337

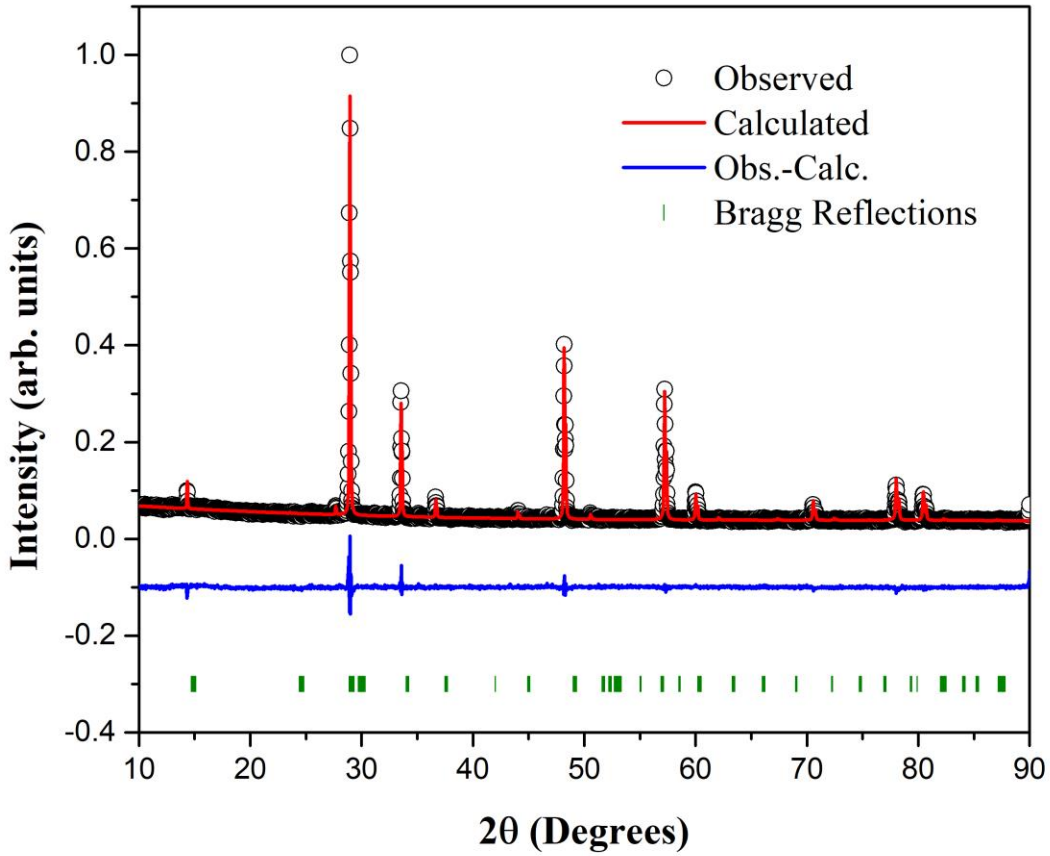

Figure B6: Room temperature powder X-ray diffraction of $(GdNdSmPrLa)_2Zr_2O_7$ with structure refinement.

Table B6: Crystallographic parameters, crystal data, and room temperature structure refinement for $(GdNdSmLaPr)_2Zr_2O_7$

*Estimated standard deviations are 1σ

Powder diffraction data collection	**$(Gd_{0.2}Nd_{0.2}Sm_{0.2}La_{0.2}Pr_{0.2})_2Zr_2O_7$**
Wavelength, Å	1.540562
Scan Range, degree 2θ	10 < 2θ < 90
Step Size, degree 2θ	0.01
Temperature, K	298
Refinement	
wRp	5.00%
Rexp	2.75%
Goodness of Fit, χ2	1.82
Software	GSAS -II
Variables:	
Overall	4 Background
Instrument Parameters	
W	4.59(6)
X	1.39(1)
Y	3.12(8)
Crystal Data	
Crystal system	Cubic
Space group	F d -3 m
Lattice Parameter, Å	10.663(8)
Volume, $Å^3$	1212.68(3)
Z	8
Formula weight, g/mol	587.11
Calculated Density, g/cm^3	6.431

APPENDIX C

ADDITIONAL SCANNING ELECTRON MICROSCOPY RESULTS

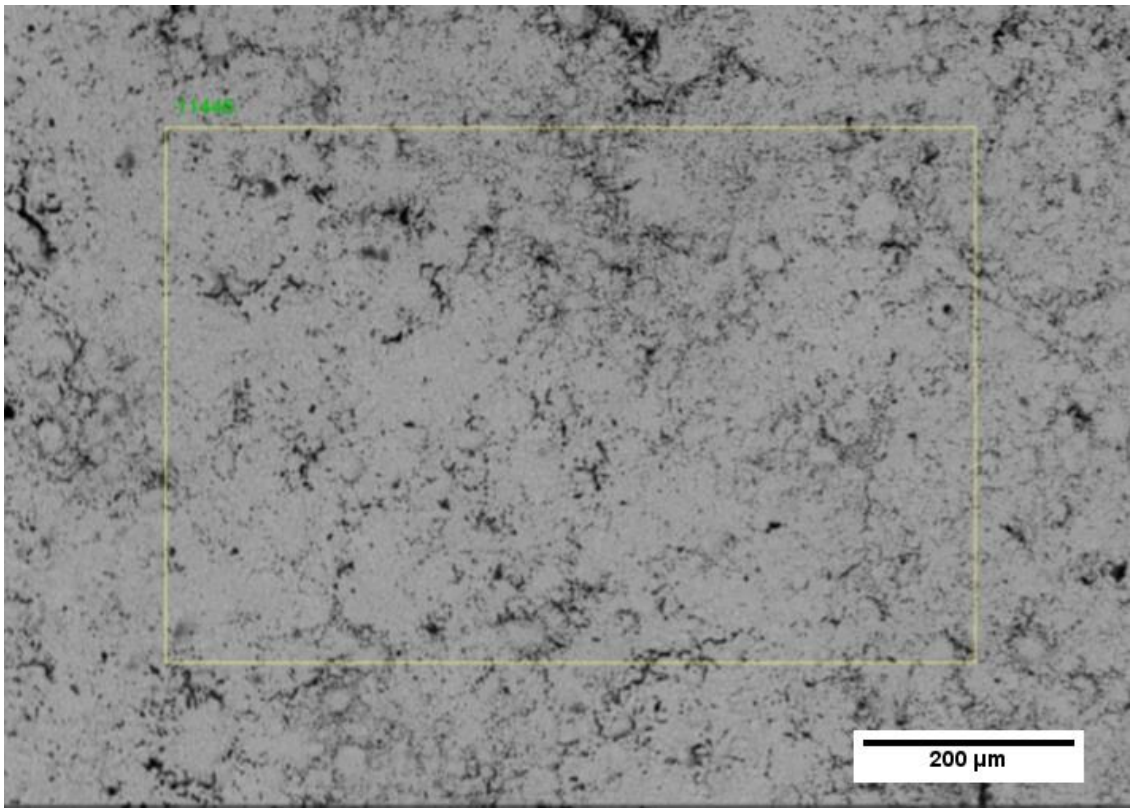

Figure C1: SEM image at 200 µm and area scan of polycrystalline $(Yb_{0.2}Tb_{0.2}Gd_{0.2}Dy_{0.2}Er_{0.2})_2Ti_2O_7$.

Table C1: Area scan concentration data for polycrystalline $(Yb_{0.2}Tb_{0.2}Gd_{0.2}Dy_{0.2}Er_{0.2})_2Ti_2O_7$.

Element	Atomic Number	Mass Concentration (%)	Mass Normalized (%)	Atom Concentration (%)	Absolute Error (%)
Oxygen	8	16.28	17.62	57.40	1.94
Titanium	22	19.63	21.24	23.13	0.57
Gadolinium	64	11.03	11.93	3.96	0.32
Terbium	65	11.56	12.51	4.10	0.33
Dysprosium	66	11.19	12.11	3.89	0.32
Erbium	68	11.05	11.95	3.73	0.32
Ytterbium	70	11.68	12.64	3.81	0.34
		92.41	100	100	

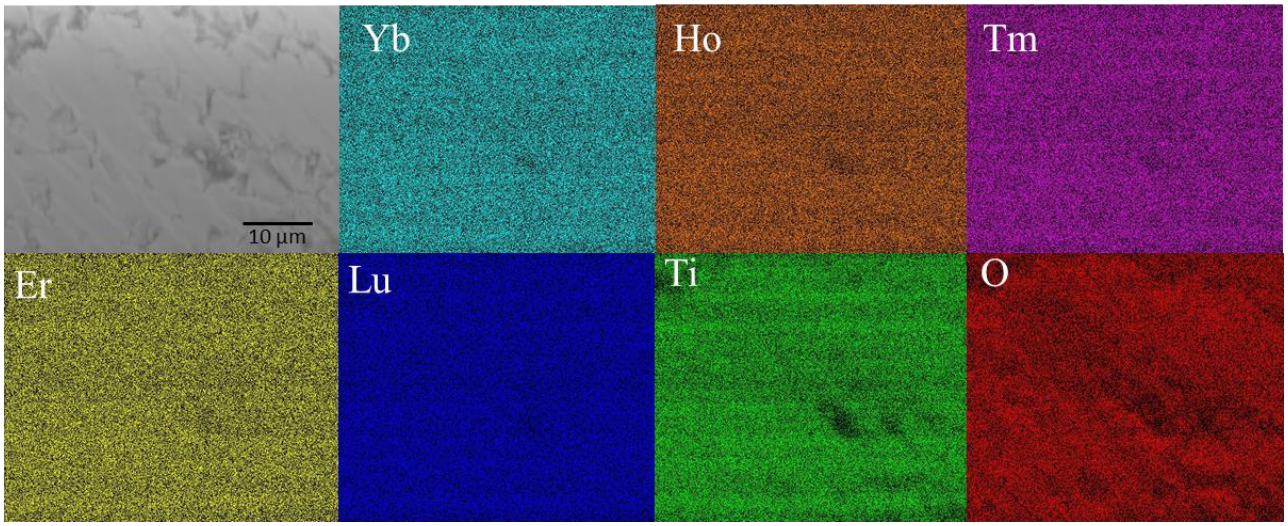

Figure C2: Color mapping of $(Yb_{0.2}Tm_{0.2}Lu_{0.2}Ho_{0.2}Er_{0.2})_2Ti_2O_7$ single crystal showing a homogenous distribution of the rare-earth cations on the micron scale.

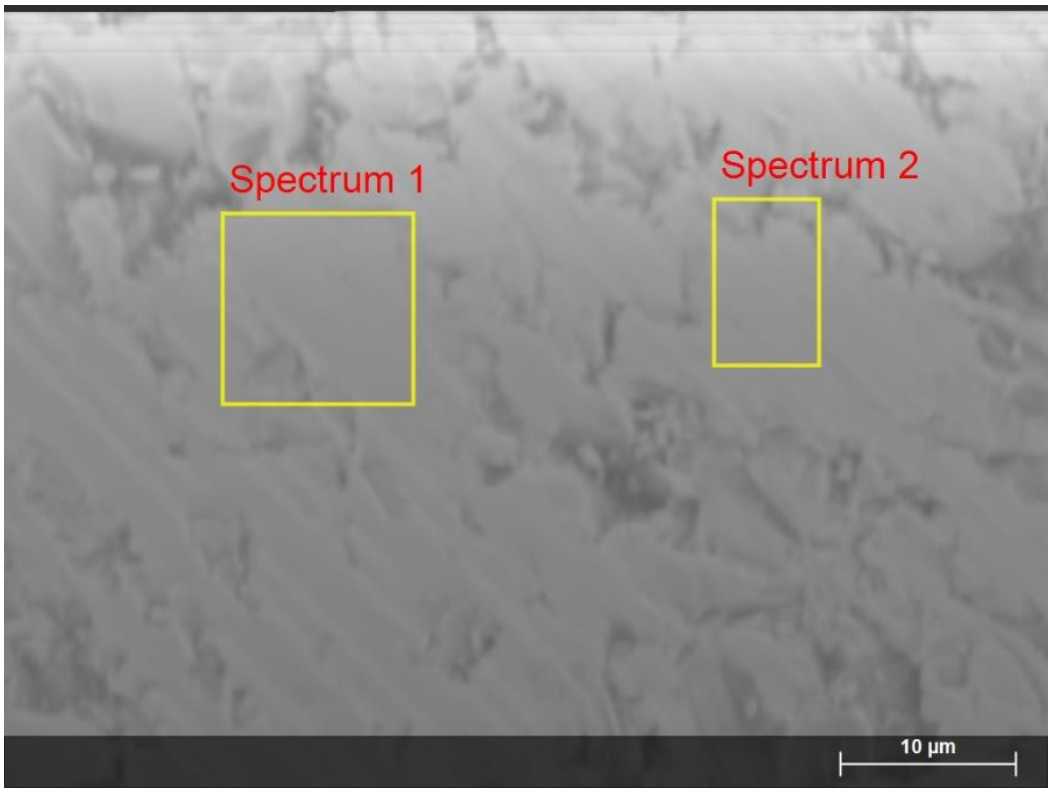

Figure C3: Image of the $(Yb_{0.2}Tm_{0.2}Lu_{0.2}Ho_{0.2}Er_{0.2})_2Ti_2O_7$ single crystalline surface using scanning electron microscopy at the micron scale.

Table C2: Area scan concentration data for spectrum 1 in Figure C5 of $(Yb_{0.2}Tm_{0.2}Lu_{0.2}Ho_{0.2}Er_{0.2})_2Ti_2O_7$ single crystal.

Element	Atomic Number	Mass Concentration (%)	Mass Normalized (%)	Atom Concentration (%)	Absolute Error (%)
Oxygen	8	14.69522722	15.70685734	55.33220756	1.765581293
Titanium	22	18.47387554	19.74563056	23.243914	0.536799153
Holmium	67	11.75101813	12.55996675	4.292204795	0.339968478
Erbium	68	11.95328867	12.77616175	4.305273078	0.346179195
Thulium	69	12.00234045	12.82859028	4.280098363	0.348565087
Ytterbium	70	12.39178797	13.24484766	4.314126301	0.360383247
Lutetium	71	12.2917712	13.13794566	4.232175904	0.359364675
		93.55930917	100	100	

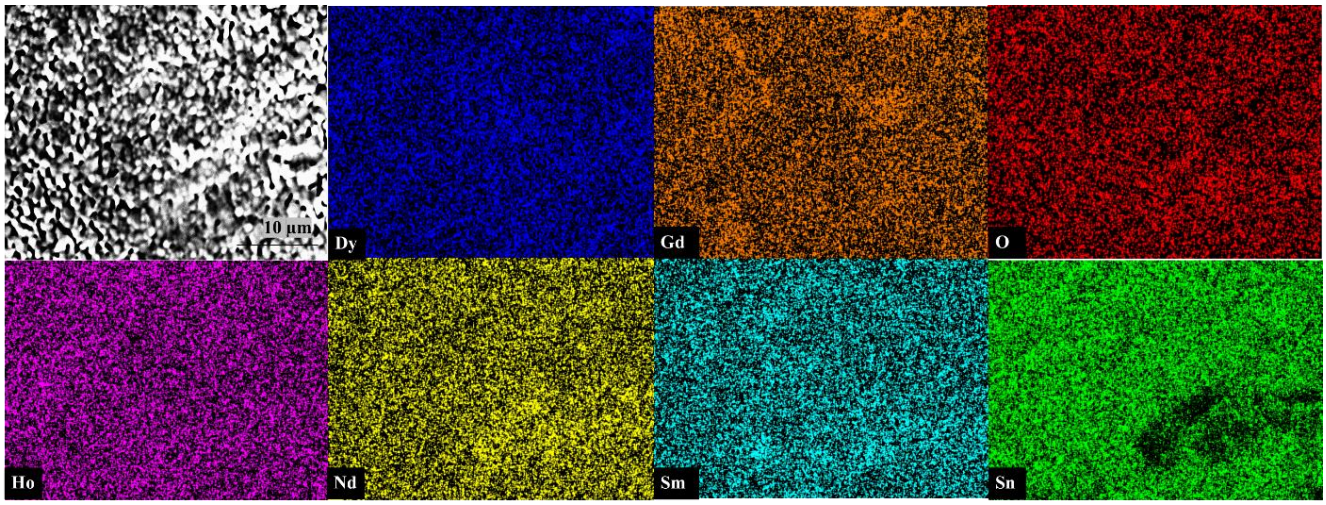

Figure C4: Color mapping of $(DyGdHoNdSm)_2Sn_2O_7$ polycrystal showing a homogenous distribution of the rare-earth cations on the micron scale.

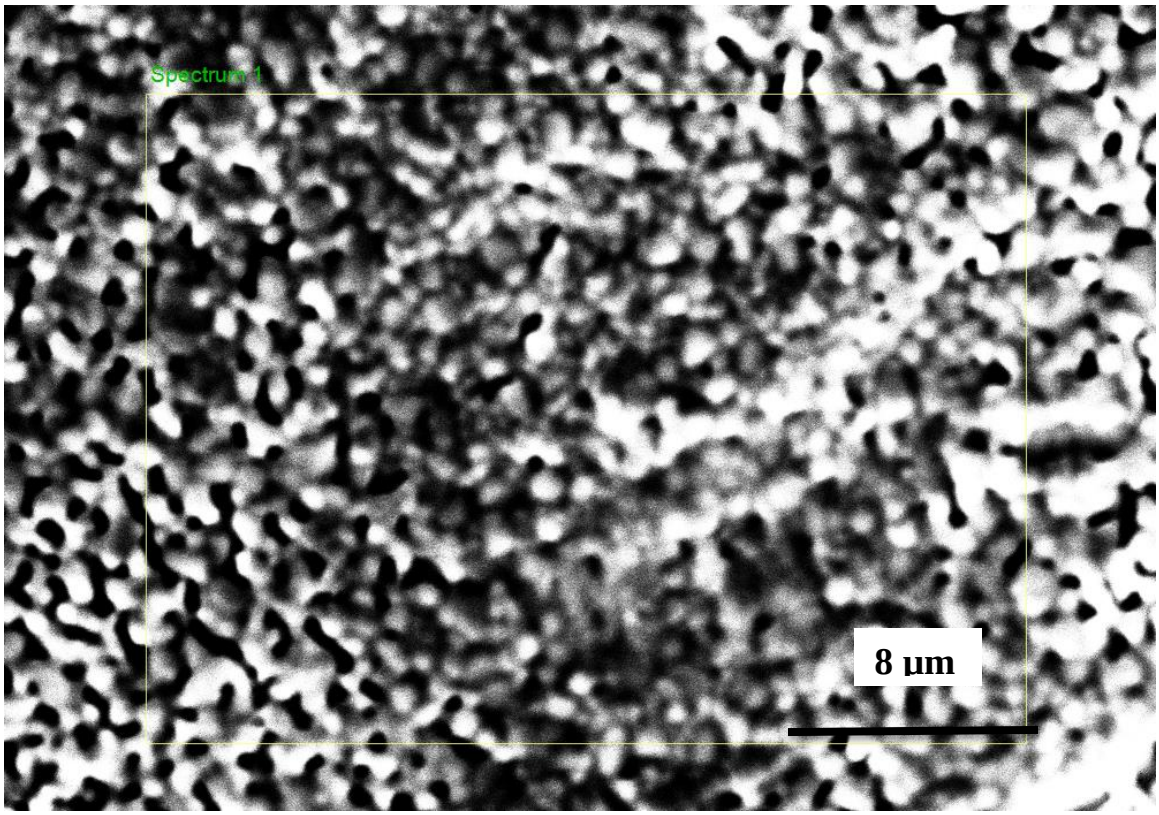

Figure C5: SEM area scan of polycrystalline $(Dy_{0.2}Ho_{0.2}Gd_{0.2}Sm_{0.2}Nd_{0.2})_2Sn_2O_7$.

Table C3: Area scan concentration data for polycrystalline $(Dy_{0.2}Ho_{0.2}Gd_{0.2}Sm_{0.2}Nd_{0.2})_2Sn_2O_7$.

Element	Atomic Number	Mass Concentration (%)	Mass Normalized (%)	Atom Concentration (%)	Absolute error (%)
Oxygen	8	7.655	7.996	42.816	0.403
Gadolinium	64	9.180	9.589	5.224	0.209
Neodymium	60	11.119	11.615	6.899	0.230
Samarium	62	8.797	9.189	5.236	0.196
Dysprosium	66	11.820	12.347	6.510	0.250
Holmium	67	10.608	11.081	5.756	0.244
Tin	50	36.557	38.185	27.559	0.735
		Sum	95.73595518	100	100

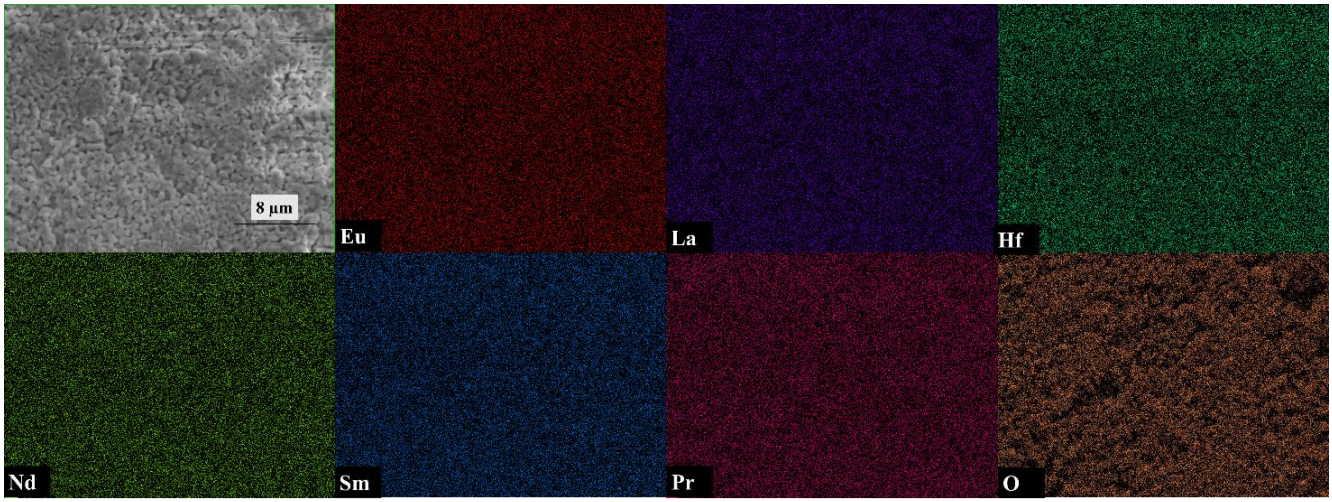

Figure C6: Color mapping of $(Eu_{0.2}Nd_{0.2}Sm_{0.2}Pr_{0.2}La_{0.2})_2Hf_2O_7$ showing a homogenous distribution of the rare-earth cations on the micron scale.

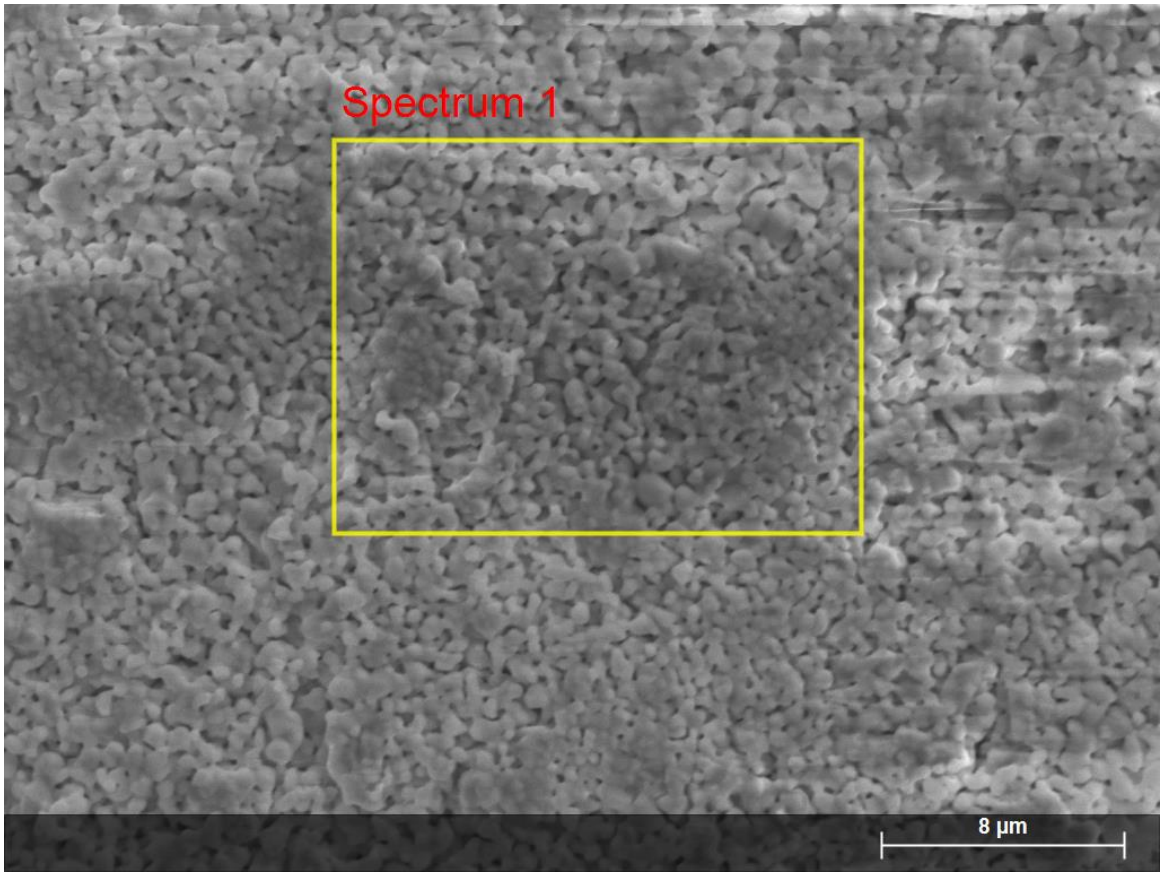

Figure C7: SEM area scan of polycrystalline $(Eu_{0.2}Nd_{0.2}Sm_{0.2}Pr_{0.2}La_{0.2})_2Hf_2O_7$.

Table C4: Area scan concentration data for polycrystalline $(Eu_{0.2}Nd_{0.2}Sm_{0.2}Pr_{0.2}La_{0.2})_2Hf_2O_7$.

Element	Atomic Number	Mass Concentration (%)	Mass Normalized (%)	Atom Concentration (%)	Absolute error (%)
O	8	13.709	20.715	72.278	1.963
La	57	5.156	7.791	3.131	0.182
Pr	59	5.126	7.746	3.069	0.180
Nd	60	5.634	8.514	3.295	0.194
Sm	62	5.546	8.380	3.111	0.193
Eu	63	5.597	8.458	3.107	0.195
Hf	72	25.410	38.396	12.009	0.756
		Sum	66.17816603	100	100

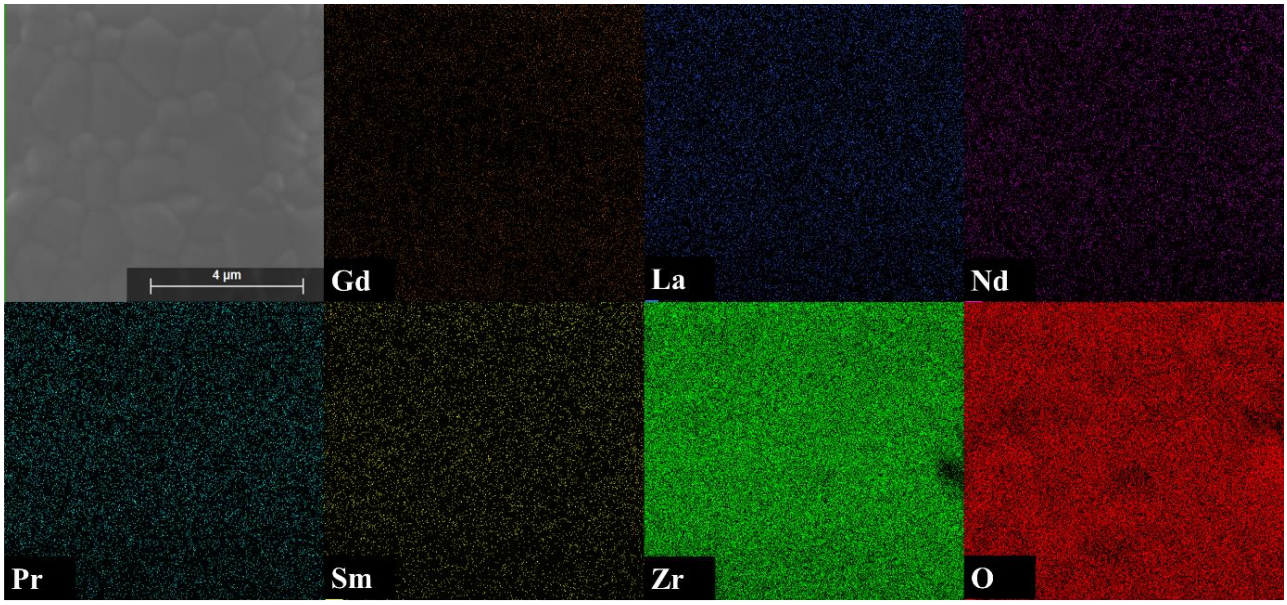

Figure C8: Color mapping of $(Nd_{0.2}Sm_{0.2}Gd_{0.2}Pr_{0.2}La_{0.2})_2Zr_2O_7$ showing a homogenous distribution of the rare-earth cations on the micron scale.

Figure C9: SEM area scan of polycrystalline $(Nd_{0.2}Sm_{0.2}Gd_{0.2}Pr_{0.2}La_{0.2})_2Zr_2O_7$.

Table C5: Area scan concentration data for polycrystalline $(Nd_{0.2}Sm_{0.2}Gd_{0.2}Pr_{0.2}La_{0.2})_2Zr_2O_7$.

Element	Mass Normalized (%)	Atom Concentration (%)	Absolute error (%)
O	47.250	85.937	6.890
Pr	4.152	0.857	0.209
Nd	5.448	1.099	0.252
Sm	4.476	0.866	0.229
Gd	3.760	0.696	0.217
La	5.408	1.133	0.245
Zr	29.505	9.412	1.323
	Sum	100	100

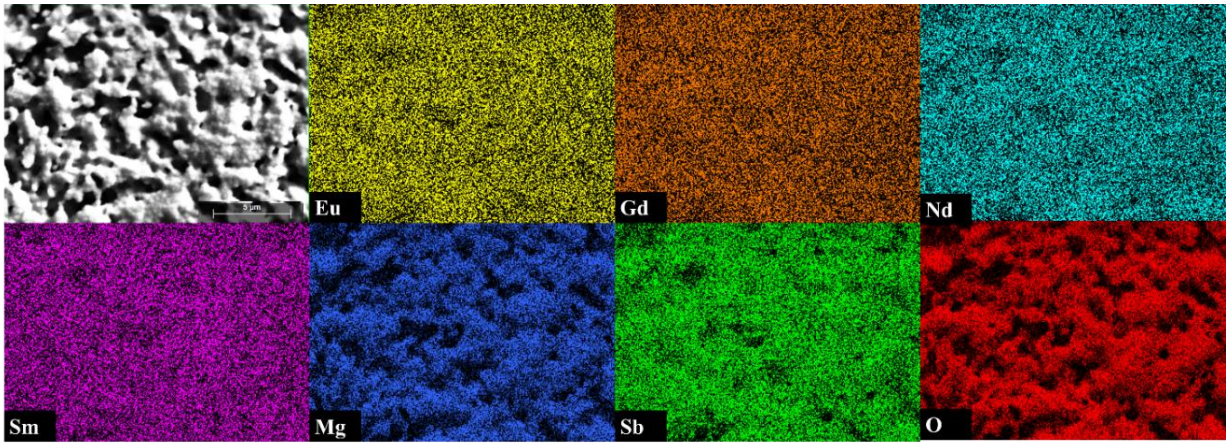

Figure C10: Color mapping of $(EuGdSmNd)_3Sb_3Mg_2O_{14}$ showing a homogenous distribution of the rare-earth cations on the micron scale.

APPENDIX D

AMBIENT TEMPERATURE RESONANT ULTRASOUND SPECTROSCOPY OF HIGH ENTROPY OXIDE FLUORITES

Two high entropy fluorite oxides (one equimolar and another non-equimolar) were successfully synthesized using solid state reactions with precursor reactants HfO_2, ZrO_2, CeO_2, Y_2O_3, Yb_2O_3, Gd_2O_3, and CaO at 1500˚C for 20 hours in air. These two polycrystals were then hot pressed at 1500˚C in an argon atmosphere with 0.9 tons of pressure to produce two dense pellets for resonant ultrasound spectroscopy (RUS) measurements at room temperature. The equimolar composition $(Hf_{0.2}Zr_{0.2}Ce_{0.2}Y_{0.2}Yb_{0.2})O_2$ was chosen for this study based on another report [D1], which used pulse-echo ultrasound to determine the elastic constants. It was desired to compare mechanical stiffness results from the Wright et al. study [D1] with our results determined by RUS. A novel second, non-equimolar composition $(Zr_{0.25}Hf_{0.25}Ce_{0.25})(Y_{0.0625}Gd_{0.0625}Yb_{0.0625}Ca_{0.0625})O_2$ was synthesized in a similar fashion as the equimolar for further comparison and for determining room temperature elastic moduli. Table D1 lists the resulting stiffness constants from this RUS study at room temperature, along with comparable data from Wright et al. These results indicate that the room temperature elastic moduli are similar to what has been reported on HEO fluorites.

Table D1: Room temperature resonant ultrasound spectroscopy elastic moduli fits for HEO fluorites.

Composition	C11 (GPa)	C44 (GPa)	rms error (%)	Bulk Modulus (GPa)	Young's Modulus (GPa)	Poisson's Ratio	Reference
$(Zr_{0.25}Hf_{0.25}Ce_{0.25})(Y_{0.0625}Gd_{0.0625}Yb_{0.0625}Ca_{0.0625})O_2$	294	83	0.42	182	217	0.302	This study
$(Hf_{0.2}Zr_{0.2}Ce_{0.2}Y_{0.2}Yb_{0.2})O_2$	269	77	0.43	166	202	0.297	This study
$(Hf_{0.2}Zr_{0.2}Ce_{0.2}Y_{0.2}Yb_{0.2})O_2$					232.6 ± 2.4		[D1]

Table D2: RUS output file with room temperature elastic moduli fit for HEO fluorite.

mass=	0.2661 grams		rho= 7.161 gm/cc

Mode	**Fexp (MHz)**	**Fcalc (MHz)**	**% error**
1	0.1337494	0.1278622	-4.4
2	0.1532125	0.1520011	-0.79
3	0.2737485	0.272006	-0.64
4	0.28966	0.2908859	0.42
5	0.32008	0.3176429	-0.76
6	0.32998	0.3323992	0.73
7	0.3822216	0.38167	-0.14
8	0.39884	0.3971612	-0.42
9	0.4117364	0.4113249	-0.1
10	0.4521677	0.4536851	0.34
11	0.4883247	0.4902716	0.4
12	0.531045	0.5300553	-0.19
13	0.5371089	0.5326052	-0.84
14	0.6091774	0.6097848	0.1
15	0.6106737	0.613611	0.48
16	0.6122799	0.6157792	0.57
17	0.6262	0.6255848	-0.1
18	0.636099	0.6365859	0.08
19	0.6525263	0.6504953	-0.31
20	0.65809	0.6596798	0.24
21	0.6649803	0.6675943	0.39
22	0.6746144	0.6777863	0.47
23	0.7751788	0.7765216	0.17
24	0.8176991	0.8180466	0.04
25	0.8476919	0.8494174	0.2

Bulk	Modulus (GPa)=	182.3625	
Young's	Modulus (GPa)=	217.0191	
Shear	Modulus (GPa)=	83.3625	
c11(GPa)	293.51248	V(compressional)(km/s) =	6.40201
c44(GPa)	83.36246	V(shear)(km/s) =	3.41184
d1(cm)	d2(cm)	d3(cm)	
0.1263	0.455	0.6466	

rms error=
0.4276%

REFERENCES

[D1] A.J. Wright et al. “From High-Entropy Ceramics to Compositionally-Complex Ceramics: A Case Study of Fluorite Oxides,” Journal of the European Ceramic Society, 40, 2120-2129 (2020).

APPENDIX E

DC SUSCEPTIBILITY CURVES

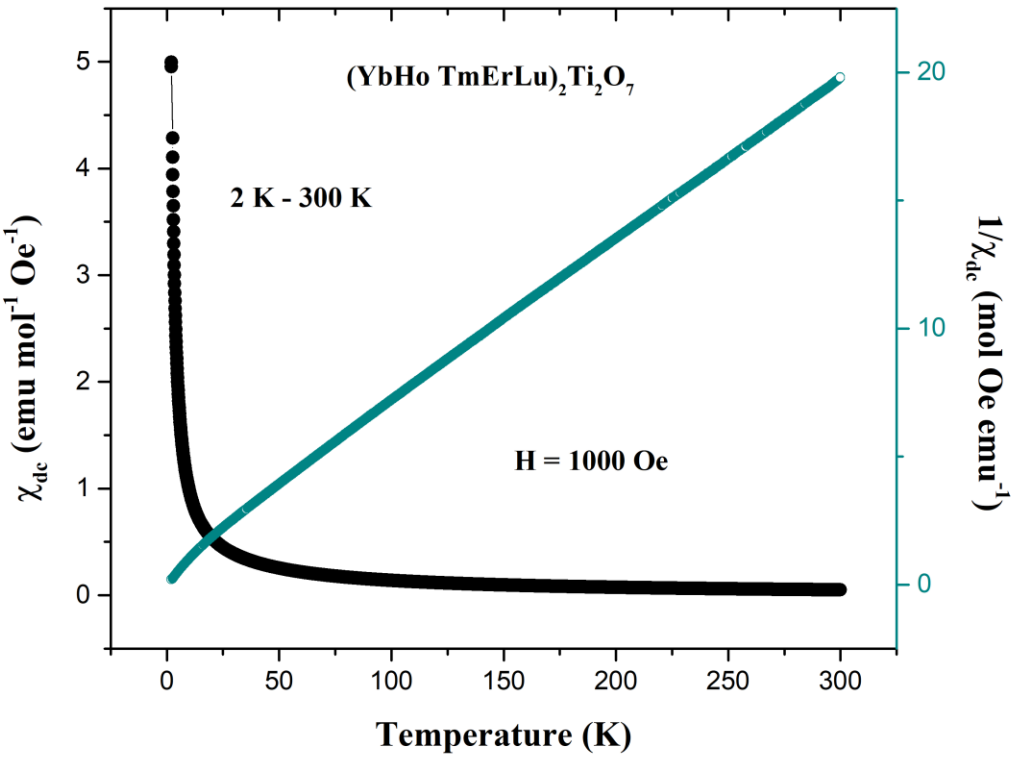

Figure E1: DC susceptibility for $(YbTmLuHoEr)_2Ti_2O_7$ single crystal.

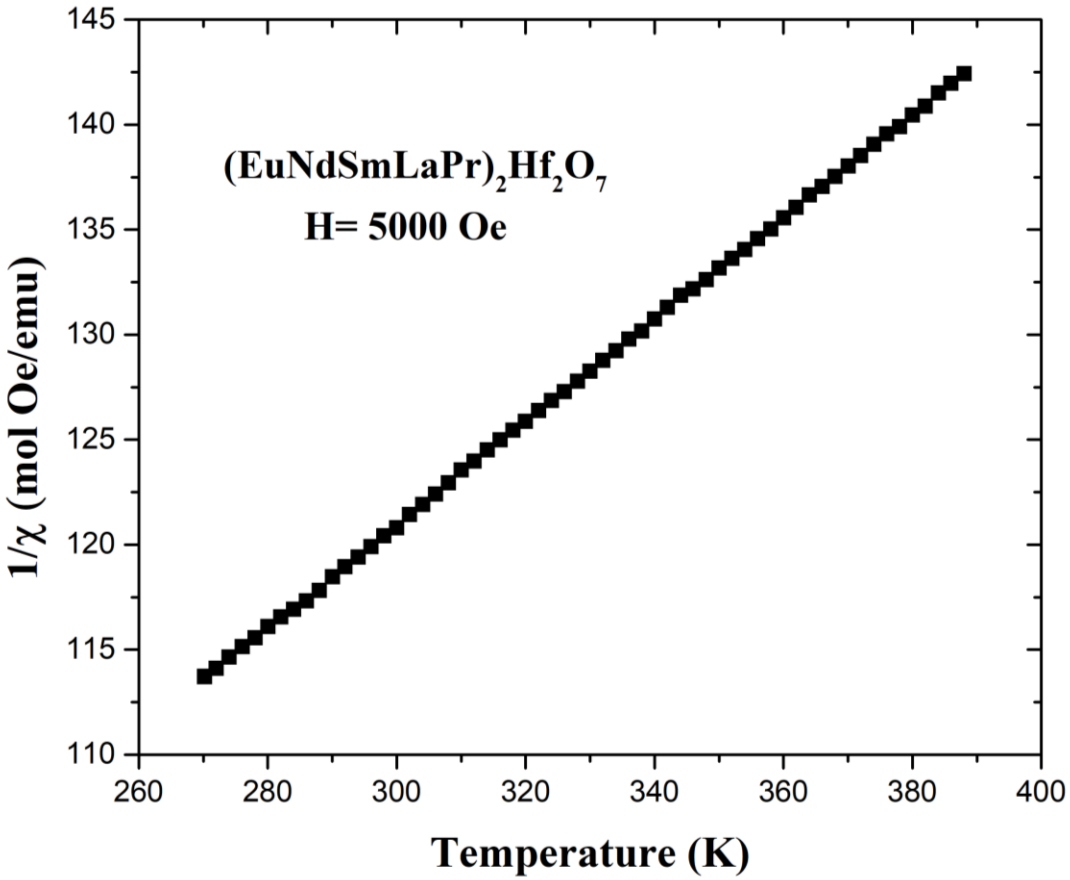

Figure E2: DC inverse susceptibility for polycrystalline $(EuNdSmLaPr)_2Hf_2O_7$ from 270 to 390 K.

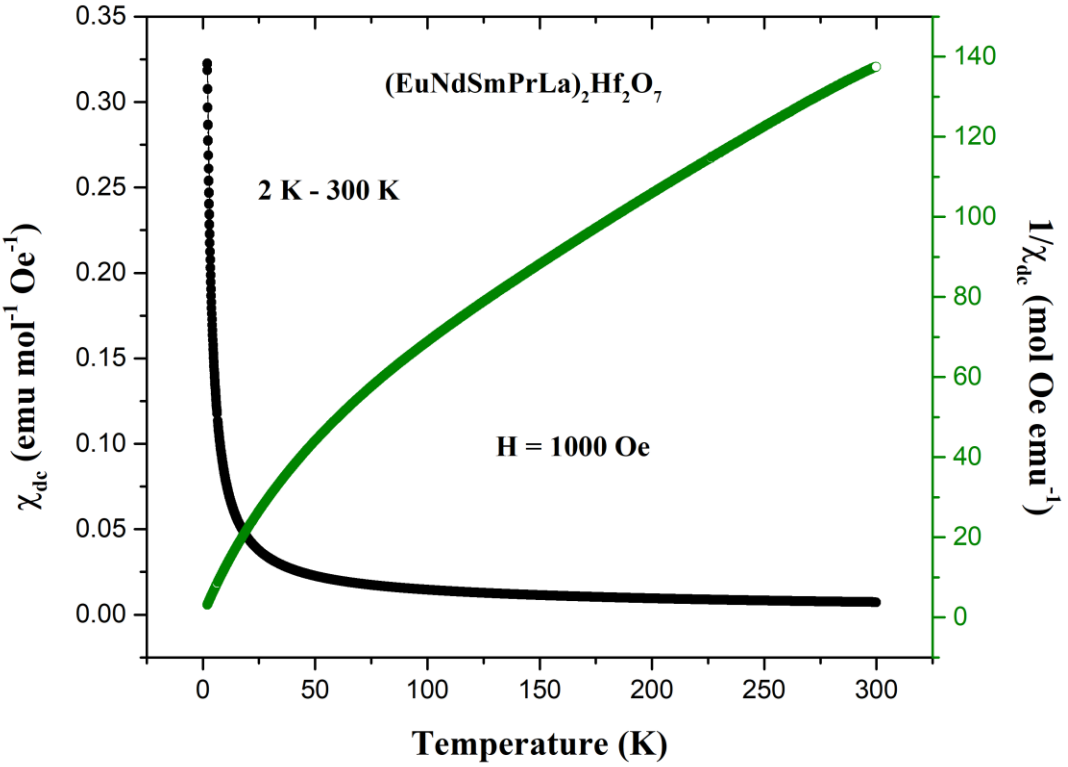

Figure E3: DC susceptibility for polycrystalline $(EuNdSmPrLa)_2Hf_2O_7$.

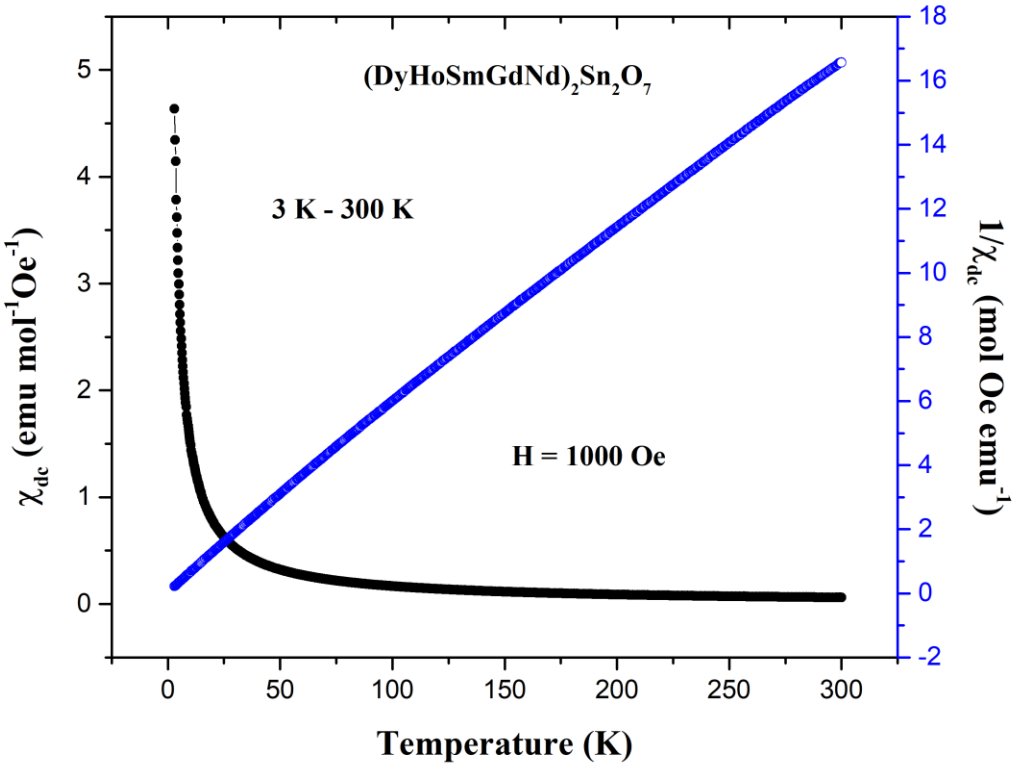

Figure E4: DC susceptibility for polycrystalline $(DyHoSmGdNd)_2Sn_2O_7$.

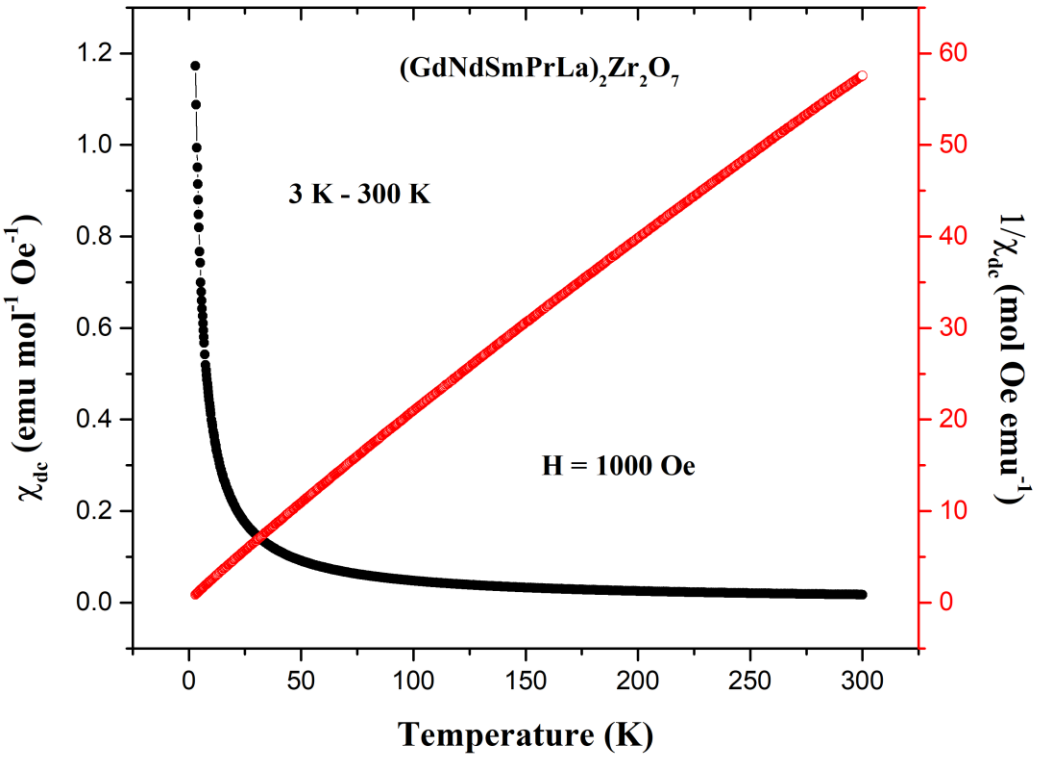

Figure E5: DC susceptibility for polycrystalline $(GdNdSmPrLa)_2Zr_2O_7$.

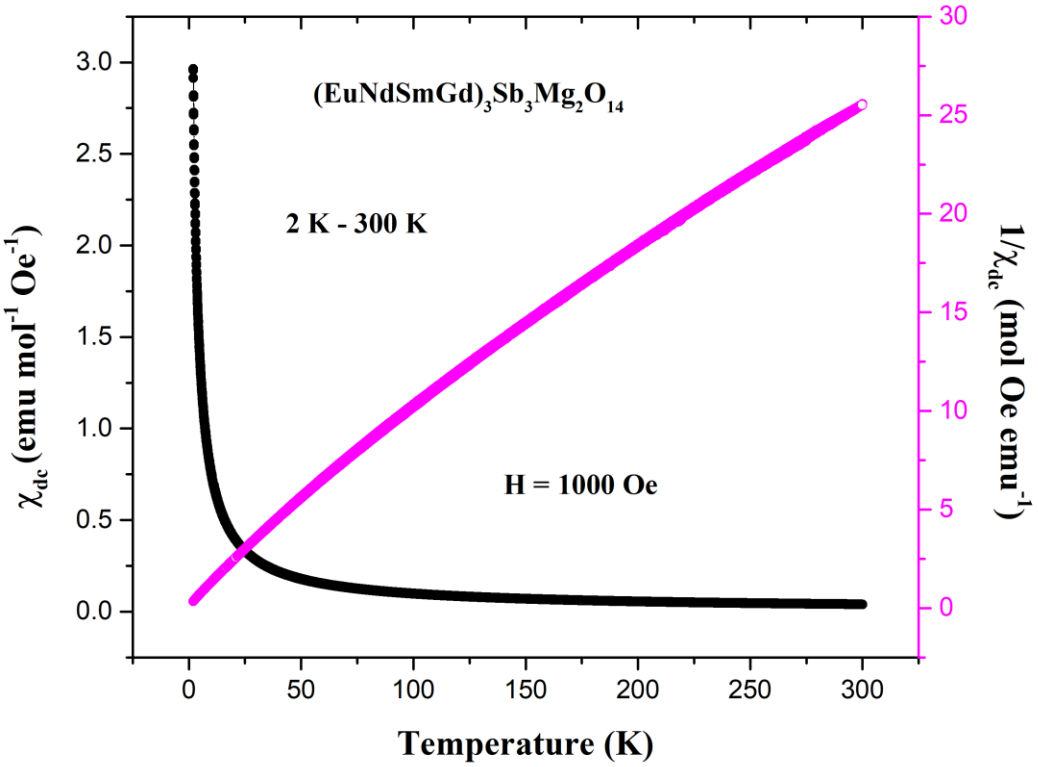

Figure E6: DC susceptibility for polycrystalline $(EuNdSmGd)_3Sb_3Mg_2O_{14}$.

Table E1: List of experimentally derived effective magnetic moments and Curie-Weiss temperatures from magnetic susceptibility measurements on each pyrochlore-type HEO.

HEO Sample	Sample Type	Field Direction	Temperature Range (K)	Effective Magnetic Moment (μB)	Curie-Weiss Temperature (K)
$(YbTbGdErDy)_2Ti_2O_7$	Single Crystal	along [100]	3 - 20	5.79	-2.98(0)
$(YbHoTmErLu)_2Ti_2O_7$	Single Crystal	along [100]	2 - 20	4.67	-0.64(7)
$(DyHoSmGdNd)_2Sn_2O_7$	Polycrystal		3 - 20	5.66	-0.43(8)
$(EuPrSmLaNd)_2Hf_2O_7$	Polycrystal		2 - 20	1.37	-1.36(4)
$(GdNdSmPrLa)_2Zr_2O_7$	Polycrystal		3 - 20	3.02	-1.09(4)
$(NdSmEuGd)_3Sb_3Mg_2O_{14}$	Polycrystal		2 - 20	2.78	-1.19(7)

VITA

Candice Kinsler-Fedon (*née* Kinsler) was born in Morristown, TN and grew up in White Pine, TN. She attended Jefferson County High School and graduated in May of 2011. Later that year, she began studying physics at the University of Tennessee, Knoxville. As an undergraduate, Candice participated in research in between classes where she learned to synthesize various oxide compounds and studied their magnetic properties. Candice obtained her B.S. in General Physics with a minor in Materials Science and Engineering in December 2015. After graduation, she continued her education by enrolling in the graduate program for Materials Science and Engineering at the University of Tennessee, Knoxville. She received her M.S. in May 2019 and Ph.D. degree in May 2022 for Materials Science and Engineering. During her time as a graduate research assistant, she focused on the synthesis and characterization involving the magnetic, mechanical, thermal, and radiation resistant properties of high-entropy oxides (HEOs) with pyrochlore-type structures.